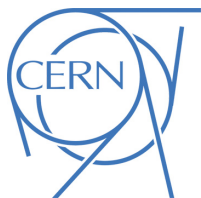




ATLAS Note



Draft version 16

1

2

3

4

Search for flavor-changing neutral currents tHq interactions with $H \rightarrow \tau^+\tau^-$ in proton-proton collisions at $\sqrt{s} = 13$ TeV

5

The ATLAS Collaboration

6

17th January 2021

7

A search is presented for flavor-changing neutral currents tHq interactions with $H \rightarrow \tau^+\tau^-$ using a data set collected with the ATLAS detector at the LHC, corresponding to an integrated luminosity of 140 fb^{-1} of proton-proton collisions at a center-of-mass energy of 13 TeV. The search is performed in the decay chain $t\bar{t} \rightarrow Wb + Hq$ or $qg \rightarrow tH \rightarrow Wb + H$ ($q = c/u$), where the W boson decays inclusively and H decays to $\tau^+\tau^-$. Upper limits at 95 % confidence level for the coupling coefficient are measured to be XXX and XXX , while the expected limits are $XXX^{+XXX}_{-XXX}\%$ and $XXX^{+XXX}_{-XXX}\%$, respectively.

14

© 2021 CERN for the benefit of the ATLAS Collaboration.

Reproduction of this article or parts of it is allowed as specified in the CC-BY-4.0 license.

15 **Contents**

16	1 To do list	4
17	2 Change log	4
18	3 Introduction	5
19	4 Analysis outline	6
20	4.1 Signal regions	6
21	4.2 Analysis strategy for leptonic channels	7
22	4.3 Analysis strategy for in Hadronic channels	8
23	4.4 Blinding strategy	8
24	5 Detector, data set and Monte Carlo simulation	8
25	5.1 ATLAS detector	8
26	5.2 Data set	10
27	5.3 Signal and background simulation	11
28	6 Object reconstruction	13
29	6.1 Jets	13
30	6.2 b-tagging	14
31	6.3 Light leptons	14
32	6.4 Hadronic tau decays	14
33	6.5 Missing transverse energy	15
34	6.6 Tight lepton isolation: <code>PromptLeptonVeto(PLV)</code>	15
35	6.7 Overlap removal	16
36	7 Signal regions	18
37	7.1 Trigger	18
38	7.2 Cuts	19
39	8 Reconstruction of event topology	21
40	9 Background estimation	43
41	9.1 Fake tau estimation in leptonic channels	43
42	9.2 QCD fake background in $\tau_{\text{lep}}\tau_{\text{had}}$ and $l\tau_{\text{had}}$ regions	45
43	9.3 Fake tau estimate in hadronic channels	47
44	10 MVA analysis	58
45	11 Systematic uncertainties	67

46	11.1 Luminosity (TBD)	67
47	11.2 Detector-related uncertainties (TBD)	67
48	11.3 Uncertainties on fake background estimations	68
49	11.4 Theoretical uncertainties on the background (TBD)	69
50	11.5 Uncertainties on the signal modelling (TBD)	70
51	12 Fit model and signal extraction	71
52	13 Results	76
53	Appendix	79
54	A Sample DSID list	79
55	B Derivation and framework level cuts	80

⁵⁶ **1 To do list**

⁵⁷ Implementation of theory systematics and instrumental systematics.

⁵⁸ PLIV implementation

⁵⁹ **2 Change log**

⁶⁰ From V1 to V2:

⁶¹ Leptonic channels: 80fb-1 → 140fb-1

⁶² BDT tau ID → RNN tau ID

⁶³ Updates to PFlow jets with DL1r b-tagging.

⁶⁴ Optimised event selection.

⁶⁵ Changed fake estimation method.

⁶⁶ Added signal regions $l\tau$ 1j and $l\tau$ 2j.

⁶⁷ From V2 to V3:

⁶⁸ Added to do list and change log.

⁶⁹ Added Analysis outline section and moved signal region definition here.

70 3 Introduction

71 Since the discovery of the Higgs boson in 2012, great efforts are made to study its properties. As the
 72 mass of the Higgs boson is about 125 GeV [1], it is kinematically allowed that a top quark decays to
 73 a Higgs boson and an up-type quark via the flavour-changing neutral current (FCNC). In the Standard
 74 Model (SM), the FCNC interaction is forbidden at tree level and suppressed at higher orders due to the
 75 Glashow-Iliopoulos-Maiani (GIM) mechanism [2]. The $t \rightarrow u/c + H$ branching fraction in the SM is
 76 calculated to be around 10^{-15} [3]. It would be enhanced in many models beyond the SM (BSM). Examples
 77 are the quark-singlet model [4, 5], the two-Higgs doublet model with or without the flavour violation [6,
 78 7], the minimal supersymmetric standard model (MSSM) [8], supersymmetry with R-parity violation [9],
 79 the Topcolour-assisted Technicolour model [10] or models with warped extra dimensions [11], the little
 80 Higgs model with T-parity conservation [12] and the composite Higgs models [13]. Especially, the ansatz
 81 of Cheng and Sher [14] allows a branching fraction of about 10^{-3} [15]. Therefore, an observation of this
 82 decay would be a clear evidence for new physics.

83 On the other hand, if the tHq interaction exists, the single-top, Higgs associated production through this
 84 interaction should also be enhanced. The tH associated production in the SM prediction is expected to be
 85 small at LHC[16]. So the study on this process will also contribute to the FCNC interaction searches.

86 Upper 95% CL limits on $\text{BR}(t \rightarrow Hq)$ have been obtained by ATLAS based on the data from 2015 and
 87 2016, in the $H \rightarrow \gamma\gamma$ [17], $H \rightarrow WW/\tau_{\text{lep}}\tau_{\text{lep}}$ multilepton [18] and $H \rightarrow \tau\tau, H \rightarrow b\bar{b}$ [19] channels. The
 88 combined expected (observed) limits are 0.083% (0.11%) and 0.083% (0.12%) for $t \rightarrow Hc$ and $t \rightarrow Hu$
 89 decay branching ratio, respectively.

90 The $t \rightarrow Hq$ decay and $gq \rightarrow tH$ production are also searched by CMS based on the data from 2015
 91 and 2016[20] using the $H \rightarrow b\bar{b}$ decay. The branching ratio derived for $t \rightarrow Hc$ and $t \rightarrow Hu$ decay are
 92 0.47% (0.44%) and 0.47% (0.34%) respectively.

93 The FCNC coupling is parametrised using dim-6 operators [21]. The effective Lagrangian regarding tqH
 94 interaction is:

$$\mathcal{L}_{EFT} = \frac{C_{u\phi}^{i3}}{\Lambda^2} (\phi^\dagger \phi) (\bar{q}_i t) \tilde{\phi} + \frac{C_{u\phi}^{3i}}{\Lambda^2} (\phi^\dagger \phi) (\bar{t}_i q) \tilde{\phi} \quad (1)$$

95 Where the operator notation is consistent with [21]. The coefficient $C_{u\phi}$'s can be extracted as

$$\begin{aligned} (C_{u\phi}^{i3})^2 + (C_{u\phi}^{3i})^2 &= 1946.6 \text{ BR}(t \rightarrow qH) \\ (C_{u\phi}^{13})^2 + (C_{u\phi}^{31})^2 &= \sigma(ug \rightarrow tH)/365.2 \text{ fb} \\ (C_{u\phi}^{23})^2 + (C_{u\phi}^{32})^2 &= \sigma(cg \rightarrow tH)/52.9 \text{ fb} \end{aligned} \quad (2)$$

96 To give a better impression on the numbers, we use $\text{BR}(t \rightarrow qH) = 1(0.2)\%$ as benchmark, which is
 97 corresponding to $(C_{u\phi}^{13})^2 + (C_{u\phi}^{31})^2 = 19.47(3.89)$, $\sigma(ug \rightarrow tH) = 7109.0(1421.8)$ pb, $\sigma(cg \rightarrow tH) =$
 98 1029.8(206.0) pb.

99 In this article, a search for the decay $t \rightarrow qH$ in the $t\bar{t}$ production (TT) and single-top, Higgs associated
100 production (ST) with $H \rightarrow \tau\tau$ as shown in Fig 1 using 140 fb^{-1} of proton-proton collision data at 13 TeV,
101 taken with the ATLAS detector at the Large Hadron Collider (LHC), is presented. The final state is
102 characterized by one top and one Higgs. In TT, there is an additional u/c quark forming a top resonance
103 with Higgs.

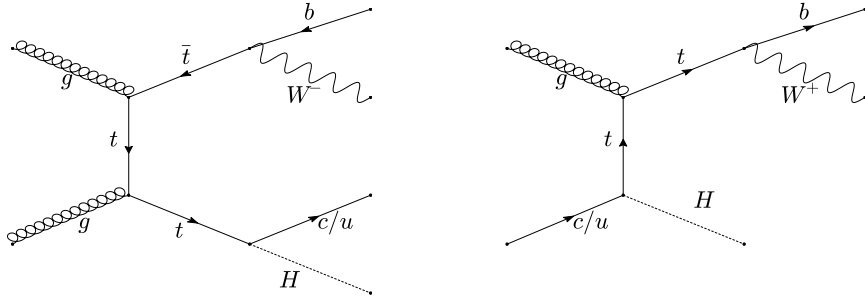


Figure 1: Diagrams of FCNC TT(left) and ST(right) process.

104 4 Analysis outline

105 4.1 Signal regions

106 As demonstrated in the Figure 1, depending on the production modes and the decay of the W boson from
107 top quark, the analysis is split into 4 kinds of final states as shown in table 1. Except events with 2 leptons
108 (leptonic tau included) or no hadronic tau in the final states, all of the decay modes are considered in the
109 analysis.

110 Due to the low statistics in STL and TTL regions, the STL and TTL are included in a single region
111 $l\tau_{\text{had}}\tau_{\text{had}}$ for $H \rightarrow \tau_{\text{had}}\tau_{\text{had}}$ where there is no light jet multiplicity requirement. However due to the low
112 tau reconstruction rate, it is not rare that one of tau fails the reconstruction and remains as a jet. So the
113 $l\tau_{\text{had}} 1j$ and $l\tau_{\text{had}} 2j$ are included as signal regions where the lepton and τ_{had} are required to have the same
114 charged to reduce background.

115 The summary for the signal regions are listed in Table 2. With corresponding yield after fake estimation
116 in Table 4.

117 For the future convenience, STH $\tau_{\text{lep}}\tau_{\text{had}}$ and TTH $\tau_{\text{lep}}\tau_{\text{had}}$ are indicated by $\tau_{\text{lep}}\tau_{\text{had}}$; STH $\tau_{\text{had}}\tau_{\text{had}}$ and TTH
118 $\tau_{\text{had}}\tau_{\text{had}}$ are indicated by $\tau_{\text{had}}\tau_{\text{had}}$; $l\tau_{\text{had}} 2j$ and $l\tau_{\text{had}} 1j$ are indicated by $l\tau_{\text{had}}$. All the of regions involving
119 leptons (including τ_{lep}) are indicated by "leptonic channels", otherwise "hadronic channels".

Table 1: Overview of the final states of signal events.

	# of particles	alias	b-jet	jets	lepton	taus
ST	$W \rightarrow l\nu$	STL	1	1	1	2
	$W \rightarrow q\bar{q}$	STH	1	3	0	2
TT	$W \rightarrow l\nu$	TTL	1	2	1	2
	$W \rightarrow q\bar{q}$	TTH	1	4	0	2

Table 2: Overview of the signal regions.

Signal regions	b-jet	light flavor jets	lepton	hadronic taus	charge
$l\tau_{\text{had}} 2j$	1	2	1	1	$l\tau_{\text{had}}$ SS
$l\tau_{\text{had}} 1j$	1	1	1	1	$l\tau_{\text{had}}$ SS
$l\tau_{\text{had}}\tau_{\text{had}}$	1	any	1	2	$\tau_{\text{had}}\tau_{\text{had}}$ OS
STH $\tau_{\text{had}}\tau_{\text{had}}$	1	2	0	2	$\tau_{\text{had}}\tau_{\text{had}}$ OS
TTH $\tau_{\text{had}}\tau_{\text{had}}$	1	≥ 3	0	2	$\tau_{\text{had}}\tau_{\text{had}}$ OS
STH $\tau_{\text{lep}}\tau_{\text{had}}$	1	2	1	1	$\tau_{\text{lep}}\tau_{\text{had}}$ OS
TTH $\tau_{\text{lep}}\tau_{\text{had}}$	1	≥ 3	1	1	$\tau_{\text{lep}}\tau_{\text{had}}$ OS

120 4.2 Analysis strategy for leptonic channels

- 121 The main background contributing to the leptonic channels, defined in the last section, is top pair production
122 as shown in Figure 21. It can either contribute as reducible and irreducible background.
- 123 As irreducible background, when the top pair decays full-leptonically to a l and a τ , and one of the b -jet
124 from top decay fails the b -tagging, the event ends up in STH $\tau_{\text{lep}}\tau_{\text{had}}$ region. If there are radiation or
125 pile-up jets, the event ends up TTH $\tau_{\text{lep}}\tau_{\text{had}}$ region.
- 126 The irreducible background is modelled directly by Monte Carlo.
- 127 As reducible background, when the top pair decays full-leptonically, to a l and a τ_{had} , and one of the b -jet
128 from top decay fails the b -tagging, if the b -jet or one of the radiation jet is reconstructed as a τ_{had} the event
129 ends up in the $l\tau_{\text{had}}\tau_{\text{had}}$ region. When the top pair decays semi-leptonically, but one of the W-decaying jet
130 or the radiation jet or pile-up jet fakes a τ_{had} . Depending on the jet multiplicity, the event ends up in STH
131 $\tau_{\text{lep}}\tau_{\text{had}}$ or TTH $\tau_{\text{lep}}\tau_{\text{had}}$ if the fake tau has the opposite charge to the lepton or in $l\tau 1j/2j$ if the fake tau
132 has the same charge as the lepton.
- 133 The reducible background except QCD is also modelled by Monte Carlo but with scale factors derived
134 from the $t\bar{t}$ control regions in Table 3 and explained in 9.1.
- 135 The QCD multi-jets also contribute a small fraction of the reducible background by faking both lepton
136 and taus, especially in the low jet multiplicity region $l\tau 1j$. This is modelled by the ABCD method by
137 cutting on $E_{\text{T}}^{\text{miss}}$ and the PLV defined in Sec. 6.6 as explained in 9.2.

Table 3: Overview of the control regions used for fake tau scale factor derivation in leptonic channels.

Control regions	b-jet	light flavor jets	lepton	hadronic taus	charge
$2l1tau1bnj$	1	any	2	1	ll OS
$2l1tau2bnj$	2	any	2	1	ll OS
$1l1tau2b2jSS$	2	2	1	1	$l\tau$ SS
$1l1tau2b2jOS$	2	2	1	1	$l\tau$ OS
$1l1tau2b3jSS$	2	≥ 3	1	1	$l\tau$ SS
$1l1tau2b3jOS$	2	≥ 3	1	1	$l\tau$ OS

138 4.3 Analysis strategy for in Hadronic channels

- 139 Similar to STH $\tau_{\text{lep}}\tau_{\text{had}}$ or TTH $\tau_{\text{lep}}\tau_{\text{had}}$, the $t\bar{t}$ also contributes to the hadronic channels as reducible and
 140 irreducible background. But in the hadronic channels, much larger contribution is observed from $Z \rightarrow \tau\tau$
 141 with radiated b -jet and QCD faking both taus as shown in Figure 27.
 142 The irreducible background is modelled directly by Monte Carlo. The reducible background with sub-
 143 leading taus faked is modelled by Fake Factor method while the reducible background with leading taus
 144 faked is modelled by Monte Carlo with a conservative uncertainty of 50% according to Sec. 9.1.

145 4.4 Blinding strategy

- 146 In order to keep the analysis unbiased from artificial cut tunings some data histogram bins are blinded.
 147 The blinding threshold is quantified as significances reaching 1 when decaying branching ratio is 0.2%
 148 to be conservative enough when the published limit is around 0.1%. The data is shown in some signal
 149 regions where the sensitivities are too low that none of the bins are above the threshold. In addition, the
 150 signal enriched high BDT region are blinded ($\text{BDT} > 0.2$).

151 5 Detector, data set and Monte Carlo simulation

152 5.1 ATLAS detector

- 153 The ATLAS detector [22] at the LHC covers nearly the entire solid angle around the collision point. It
 154 consists of an inner tracking detector surrounded by a thin superconducting solenoid, electromagnetic
 155 and hadronic calorimeters, and a muon spectrometer incorporating three large superconducting toroid
 156 magnets.

Table 4: The summary for the yield in the signal regions and control regions.

	$l\tau_{had}$ 1j	STH $\tau_{lep}\tau_{had}$	$l\tau_{had}$ 2j	TTH $\tau_{lep}\tau_{had}$
data	6384.00 ± 79.90	46505.00 ± 215.65	5312.00 ± 72.88	32551.00 ± 180.42
background	5432.51 ± 101.62	55575.24 ± 114.29	5393.40 ± 49.31	39974.01 ± 77.00
$\bar{t}t \rightarrow bWcH$	53.85 ± 0.57	96.11 ± 0.91	49.61 ± 0.55	124.16 ± 1.11
$cg \rightarrow tH$	2.10 ± 0.04	5.26 ± 0.07	1.30 ± 0.03	4.16 ± 0.07
tCH merged signal	55.95 ± 0.57	101.36 ± 0.92	50.91 ± 0.55	128.33 ± 1.12
$\bar{t}t \rightarrow bWuH$	55.82 ± 0.59	98.60 ± 0.90	51.92 ± 0.56	130.12 ± 1.11
$ug \rightarrow tH$	10.64 ± 0.20	26.92 ± 0.38	7.02 ± 0.16	23.35 ± 0.38
tuH merged signal	66.45 ± 0.62	125.53 ± 0.98	58.94 ± 0.58	153.47 ± 1.17
	$111\tau_{had}2b2j$ os	$111\tau_{had}2b2j$ ss	$111\tau_{had}2b3j$ os	$111\tau_{had}2b3j$ ss
data	18462.00 ± 135.87	1916.00 ± 43.77	11064.00 ± 105.19	1873.00 ± 43.28
background	22569.70 ± 54.82	2081.29 ± 16.53	13627.86 ± 42.33	1911.80 ± 15.61
$\bar{t}t \rightarrow bWcH$	10.79 ± 0.32	4.38 ± 0.16	10.69 ± 0.33	3.34 ± 0.14
$cg \rightarrow tH$	0.29 ± 0.02	0.05 ± 0.01	0.18 ± 0.02	0.04 ± 0.01
tCH merged signal	11.08 ± 0.32	4.43 ± 0.16	10.86 ± 0.33	3.37 ± 0.14
$\bar{t}t \rightarrow bWuH$	5.15 ± 0.21	2.04 ± 0.11	5.82 ± 0.23	1.78 ± 0.10
$ug \rightarrow tH$	1.29 ± 0.09	0.27 ± 0.03	0.94 ± 0.08	0.18 ± 0.03
tuH merged signal	6.44 ± 0.23	2.31 ± 0.11	6.76 ± 0.25	1.96 ± 0.11
	$211\tau_{had}1bnj$	$211\tau_{had}2bnj$	$l\tau_{had}\tau_{had}$	
data	2431.00 ± 49.31	862.00 ± 29.36	Blinded	
background	2574.74 ± 32.00	861.09 ± 10.85	339.71 ± 16.08	
$\bar{t}t \rightarrow bWcH$	25.77 ± 0.40	2.13 ± 0.11	52.35 ± 0.56	
$cg \rightarrow tH$	1.97 ± 0.04	0.06 ± 0.01	4.11 ± 0.05	
tCH merged signal	27.74 ± 0.40	2.20 ± 0.11	56.46 ± 0.56	
$\bar{t}t \rightarrow bWuH$	26.87 ± 0.41	0.54 ± 0.06	54.67 ± 0.58	
$ug \rightarrow tH$	9.57 ± 0.19	0.14 ± 0.02	19.03 ± 0.27	
tuH merged signal	36.44 ± 0.45	0.68 ± 0.06	73.71 ± 0.64	
	STH $\tau_{had}\tau_{had}$	TTH $\tau_{had}\tau_{had}$		
data	1047.00 ± 32.36	1116.00 ± 33.41		
background	1117.24 ± 14.83	1151.42 ± 14.81		
$\bar{t}t \rightarrow bWcH$	27.13 ± 0.59	82.52 ± 1.05		
$cg \rightarrow tH$	3.35 ± 0.07	4.49 ± 0.08		
tCH merged signal	30.47 ± 0.60	87.01 ± 1.06		
$\bar{t}t \rightarrow bWuH$	27.66 ± 0.58	85.91 ± 1.04		
$ug \rightarrow tH$	17.15 ± 0.33	22.35 ± 0.41		
tuH merged signal	44.82 ± 0.67	108.26 ± 1.12		

157 The inner-detector system (ID) is immersed in a 2 T axial magnetic field and provides charged particle
 158 tracking in the range $|\eta| < 2.5$. A high-granularity silicon pixel detector covers the vertex region and
 159 typically provides three measurements per track. It is followed by a silicon microstrip tracker, which usually
 160 provides four two-dimensional measurement points per track. These silicon detectors are complemented
 161 by a transition radiation tracker, which enables radially extended track reconstruction up to $|\eta| < 2.0$.
 162 The transition radiation tracker also provides electron identification information based on the fraction of
 163 hits above a higher energy-deposit threshold corresponding to transition radiation. Compared to Run-1,
 164 an Insertable B-Layer [23] (IBL) is inserted as the innermost pixel layer during LS1 for Run-2, which
 165 significantly improves the tracking performance.

166 The calorimeter system covers the pseudorapidity range $|\eta| < 4.9$. Within the region $|\eta| < 3.2$, electromagnetic
 167 calorimetry is provided by barrel and endcap high-granularity liquid-argon (LAr) electromagnetic
 168 calorimeters, with an additional thin LAr presampler covering $|\eta| < 1.8$, to correct for energy loss in
 169 material upstream of the calorimeters. Hadronic calorimetry is provided by a scintillator-tile calorimeter,
 170 segmented into three barrel structures within $|\eta| < 1.7$, and two LAr hadronic endcap calorimeters.

171 A muon spectrometer (MS) comprises separate trigger and high-precision tracking chambers measuring
 172 the deflection of muons in a magnetic field generated by superconducting air-core toroids. The precision
 173 chamber system covers the region $|\eta| < 2.7$ with three layers of monitored drift tubes, complemented by
 174 cathode strip chambers in the forward region, where the background is highest. The muon trigger system
 175 covers the range $|\eta| < 2.4$ with resistive-plate chambers in the barrel, and thin-gap chambers in the endcap
 176 regions.

177 5.2 Data set

178 This analysis is based on the full proton-proton data at a center-of-mass energy $\sqrt{s} = 13$ TeV with a bunch
 179 spacing of 25 ns collected by ATLAS in Run-2. The following good run list (GRL) was used for the 2015
 180 dataset:

181 data15_13TeV.periodAllYear_DetStatus-v89-pro21-02
 182 (Unknown_PHYS_StandardGRL_All_Good_25ns.xml

183 which corresponds to an integrated luminosity of 3.22 fb^{-1} .

184 The GRL used for the 2016 dataset:

185 data16_13TeV.periodAllYear_DetStatus-v89-pro21-01
 186 (DQDefects-00-02-04_PHYS_StandardGRL_All_Good_25ns.xml

187 corresponds to an integrated luminosity of 32.88 fb^{-1} .

188 These GRLs exclude data where the IBL was not fully operational. The uncertainty in the combined
 189 2015+2016 integrated luminosity, 36.1 fb^{-1} , is 2.1%. It is derived, following a methodology similar to
 190 that detailed in Ref. [24], from a calibration of the luminosity scale using x-y beam-separation scans
 191 performed in August 2015 and May 2016.

192 The GRL used for the 2017 dataset:

193 `data17_13TeV.periodAllYear_DetStatus-v99-pro22-01`
 194 `_Unknown_PHYS_StandardGRL_All_Good_25ns_Triggerno17e33prim.xml`

195 corresponds to an integrated luminosity of 44.307 fb^{-1} .

196 The GRL used for the 2018 dataset:

197 `data18_13TeV.periodAllYear_DetStatus-v102-pro22-04`
 198 `_Unknown_PHYS_StandardGRL_All_Good_25ns_Triggerno17e33prim.xml`

199 corresponds to an integrated luminosity of 59.937 fb^{-1} . The final luminosity used for the analysis is
 200 140.45 fb^{-1} .

201 **5.3 Signal and background simulation**

202 The overview of the major samples generated is summarized in table 5.

203 The TopFCNC UFO model [25, 26] with 5-flavour scheme is used for signal simulation.

204 The targeted signal in this analysis is tqH/tH with $H \rightarrow \tau\tau$ (samples 411170-411177 and 412098-412105)
 205 in App. A).

206 The FCNC ST signal is simulated using MadGraph5_aMC@NLO v2.6.2 [27] interfaced with Pythia 8
 207 [28] with the A14 tune [29] for the generation of parton showers, hadronisation and multiple interactions
 208 and the NNPDF30NLO [30] parton distribution functions (PDF) is used to generate qg events at next-to-
 209 leading order (NLO) in QCD. Depending on either up quark or charm quark involved in the FCNC decay
 210 and either the W bosons decaying hadronically or leptonically, 4 samples are generated for each term of
 211 effective Lagrangian, so eight samples in total.

212 The FCNC TT signal is simulated using Powheg-Box [31] V2 interfaced with Pythia8 [28] with the
 213 A14 tune [29] for the generation of parton showers, hadronisation and multiple interactions and the
 214 NNPDF30NLO [30] parton distribution functions (PDF) is used to generate $t\bar{t}$ events at next-to-leading
 215 order (NLO) in QCD. Depending on either the top or the anti-top quark decaying to bW , either up quark or
 216 charm quark involved in the FCNC decay and either the W bosons decaying hadronically or leptonically,
 217 eight samples are produced with the Higgs going to a τ -lepton pair.

- 218 Considering the other decays of the Higgs can be part of the signal, samples xxxxxx-xxxxxx (To be added
 219 with the samples used by tH bb/ML group) with inclusive W and Higgs decays are also included. These
 220 sample have a one-lepton (electron or muon) filter at truth level (either coming from W or Higgs decays).
 221 The events in xxxxxx-xxxxxx with $H \rightarrow \tau\tau$ decay are removed based on truth information.
- 222 It is checked that after the final selection, there are 110 overlapped signal events caused by different overlap
 223 removal and object definition in xTauFramework and ttHMultiAna (27140 in total for hadhad channel and
 224 95253 in total for lepton channels) but there is no overlap in the signal enriched region ($BDT > 0.5$).
 225 The total FCNC signal with fake taus in this analysis is not used in the MVA training, but is regarded as
 226 part of the total signal in the fit. The normalization factor of the other components is common with the
 227 signal, so that their yields are fully correlated in the fit.
- 228 The dominant background is the $t\bar{t}$ production. The $t\bar{t}$ process and the single top process are generated
 229 with Powheg-Box [31] V2, and Pythia8 is used for the parton shower. NNPDF30NLO [30] and A14
 230 tune [29] are used for $t\bar{t}$ (single top). The $t\bar{t}$ sample is also generated with different generators and parton
 231 showers models, as well as different amount of radiations, for systematics as detailed in Sec. 11.
 232 The $t\bar{t}X$, where $X=W, ee, \mu\mu, \tau\tau$ or $Z(qq, \nu\nu)$ are generated with MadGraph5_aMC@NLO and interfaced
 233 with Pythia8 for the parton shower. The NNPDF30NLO [30] is used for the matrix element PDF. The $t\bar{t}$,
 234 single top and $t\bar{t}X$ are combined into a single process named top background in the analysis.
- 235 The $W+$ jets, $Z+$ jets and diboson backgrounds are simulated using Sherpa 2.2.1 [32] with NNPDF30NNLO
 236 PDF [30].
 237 The τ decay in the single top samples is handled by Tauola [33]. All samples showered by Pythia8
 238 (Sherpa) have the τ decays also handled by Pythia8 (Sherpa). All the decay modes of the τ lepton are
 239 allowed in the event generators (but may be subject to generator filters). The summary of used generators
 240 for matrix element and parton shower is given in Table 5.
 241 The SM higgs background includes ggH , VH , VBF and $t\bar{t}H$, generated from Powheg-Box [31] V2
 242 interfaced with Pythia8. The overall contribution is pretty small. Various PDF and tune options are use
 243 for those samples depending on the decay modes.
 244 The tH associated production is negligible but we still considered it. The sample is generated using
 245 MadGraph5 and interfaced with pythia8 for parton shower. CT10 PDF and A14 tune are used. It is treated
 246 as part of SM higgs background explained in above.
 247 Except the major background $V+$ jets, $t\bar{t}$, SM higgs, Diboson, the other minor background are categorised
 248 into "Rare" processes in this analysis, which doesn't necessarily mean it's rare in the pp collision.
 249 All Monte-Carlo (MC) samples were passed through the full GEANT4 [34] simulation of the ATLAS
 250 detector, except for two extra $t\bar{t}$ samples with Pythia8 and Herwig7 [35] parton showering which are

Table 5: Overview of the MC generators used for the main signal and background samples

Process	Generator		PDF set		Tune	Order
	ME	PS	ME	PS		
TT Signal	Powheg	Pythia8	NNPDF30NLO	NNPDF23LO	A14	NLO
ST Signal	MadGraph5_aMC@NLO	Pythia8	NNPDF30NLO	NNPDF23LO	A14	NLO
$W/Z+jets$	Sherpa 2.2.1		NNPDF30NNLO		Sherpa	NLO/LO
$t\bar{t}$	Powheg	Pythia8	NNPDF30NLO	NNPDF23LO	A14	NLO
Single top	Powheg	Pythia6	CT10(NLO)	CTEQ6L1[44]	Perugia2012	NLO
$t\bar{t}X$	MadGraph5_aMC@NLO	Pythia8	NNPDF30NLO	NNPDF23LO	A14	NLO
Diboson	Sherpa 2.2.1		NNPDF30NNLO		Sherpa	NLO/LO

251 simulated with ATLFAST-II [36] for systematics (Sec. 11). In the analysis, the simulated events were
 252 reweighted based on their pile-up to match the pile-up profile observed in data.

253 The full list of MC samples are given in App. A. The single boson and diboson cross sections are
 254 calculated to NNLO [37]. The $t\bar{t}$ cross section is calculated at NNLO in QCD including resummation
 255 of NNLL soft gluon terms for a top-quark mass of 172.5 GeV [38]. The $t\bar{t}H$ and $t\bar{t}V$ are normalized to
 256 NLO cross sections according to [39] and [40]. The t -channel and s -channel single top cross sections are
 257 calculated at NLO with Hathor v2.1 [41, 42], while the Wt channel is calculated at NLO+NNLL [43].

258 6 Object reconstruction

259 In this section, various objects used in this analysis are defined, namely jets, electrons, muons, hadronically
 260 decaying taus and missing transverse energy.

261 6.1 Jets

262 Jets are reconstructed using the anti- k_t algorithm [45] with a distance parameter $R = 0.4$ applied to the
 263 particle flow candidates. Only jets with $p_T > 25$ GeV and $|\eta| < 4.5$ are considered by the E_T^{miss} calculation
 264 and overlap removal procedure. To suppress jets produced in additional pile-up interactions, jets with
 265 $p_T < 60$ GeV and $|\eta| < 2.4$ are required to have a Jet Vertex Tagger (JVT [46]) parameter larger than
 266 0.2 (Medium working point). The JVT is the output of the jet vertex tagger algorithm used to identify
 267 and select jets originating from the hard-scatter interaction through the use of tracking and vertexing
 268 information. About 10% of selected jets in the signal are in the forward detector region. After the above
 269 selection and overlap removal, a “jet cleaning” cut performed by JetCleaningTool with LooseBad working
 270 point is applied on all the jets, and the events with jets not passing this cut are discarded. Only the central
 271 jets with $|\eta| < 2.4$ are considered in the analysis to reject pile-up contamination.

272 6.2 b-tagging

273 The DL1r [47] algorithm is used to identify the jets initiated by b -quarks. A working point corresponding
 274 to an average efficiency of 70% for jets containing b -quarks is chosen.

275 6.3 Light leptons

276 Electron candidates are identified by tracks reconstructed in the inner detector and the matched cluster of
 277 energy deposited in the electromagnetic calorimeter. Electrons candidates are required to have $E_T > 15$
 278 GeV and $|\eta| < 2.47$. The transition region, $1.37 < |\eta| < 1.52$, between the barrel and end-cap calorimeters
 279 is excluded. They are further required to pass a loose + b-layer likelihood-based identification point
 280 [48] and a FCLoose isolation working point [49]. The electrons are further removed if its cluster is
 281 affected by the presence of a dead frontend board in the first or second sampling or by the presence of a
 282 dead high voltage region affecting the three samplings or by the presence of a masked cell in the core. The
 283 electron is required to be consistent with the primary vertex by imposing on the trasverse impact parameter
 284 significance ($|d_0|/\sigma_{d0} < 5$) and the longituinal impact parameter ($|\Delta z_0 \sin\theta_l| < 0.5$ mm) cuts.

285 Muon reconstruction begins with tracks reconstructed in the MS and is matched to tracks reconstructed
 286 in the inner detector. Muon candidates are required to have $p_T > 10$ GeV and $|\eta| < 2.5$. A Loose
 287 identification selection [50] based on the requirements on the number of hits in the ID and the MS
 288 is satisfied. A FCLoose isolation [49] criterion is also required. The transverse impact parameter
 289 requirement for muon is slightly tighter than for electron ($|d_0|/\sigma_{d0} < 3$), while the longitudinal impact
 290 parameter selection is the same.

291 Tight isolation working points are also applied in some channels to reduce fake and non-prompt lepton
 292 contributions based a trained isolation boosted decision tree `PromptLeptonVeto` (PLV), as described in
 293 Sec. 6.6.

294 6.4 Hadronic tau decays

295 The hadronic tau candidates [51] are seeded by jets reconstructed by the anti- k_t algorithm [45], which
 296 is applied on calibrated topo clusters [52] with a distance parameter of R=0.4. They are required to
 297 have $p_T > 20$ GeV and $|\eta| < 2.5$. The transition region between the barrel and end-cap calorimeters
 298 ($1.37 < |\eta| < 1.52$) is excluded.

299 In the hadronic channels, these tau candidates are considered in the overlap removal procedure and
 300 missing transverse energy calculation, following the Htautau group [53]. In the analysis event selection,
 301 the hadronic tau candidates are required to have one or three charged tracks and an absolute charge of one.

302 An identification algorithm based on Recursive Neural Network (RNN) [54] is applied to discriminate the
 303 visible decay products of hadronically decaying tau lepton τ_{had} from jets initiated by quarks or gluons.
 304 Different RNN working points are used at different levels depending on the analysis channel. Only events
 305 with RNN Medium taus are considered to be signal in the hadronic channels while loose taus are only
 306 used in the control regions for fake tau estimation.

307 In the leptonic channels, the taus passing the RNN Medium working point are considered in the overlap
 308 removal procedure and missing transverse energy calculation, following the ttW multi-lepton group [55].

309 For the Medium ID, the tau efficiency is about 75% (60%) for 1-prong (3-prong) candidates. The ID
 310 efficiencies are optimized to be flat versus the tau p_T and pileup.

311 The tau candidates are required to not overlap with a very loose electron candidate, and a dedicated BDT
 312 variable is also used to veto the taus which are actually electrons.

313 Efficiency scale factors for tau reconstruction, ID and electron BDT rejection [56] are applied on tau
 314 candidates in MC.

315 6.5 Missing transverse energy

316 The missing transverse energy E_T^{miss} is computed using the fully calibrated and reconstructed physics
 317 objects as described above. The TrackSoftTerm (TST) algorithm is used to compute the SoftTerm of the
 318 E_T^{miss} [57].

319 6.6 Tight lepton isolation: **PromptLeptonVeto(PLV)**

320 A dedicated isolation boosted decision tree has been trained to better reject non-prompt leptons and
 321 fakes produced in hadron decays [58]. The main idea is to identify non-prompt light leptons using
 322 lifetime information associated with a track jet that matches the selected light lepton. These additional
 323 reconstructed charged particle tracks inside the jet can be used to increase the precision of identifying the
 324 displaced decay vertex of heavy flavor (b, c) hadrons that produced a non-prompt leptons.

325 **PromptLeptonVeto** is trained on leptons selected from the Powheg+Pythia8 non-allhad $t\bar{t}$ sample using
 326 eight input variables:

- 327 • Three of them are used to identify b-tagged jets by ATLAS flavor tagging algorithms;
- 328 • Two of them are the ratio of the track lepton p_T with respect to the track jet p_T and ΔR between the
 329 lepton and the track jet axis;

- 330 • Three of them are the number of tracks collected by the track jet and the lepton track and calorimeter
331 isolation variables.
- 332 The **PromptLeptonVeto** shows a significant improvement for non-prompt-lepton rejection compared to
333 the cut-based isolation variables.
- 334 The tight working points are: **PromptLeptonVeto**< -0.50 for muons and **PromptLeptonVeto**< -0.70
335 for electrons. The efficiencies of the tight **PromptLeptonVeto** working points are measured using the
336 tag and probe method with $Z \rightarrow l^+l^-$ events. The scale factors are approximately 0.92 for $10 < p_T < 15$
337 GeV muons and 0.97 for electrons, and averaging at 0.98 to 0.99 for higher p_T leptons.
- 338 There is a new improved PLV or PLIV available sooner and we will update the tight isolation working
339 point cut accordingly in next update.

340 6.7 Overlap removal

- 341 For the objects passing the selection above, a geometric overlap removal is applied to eliminate the
342 ambiguity in the object identification. When two objects are close geometrically with ΔR less than a
343 certain threshold, or satisfy some certain requirements, one of them will be removed.
- 344 In the hadronic channels, the overlap removal is done by the official overlap removal tool provided by
345 ASG group. The "Standard" working point is used. The rules are discribed as follows in sequence:
- 346 • If two electrons have overlapped second-layer cluser, or shared tracks, the electron with lower p_T is
347 removed.
 - 348 • τ_{had} within a $\Delta R = 0.2$ cone of an electron or muon are removed.
 - 349 • If a muon sharing an ID track with an electron and the muon is calo-tagged, the muon is removed.
350 Otherwise the electron is removed.
 - 351 • Jets within a $\Delta R = 0.2$ cone of an electron are removed.
 - 352 • Electrons within a $\Delta R = 0.4$ cone of a jet are removed.
 - 353 • When a muon ID track is ghost associated to a jet or within a $\Delta R = 0.2$ cone of a jet, the jet
354 is removed if it has less than 3 tracks with $p_T > 500$ MeV or has a relative small p_T ($p_T^\mu >$
355 $0.5p_T^{\text{jet}}$ and $p_T^\mu > 0.7$ [the scalar sum of the p_T 's of the jet tracks with $p_T > 500$ MeV]).
 - 356 • Muons within a $\Delta R = 0.4$ cone of a jet are removed.
 - 357 • Jets within a $\Delta R = 0.2$ cone of the leading τ_{had} ($\tau_{\text{lep}}\tau_{\text{had}}$), or with the two leading τ_{had} 's ($\tau_{\text{had}}\tau_{\text{had}}$),
358 are excluded. The overlap also works for the reverted tau ID regions used in the analysis, since the
359 tau ID information is not used.

- 360 • If a tau candidate is tagged as b-jet with 70% working point, the tau is removed.
- 361 In the leptonic channels, the overlap removal is done using the heavy flavor overlap removal working point,
 362 which gives precedence to the b-tagged jet as follows:
- 363 • If two electrons have overlapped second-layer cluster, or shared tracks, the electron with lower p_T is
 364 removed.
- 365 • τ_{had} within a $\Delta R = 0.2$ cone of an electron or muon are removed.
- 366 • If a muon sharing an ID track with an electron and the muon is calo-tagged, the muon is removed.
 367 Otherwise the electron is removed.
- 368 • Jet is not tagged as b-jet and within a $\Delta R = 0.2$ cone of an electron is removed.
- 369 • When a muon ID track is ghost associated to a jet or within a $\Delta R = 0.2$ cone of a jet, the jet is removed
 370 if it is not tagged as b-jet and has either less than 3 tracks with $p_T > 500$ MeV or has a relative small
 371 p_T ($p_T^\mu > 0.5 p_T^{\text{jet}}$ and $p_T^\mu > 0.7$ [the scalar sum of the p_T 's of the jet tracks with $p_T > 500$ MeV]).
- 372 • Muons within a $\Delta R = 0.4$ cone of a jet are removed.
- 373 • Jet is not tagged as b-jet and within a $\Delta R = 0.2$ cone of the τ_{had} is removed. The overlap also works
 374 for the reverted tau ID regions used in the analysis.
- 375 • The event is removed if a tau candidate is tagged as b-jet with 70% working point.
- 376 The rest of overlap removal procedures are the same as used in the hadronic channels above. Note that the
 377 E_T^{miss} calculation package has its own overlap removal procedure. Only two leading taus are considered
 378 in the calculation.

379 7 Signal regions

380 In the leptonic channels, the p_T of the lepton is required to be 1 GeV above the trigger threshold. The
 381 leptons are required to have **Tight ID** as defined in Sec. 6. The trigger matching between the offline and
 382 trigger level lepton objects is also required for the corresponding leptons selected for the analysis.

383 In the hadronic channels, the two tau candidates with the highest p_T are chosen. They should also pass
 384 the **Medium tau ID** and overlap removal. To account for the trigger thresholds, the two hadronic taus are
 385 required to pass the $p_T > 40$ GeV and $p_T > 30$ GeV cuts.

386 The details of implementation of the event selection before the n-tuples and n-tuple level object quality
 387 cuts are listed in the [B](#).

388 7.1 Trigger

389 In the leptonic channels, the single-lepton triggers are required to select the candidate events. In general,
 390 the lowest unprescaled triggers are used in every data-taking periods:

391 Single electron:

- 392 • 2015: HLT_e24_lhmedium_L1EM20VH
- 393 HLT_e60_lhmedium, HLT_e120_lhloose
- 394 • 2016, 2017, 2018: HLT_e26_lhtight_nod0_ivarloose
- 395 HLT_e60_lhmedium_nod0, HLT_e140_lhloose_nod0

396 Single muon:

- 397 • 2015: HLT_mu20_iloose_L1MU15, HLT_mu50
- 398 • 2016, 2017, 2018: HLT_mu26_ivarmedium, HLT_mu50

399 The di-lepton control regions to estimate fake taus are required to pass di-lepton triggers:

400 Di-electron:

- 401 • 2015: HLT_2e12_lhloose_L12EM10VH
- 402 • 2016: HLT_2e17_lhvloose_nod0
- 403 • 2017, 2018: HLT_2e24_lhvloose_nod0

404 Di-muon:

-
- 405 • 2015: HLT_mu18_mu8noL1
 406 • 2016, 2017, 2018: HLT_mu22_mu8noL1

407 Election+Muon:

- 408 • 2015: HLT_e17_lhloose_mu14
 409 • 2016, 2017, 2018: HLT_e17_lhloose_nod0_mu14

410 The trigger used for hadronic channels in each year are listed as follow:

- 411 • 2015: HLT_tau35_medium1_tracktwo_tau25_medium1_tracktwo_L1TAU20IM_2TAU12IM
 412 • 2016: HLT_tau35_medium1_tracktwo_tau25_medium1_tracktwo
 413 • 2017: HLT_tau35_medium1_tracktwo_tau25_medium1_tracktwo_03dR30_L1DR_TAU20ITAU12I_J25
 414 • 2018: HLT_tau35_medium1_tracktwoEF_tau25_medium1_tracktwoEF_03dR30_L1DR_TAU20ITAU12I_J25

415 The two τ_{had} candidates are matched to the respective legs of the di-tau trigger using the individual single
 416 tau trigger objects. The p_T thresholds are chosen such that the selected τ_{had} candidate p_T already lies
 417 in the plateau of the respective trigger efficiency curve. Due to the rising instantaneous luminosity, the
 418 trigger used in the 2016-2018 data taking includes a requirement for an additional level-1 calorimeter
 419 trigger jet . The leading jet in those events is required to be matched within $\Delta R < 0.4$ with the jet ROI
 420 that fulfilled the jet part of the trigger criteria (trigger jet). The $p_T > 60 \text{ GeV}$ cut is applied to make sure
 421 that the jet is in the trigger p_T plateau.

422 For the TT channel tcH coupling search, the FCNC jet is from a c-quark. Regarding the similarity between
 423 the b-jet and c-jet, the very loose b-tagging is attempted on the FCNC jet in order to further select the tcH
 424 signal. However, the dominating background is $t\bar{t}$ where there are 2 b-jets. This resort does not help with
 425 the significance.

426 7.2 Cuts

427 Kinematics cuts are carefully selected to reduce background and provide control region for fake tau
 428 estimation in the hadronic channels:

- 429 • $m_{\tau\tau,\text{vis}} > 60$
 430 • $m_{\tau\tau,\text{vis}} < 120$
 431 • $\Delta R(\tau, \tau) < 3.4$
 432 • $100 \text{ GeV} < m_{\tau\tau} < 150 \text{ GeV}$

433 • $m_{t,FCNC} > 140\text{GeV}$

434 The S/B is significantly improved after applying these cuts as shown in Table 23 and 24.

435 In the leptonic channels, except $l\tau_{\text{had}}\tau_{\text{had}}$, a $E_T^{\text{miss}} > 20\text{GeV}$ cut and PLV tight is used to reduce QCD
436 background and also provide QCD enriched control regions.

437 The yields of signal regions are shown in Table ?? for leptonic channels and ?? for hadronic channels.

438 The yield of the CR generated are shown in Table ??.

439 8 Reconstruction of event topology

440 To comply with the signal topology, in each channel, exactly one jet should be tagged as a b -jet.

441 In TTH channels, all jets from the top hadronic decay and the jet from $t \rightarrow Hq$, denoted as the FCNC jet,
 442 pass the jet selection, there should be at least four jets among which the one with smallest $\Delta R(p_{\text{jet}}^\mu, p_{\tau_1}^\mu + p_{\tau_2}^\mu)$
 443 is considered as FCNC jet. If there are more than 2 jets beside FCNC jet and b -jet, the jets from W boson
 444 decay are chosen from the combination which have the invariant mass closest to W resonance. There is
 445 the chance that one of the jets fails the p_T requirement and not reconstructed. This kind of events will fall
 446 into STH channel. The FCNC top resonance is still reconstructed given the big chance that the jet which
 447 is missing is from W decay.

448 In STH events, there are 3 jets coming from top decay including the b -jet. So a Higgs resonance formed
 449 by the taus and a top resonance formed by the jets are expected.

450 In STH and TTH channels, the χ^2 fit is used to reconstruct the ditau mass and momentum by taking the
 451 τ decay kinematics into account. To determine the 4-momenta of the invisible decay products of the tau
 452 decays, the following χ^2 in Eq. 3, based on the collinear approximation is used.

$$\chi^2 = \left(\frac{m_H^{\text{fit}} - 125}{\sigma_{\text{Higgs}}} \right)^2 + \left(\frac{E_{x,\text{miss}}^{\text{fit}} - E_{x,\text{miss}}}{\sigma_{\text{miss}}} \right)^2 + \left(\frac{E_{y,\text{miss}}^{\text{fit}} - E_{y,\text{miss}}}{\sigma_{\text{miss}}} \right)^2, \quad (3)$$

453 In Eq. 3, the free parameters scanned are the energy ratio of invisible decay products for each tau decay.
 454 The Higgs mass resolution is set to 20 GeV according to the [59]. The E_T^{miss} resolution is parametrized as

$$\sigma_{\text{miss}} = 13.1 + 0.50\sqrt{\Sigma E_T}, \quad (4)$$

455 where ΣE_T (in GeV) is the scalar sum of transverse energy depositions of all objects and clusters. The
 456 invisible 4-momenta are obtained by minimizing the combined χ^2 for each event. By adding the Higgs
 457 mass constraint term in the kinematic fit, not only is the Higgs mass resolution improved, but also the
 458 resolutions of the Higgs boson's four-momentum, and the mass of the top from which the Higgs comes.
 459 Figure 2 shows the distributions of χ^2 in different regions. Good agreement between data and background
 460 predictions are achieved.

462 In $l\tau_{\text{had}}\tau_{\text{had}}$ channels, a Higgs resonance formed by the taus is expected. Additionally for TTL $\tau_{\text{had}}\tau_{\text{had}}$
 463 events, a top resonance formed by the c/u jet and Higgs is expected.

464 Due to the large amount of neutrinos produced in leptonic channels with a huge degree of freedom. The
 465 kinematic fit to reconstruct the neutrinos is given up in $l\tau_{\text{had}}\tau_{\text{had}}$ and $l\tau_{\text{had}}$ channels. The kinematics
 466 calculated directly from visible particles and E_T^{miss} are used as BDT input.

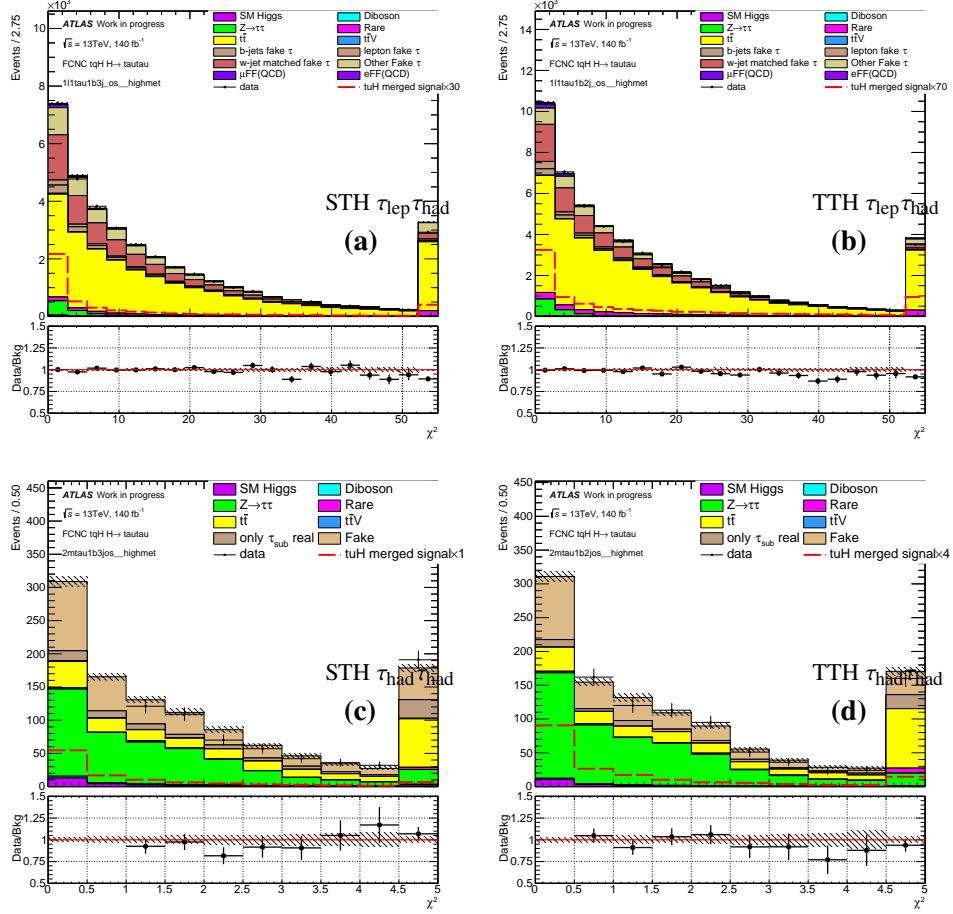


Figure 2: The distributions of χ^2 in Eq. 3 in the hadronic channels.

With the event topology reconstructed, a number of variables are defined for signal and background separation. Their distributions can be found in Sec. 9, and some of their explanations are as follows. In the following explanations, di-tau point to the visible decay product of both τ_{had} and τ_{lep} .

1. E_{miss}^T is the missing transverse momentum.
2. $p_{T,\tau}$ is the transverse momentum of the leading tau candidate.
3. $p_{T,\text{sub}-\tau}$ is the transverse momentum of the sub-leading tau candidate.
4. $p_{T,l}$ is the transverse momentum of the leading lepton.
5. χ^2 is derived from kinematic fitting for the neutrinos.
6. $m_{t,SM}$ is the invariant mass of the b -jet and the two jets from the W decay, and reflects the top mass in the decay $t \rightarrow Wb \rightarrow j_1 j_2 b$. This variable is only defined for the 4-jet STH and TTH events.

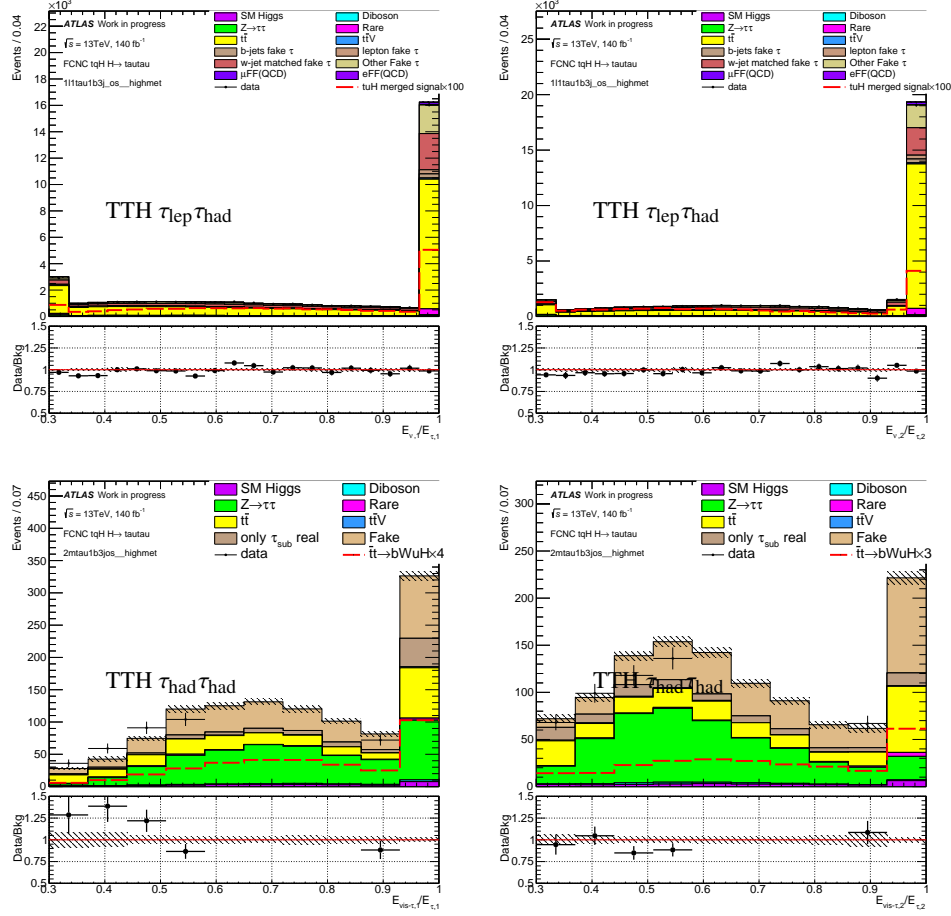


Figure 3: The distributions of $E_{\nu,i}/E_{\tau,i}$, $i = 1, 2$ in the TTH $\tau_{lep}\tau_{had}$ (top) and $\tau_{had}\tau_{had}$ (bottom) channels.

477 7. m_W^T is the transverse mass calculated from the lepton and E_T^{miss} in the leptonic channels, defined as

$$m_W^T = \sqrt{2p_{T,\text{lep}}E_T^{\text{miss}}(1 - \cos \Delta\phi_{\text{lep,miss}})}. \quad (5)$$

478 8. $m_{\tau,\tau}$ is the invariant mass of the tau candidates and reconstructed neutrinos in STH and TTH
479 channels.

480 9. m_W is the reconstructed invariant mass of the hadronic W boson from SM top quark.

481 10. $m_{t,FCNC}$ is the visible invariant mass of the FCNC-decaying top quark reconstructed from di-tau
482 candidates, FCNC-jet and reconstructed neutrinos.

483 11. $m_{\tau\tau,vis}$ is the visible invariant mass of the di-tau candidates

484 12. $p_{T,\tau\tau,vis}$ is the p_T of the di-tau candidates.

485 13. $m_{t,FCNC,vis}$ is the reconstructed visible mass of the FCNC-decaying top quark.

- 486 14. $m_{t,SM,vis}$ is the invariant mass of the lepton and the b-jet, which reflects the visible SM top mass.
- 487 15. $M(\tau\tau light - jet, min)$ is the visible mass of the di-tau candidates (include leptonic tau) and the
488 light-flavor jet, minimized by choosing different jet, reflects the invariant masss of the visible FCNC
489 top decaying product, an alternative of variable $m_{t,FCNC,vis}$.
- 490 16. $M(light - jet, light - jet, min)$ is the invariant mass of two light-flavor jet, minimized by choosing
491 different jets, reflects the invariant mass of the W candidate, an alternative of m_W .
- 492 17. E_{miss}^T centrality is a measure of how central the E_T^{miss} lies between the two tau candidates in the
493 transverse plane, and is defined as

$$\begin{aligned} E_T^{\text{miss}} \text{ centrality} &= (x + y) / \sqrt{x^2 + y^2}, \\ \text{with } x &= \frac{\sin(\phi_{\text{miss}} - \phi_{\tau_1})}{\sin(\phi_{\tau_2} - \phi_{\tau_1})}, y = \frac{\sin(\phi_{\tau_2} - \phi_{\text{miss}})}{\sin(\phi_{\tau_2} - \phi_{\tau_1})}, \end{aligned} \quad (6)$$

- 494 18. $E_{\nu,i}/E_{\tau,i}, i = 1, 2$ is the momentum fraction carried by the visible decay products from the tau
495 mother. It is based on the best-fit 4-momentum of the neutrino(s) according to the event reconstruc-
496 tion algorithm in this section. For the τ_{had} decay mode, the visible decay products carry most of
497 the tau energy since there is only a single neutrino in the final state, which is evident in the excess
498 around 1 in Figure 3.
- 499 19. $\Delta R(l + b - jet, \tau + \tau)$ is the angular distance between the lepton+b-jet and di-tau candidates.
- 500 20. $\Delta R(l, b - jet)$ is the angular distance between the lepton and b-jet.
- 501 21. $\Delta R(\tau, b - jet)$ is the angular distance between the tau and b-jet. If there are two taus in the event,
502 the leading one is selected for the calculation.
- 503 22. $\eta_{\tau,max}$ is the maximum η value among the tau candidates.
- 504 23. $\Delta R(l, \tau)$ is the angular distance between the lepton and the closest tau candidate in the leptonic
505 channels.
- 506 24. $\Delta R(\tau, fcnc - j)$ is the angular distance between the tau and the reconstructed fcnc jet.
- 507 25. $\Delta R(\tau, \tau)$ is the angular distance between two tau candidates, in case of $STH/TTH\tau_{\text{lep}}\tau_{\text{had}}$ channel,
508 the definition is the same as $\Delta R(l, \tau)$.
- 509 26. $\Delta\phi(\tau\tau, P_{miss}^T)$ is the azimuthal angle between the E_T^{miss} and di-tau p_T .

510 The distributions of those variables are shown in:

- 511 • $l\tau_{\text{had}}$ 1j: Figure 4 - 5
- 512 • $l\tau_{\text{had}}$ 2j: Figure 6 - 8
- 513 • STH $\tau_{\text{lep}}\tau_{\text{had}}$: Figure 9 - 11

- 514 • TTH $\tau_{\text{lep}}\tau_{\text{had}}$: Figure 12 - 14
- 515 • $l\tau_{\text{had}}\tau_{\text{had}}$: Figure 15 - 16
- 516 • STH $\tau_{\text{had}}\tau_{\text{had}}$: Figure 17 - 18
- 517 • TTH $\tau_{\text{had}}\tau_{\text{had}}$: Figure 19 - 20

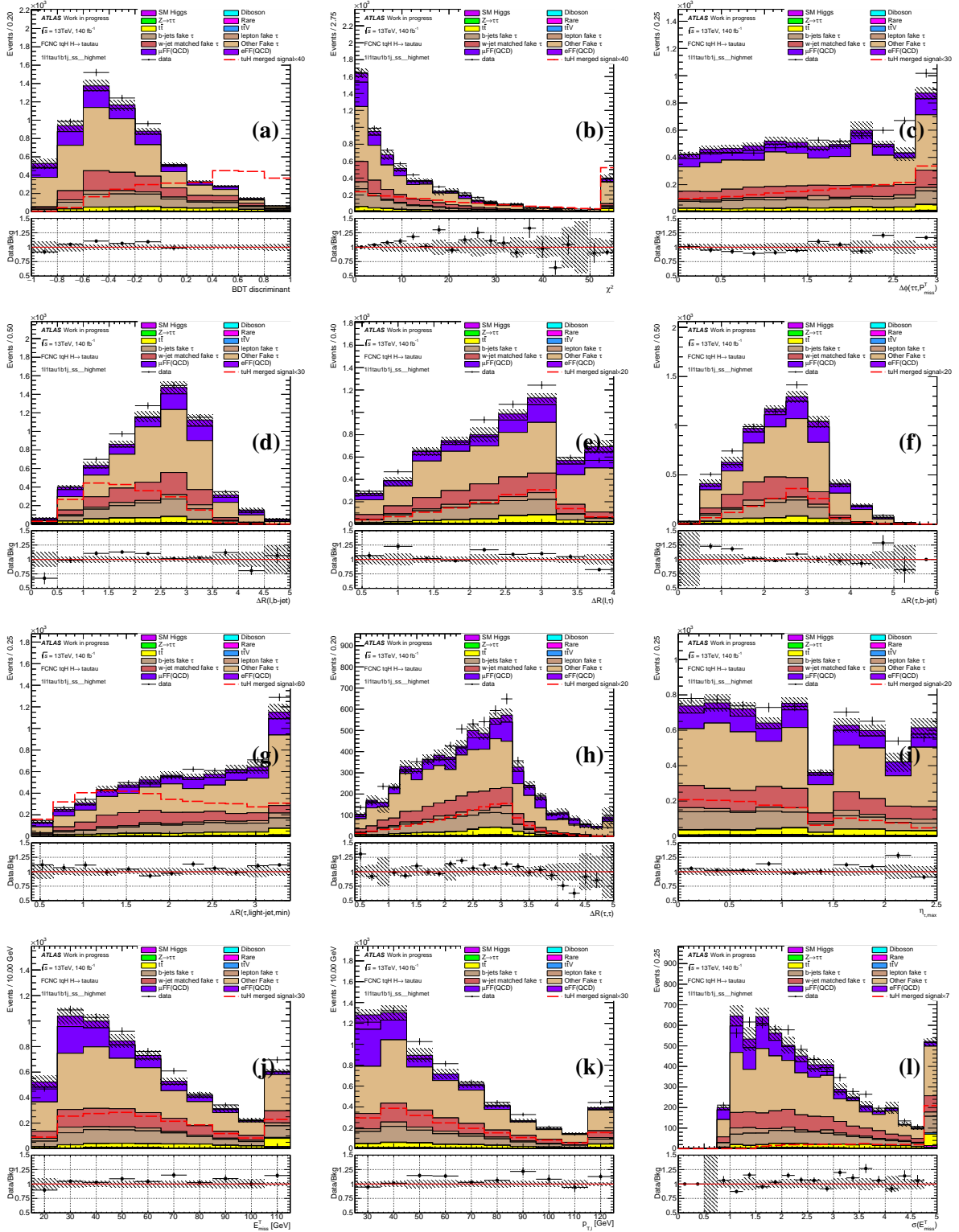


Figure 4: The variables distributions for the background and merged tuH signal in the $l\tau_{\text{had}} 1j$

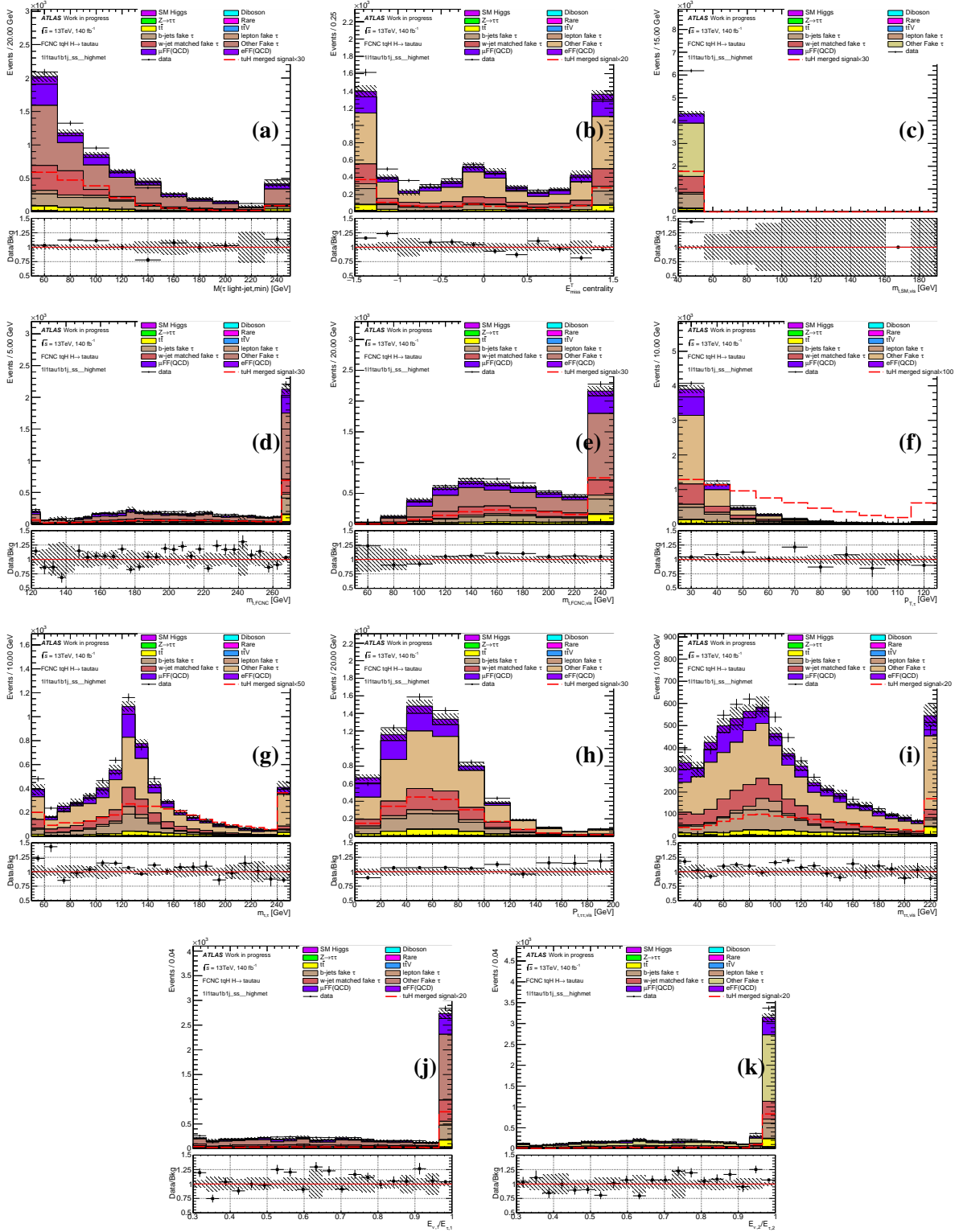
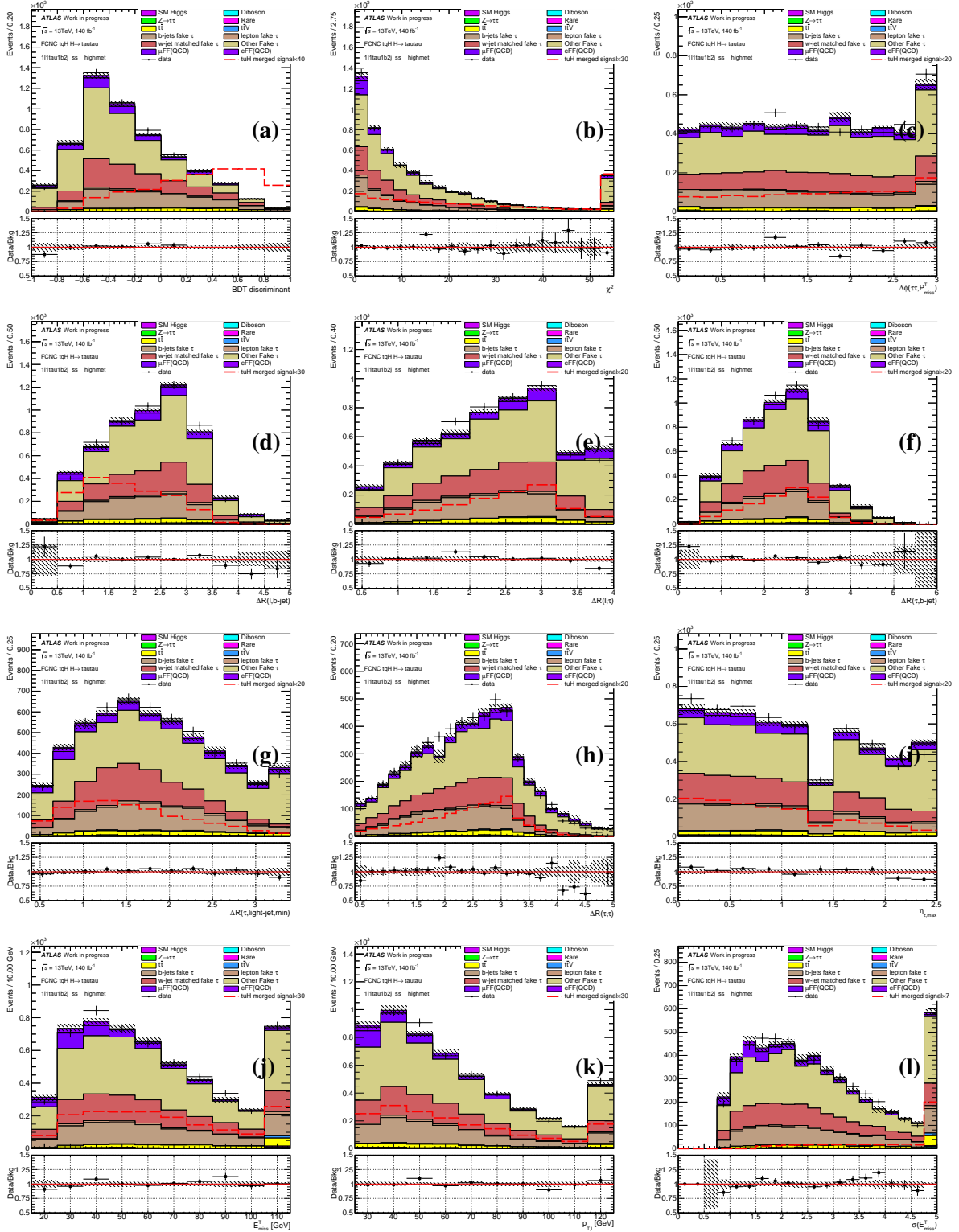


Figure 5: The variables distributions for the background and merged tuH signal in the $l\tau_{\text{had}} 1j$

Figure 6: The variables distributions for the background and merged tuH signal in the $l\tau_{\text{had}} 2j$

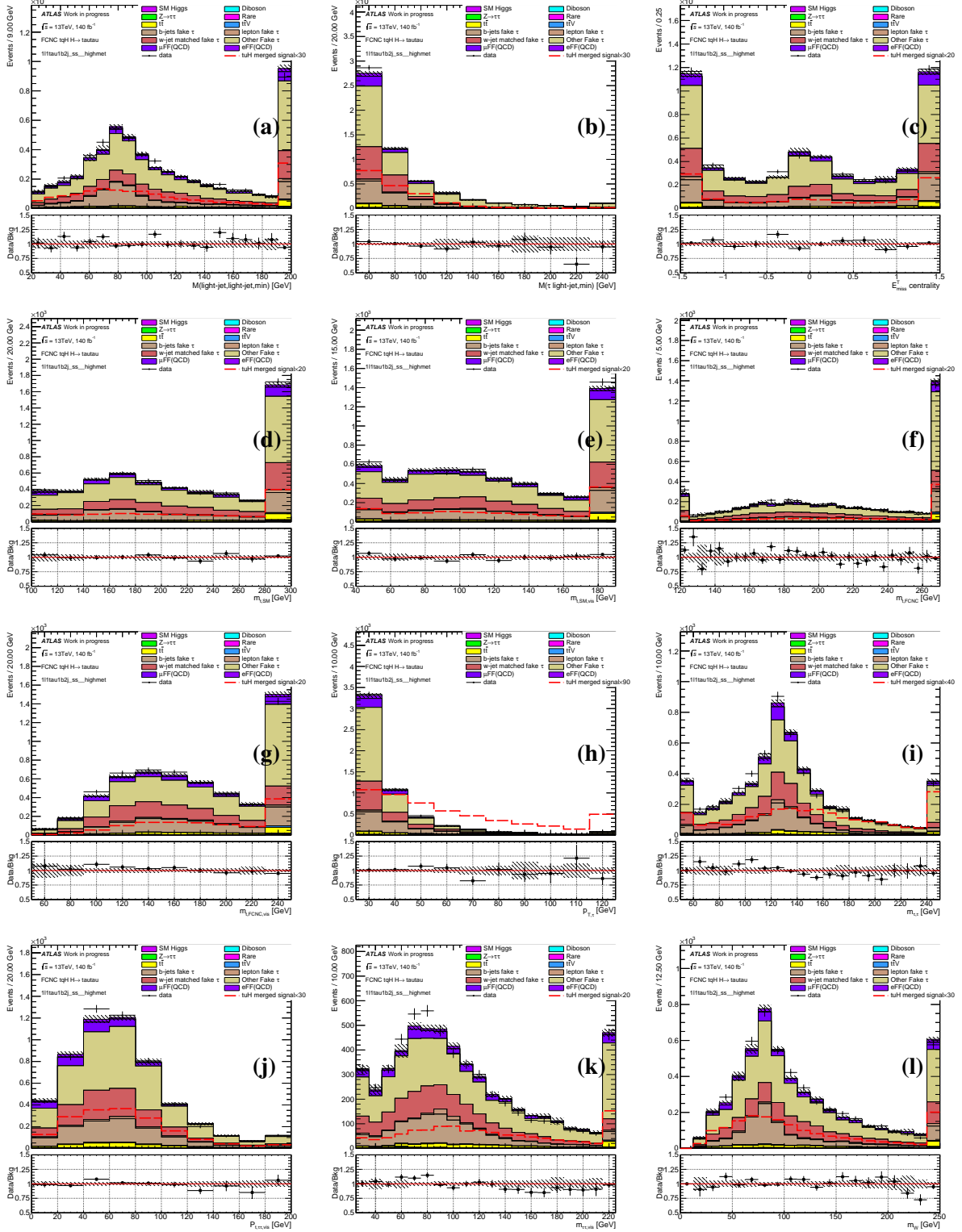


Figure 7: The variables distributions for the background and merged tuH signal in the $l\tau_{\text{had}} 2j$

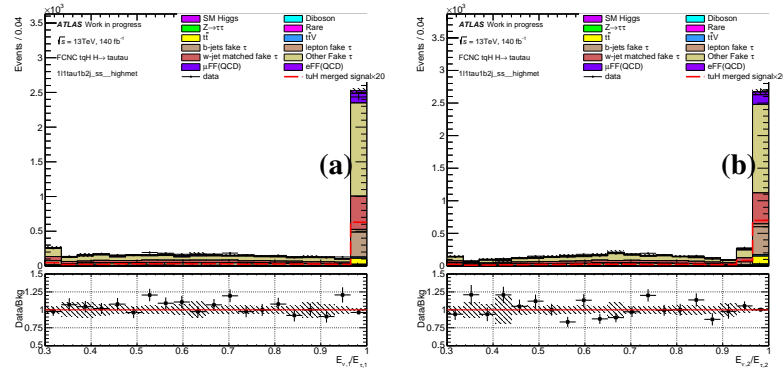
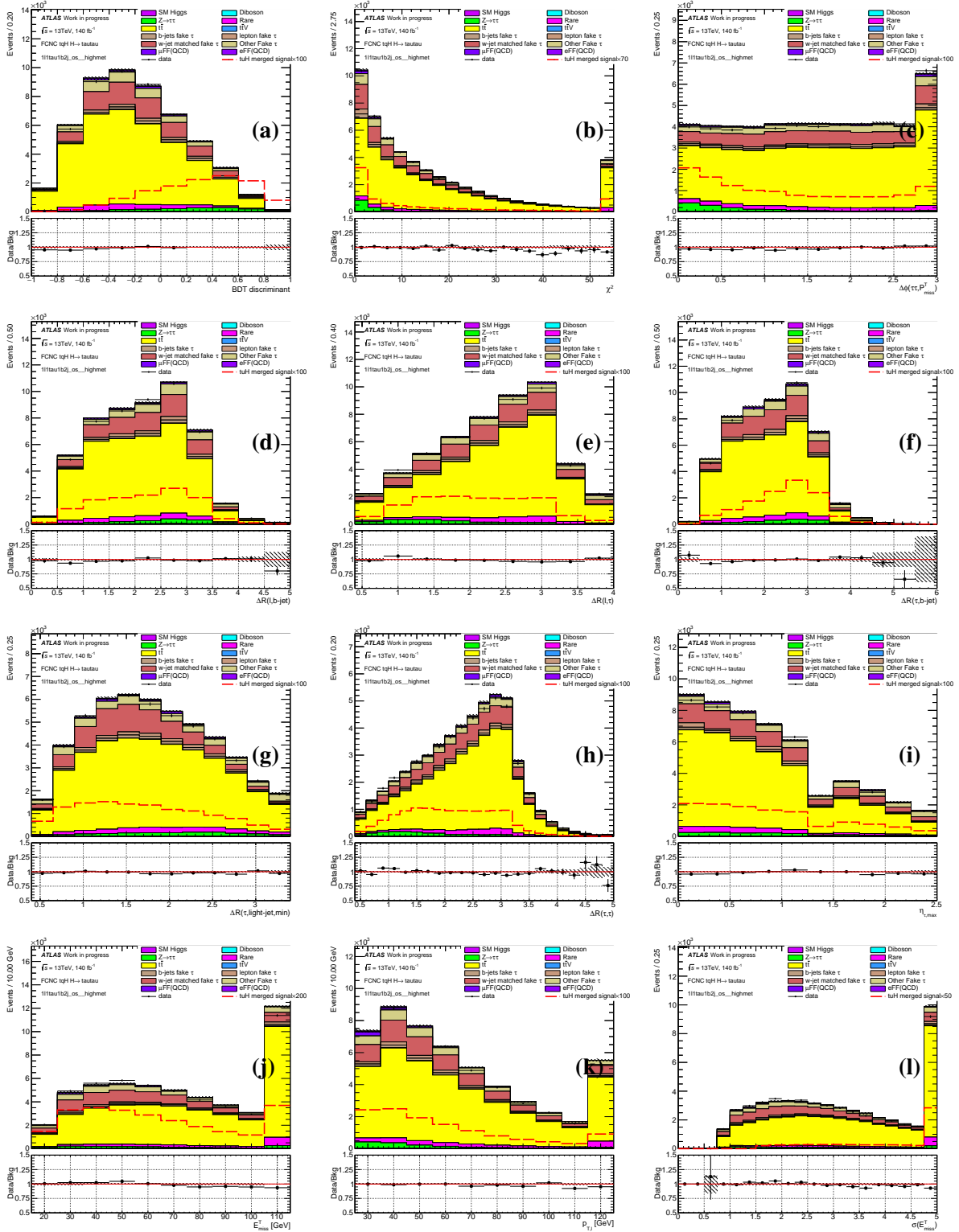


Figure 8: The variables distributions for the background and merged tuH signal in the $l\tau_{\text{had}} 2j$

Figure 9: The variables distributions for the background and merged tuH signal in the STH $\tau_{\text{lep}}\tau_{\text{had}}$

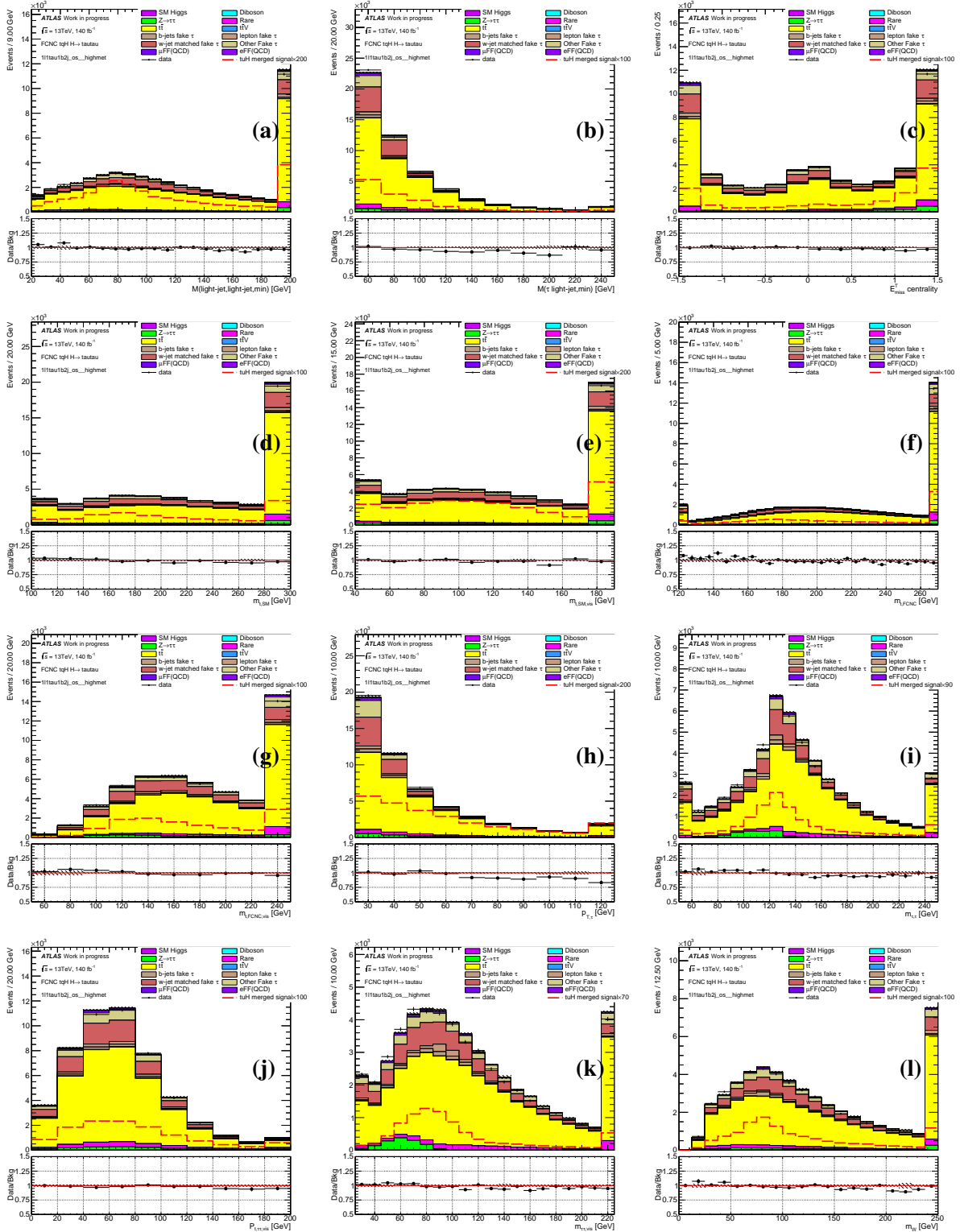


Figure 10: The variables distributions for the background and merged tuH signal in the STH $\tau_{\text{lep}} \tau_{\text{had}}$

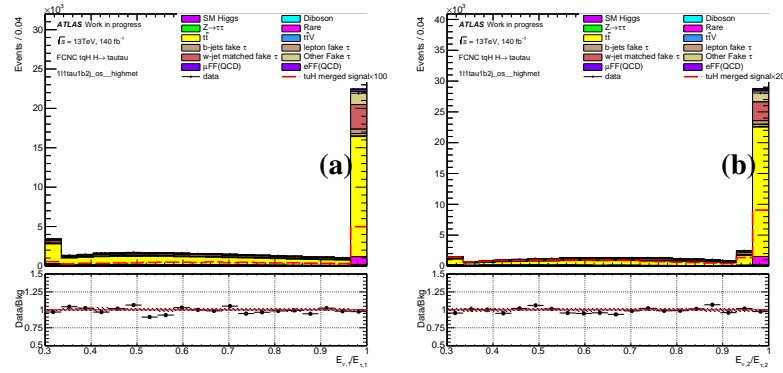


Figure 11: The variables distributions for the background and merged tuH signal in the STH $\tau_{\text{lep}}\tau_{\text{had}}$

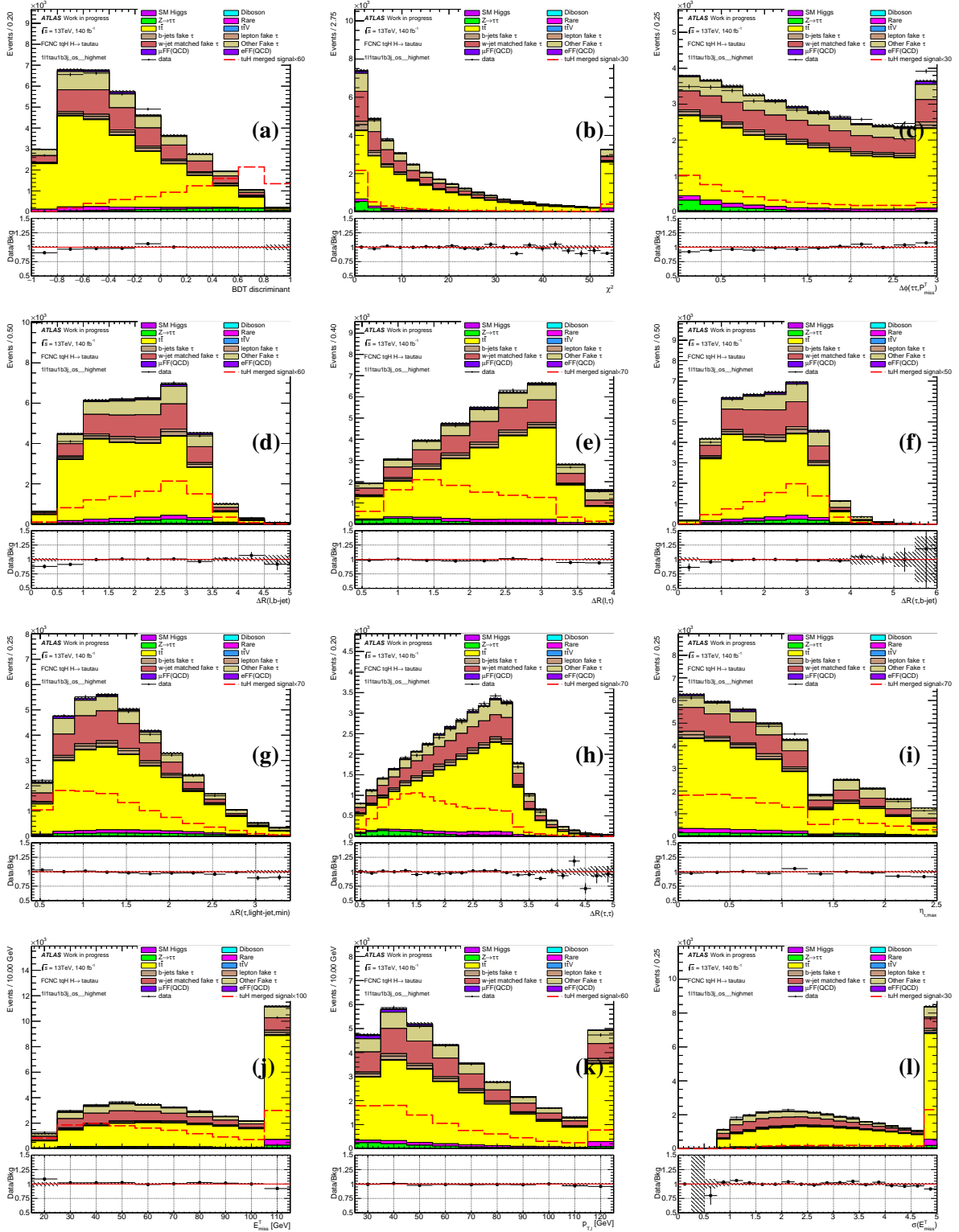


Figure 12: The variables distributions for the background and merged tuH signal in the TTH $\tau_{\text{lep}}\tau_{\text{had}}$

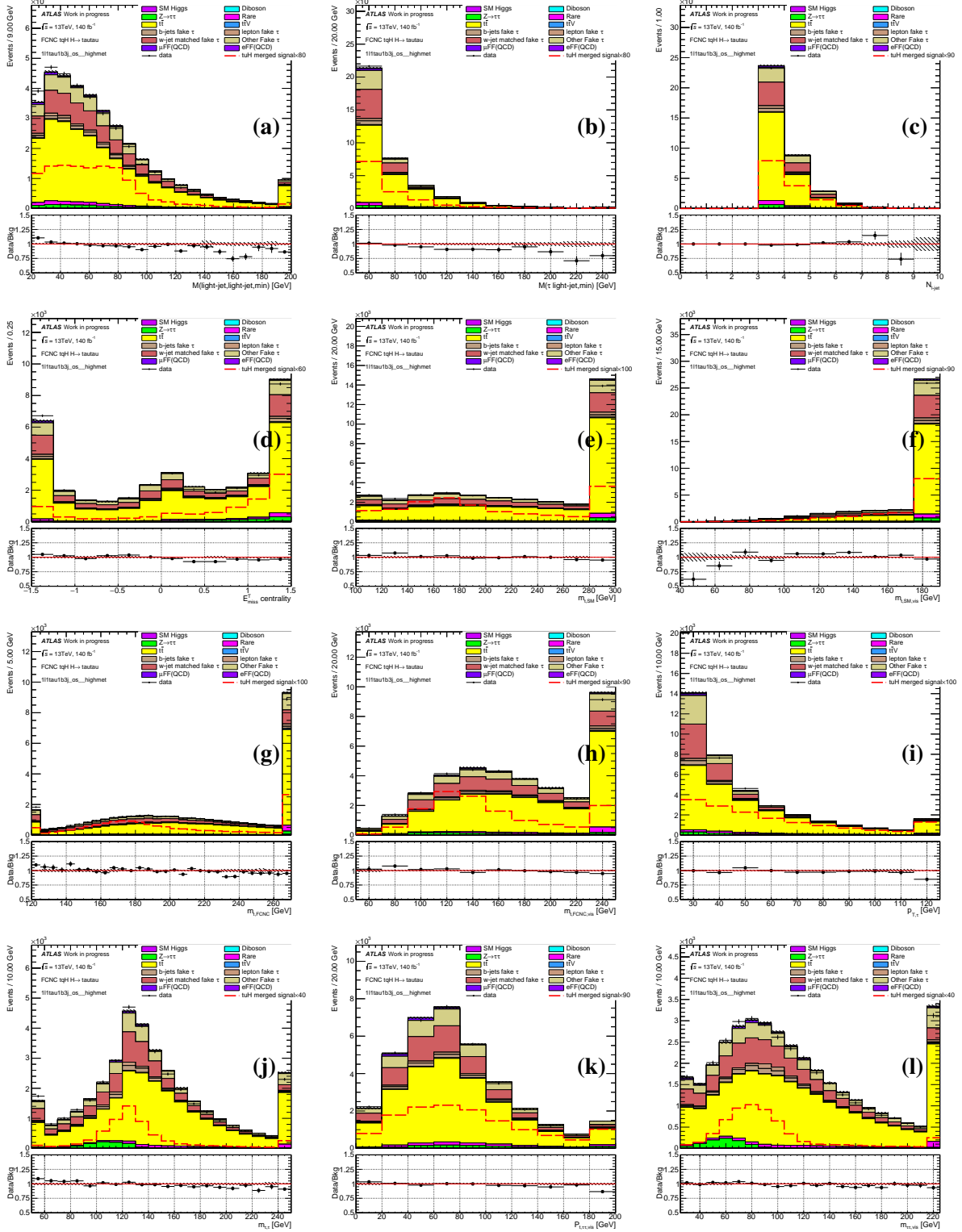


Figure 13: The variables distributions for the background and merged tuH signal in the TTH $\tau_{\text{lep}} \tau_{\text{had}}$

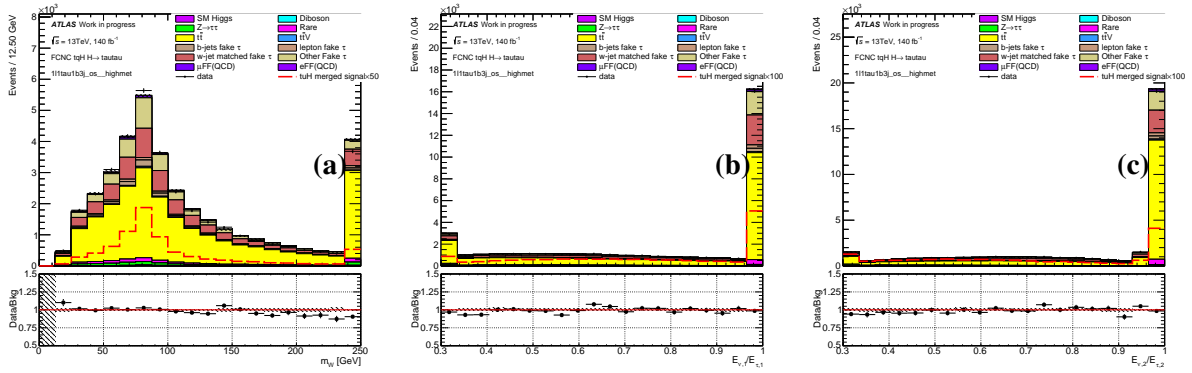


Figure 14: The variables distributions for the background and merged tuH signal in the TTH $\tau_{\text{lep}}\tau_{\text{had}}$

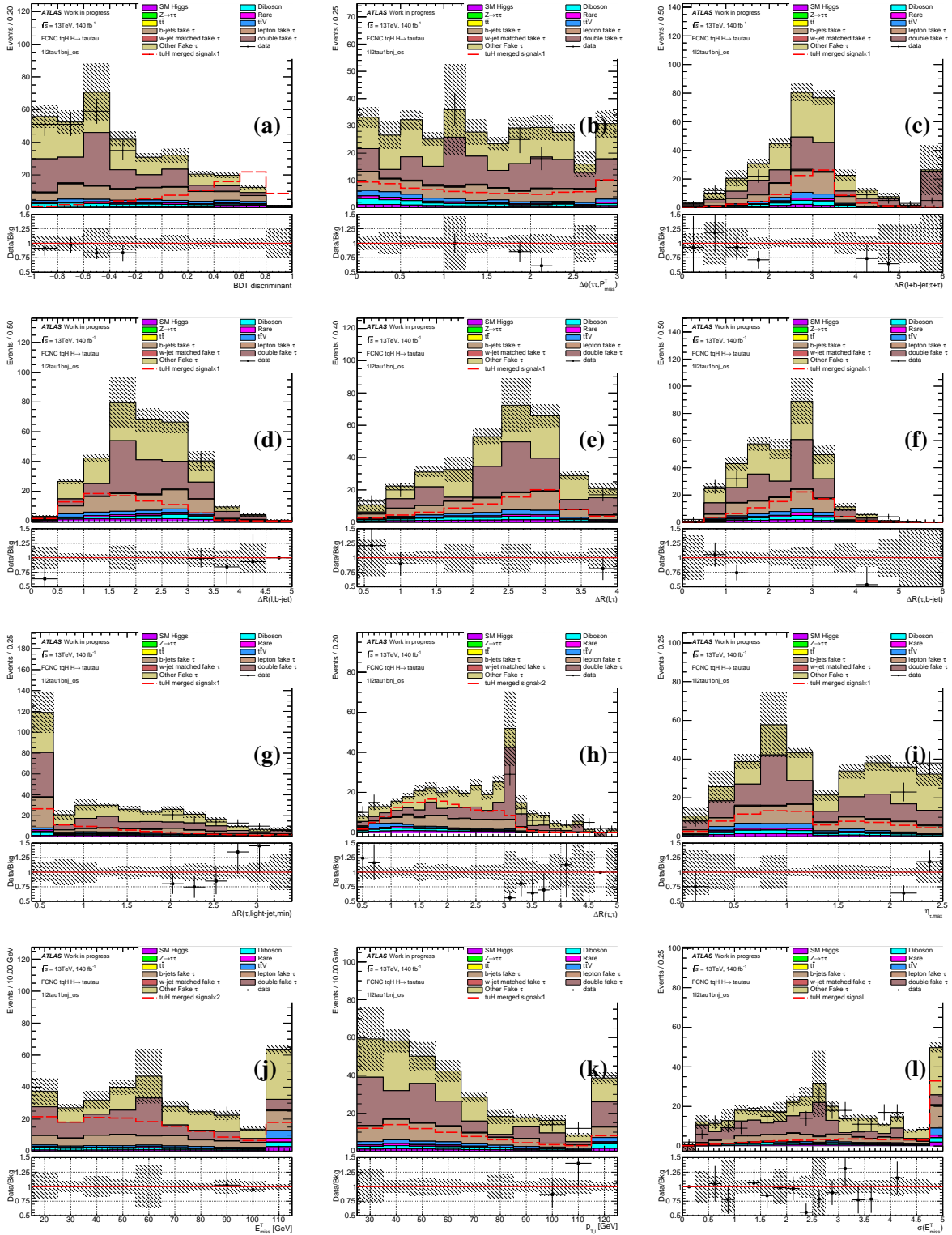
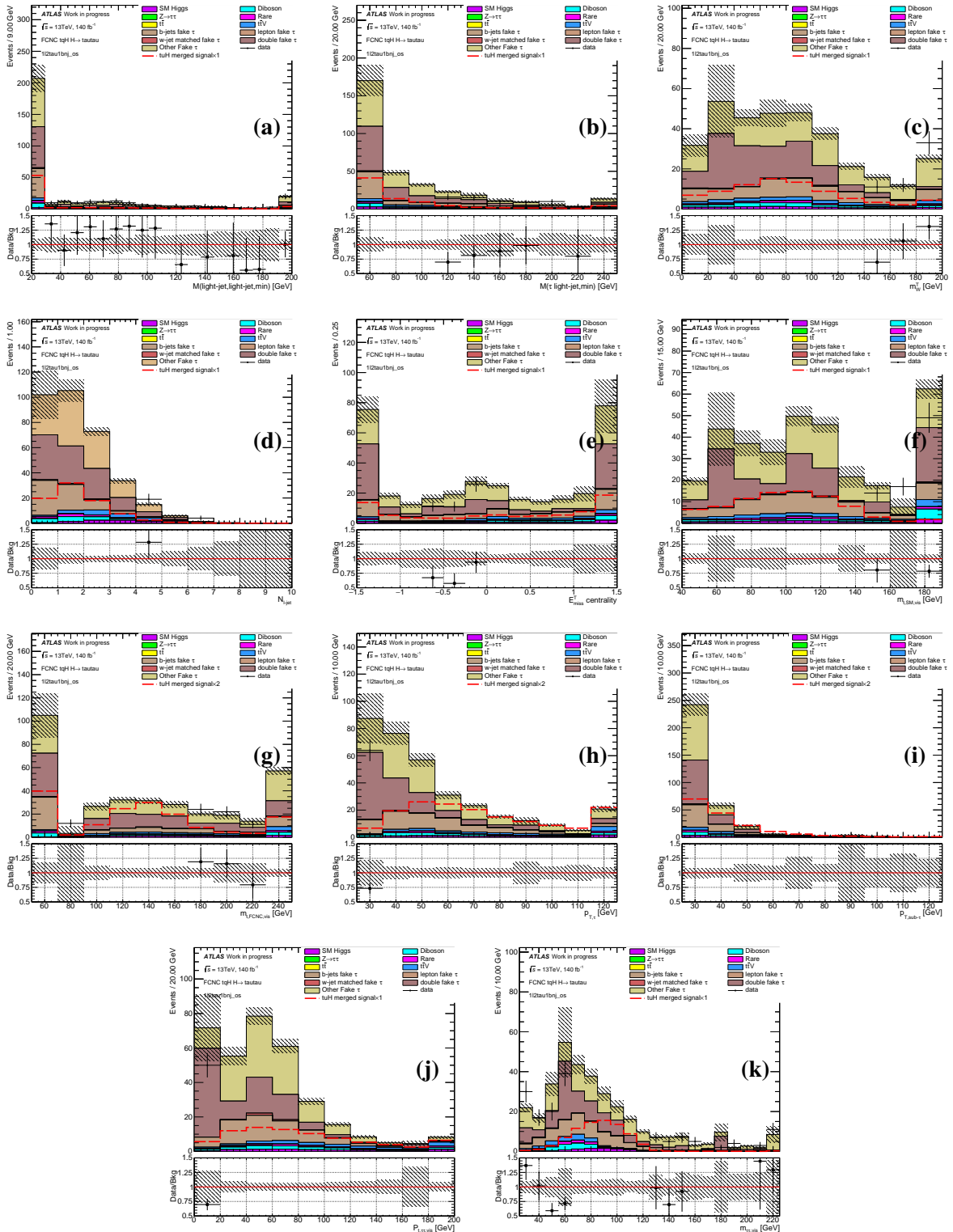


Figure 15: The variables distributions for the background and merged tuH signal in the $l\tau_{\text{had}}\tau_{\text{had}}$

Figure 16: The variables distributions for the background and merged tuH signal in the $l\tau_{\text{had}}\tau_{\text{had}}$

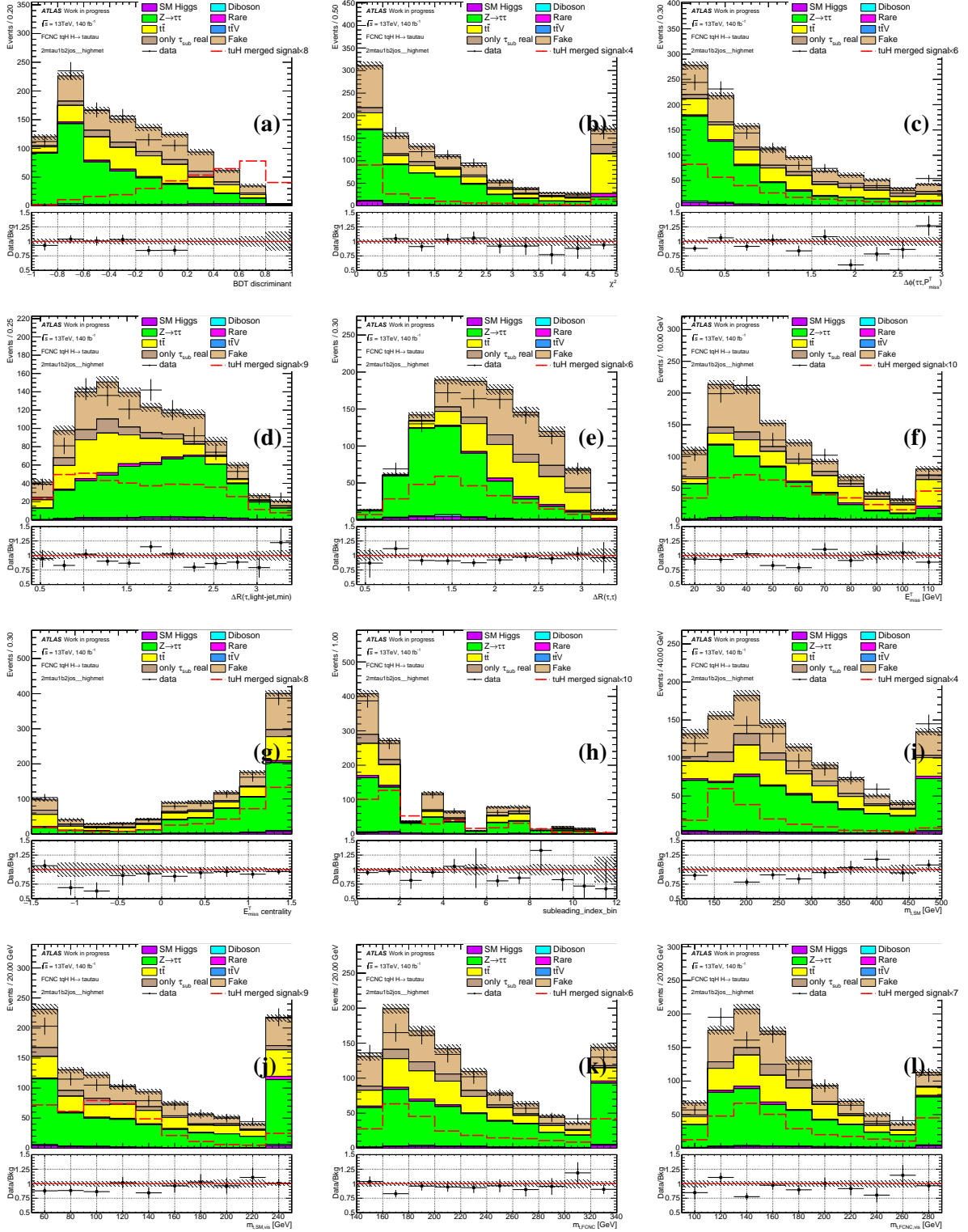


Figure 17: The variables distributions for the background and merged tuH signal in the STH $\tau_{\text{had}}\tau_{\text{had}}$

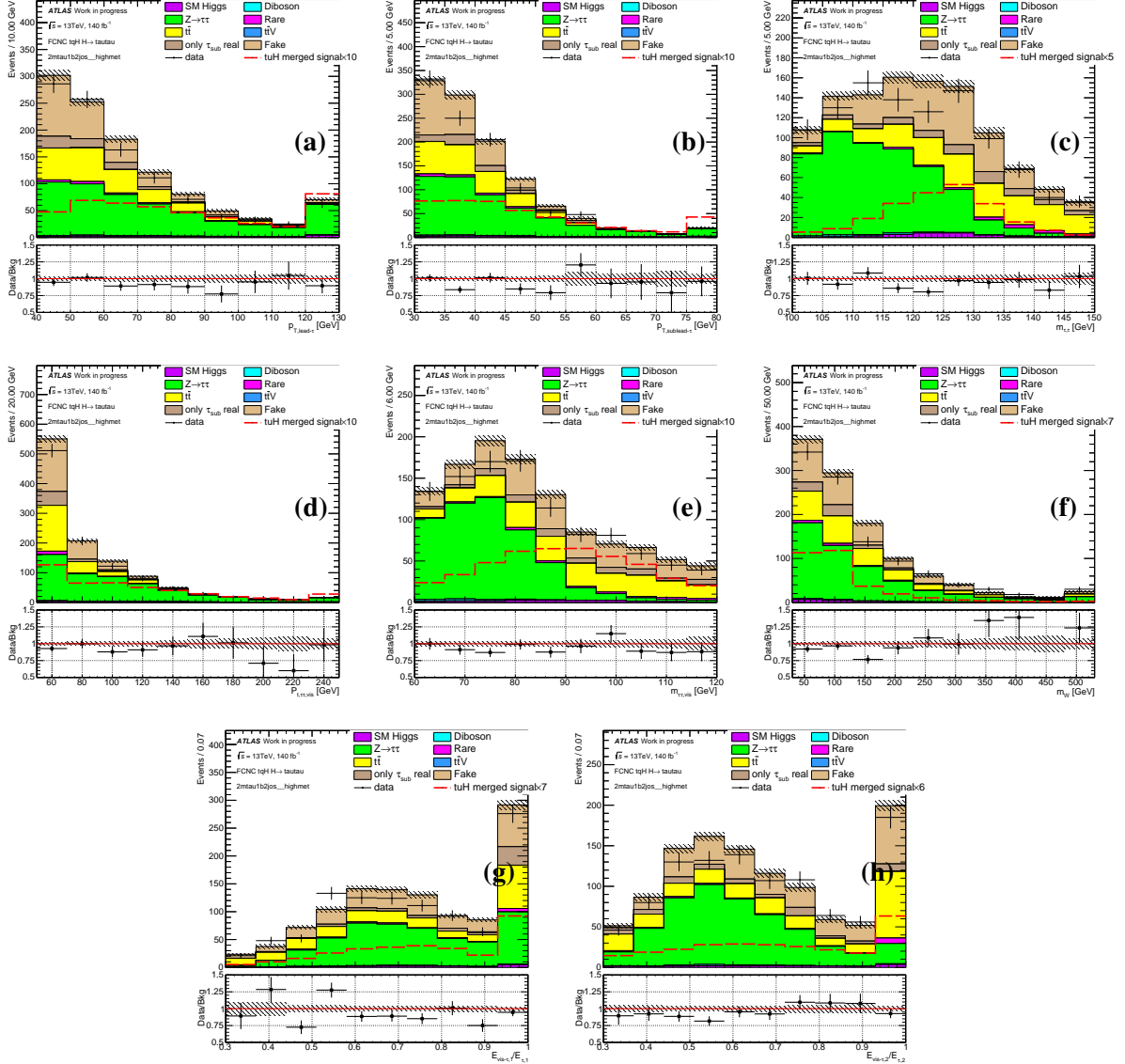


Figure 18: The variables distributions for the background and merged tuH signal in the STH $\tau_{\text{had}}\tau_{\text{had}}$

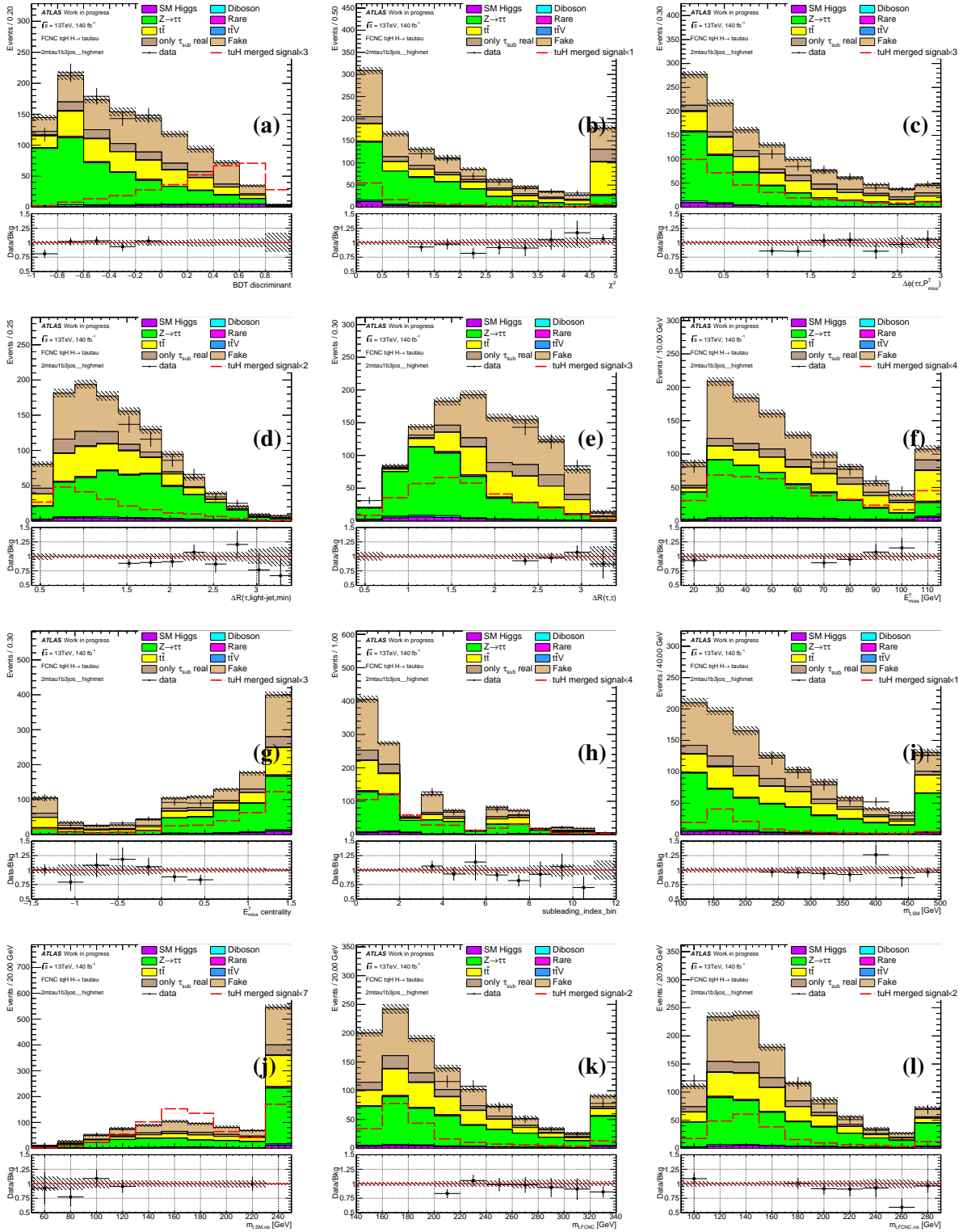


Figure 19: The variables distributions for the background and merged tuH signal in the TTH $\tau_{\text{had}}\tau_{\text{had}}$

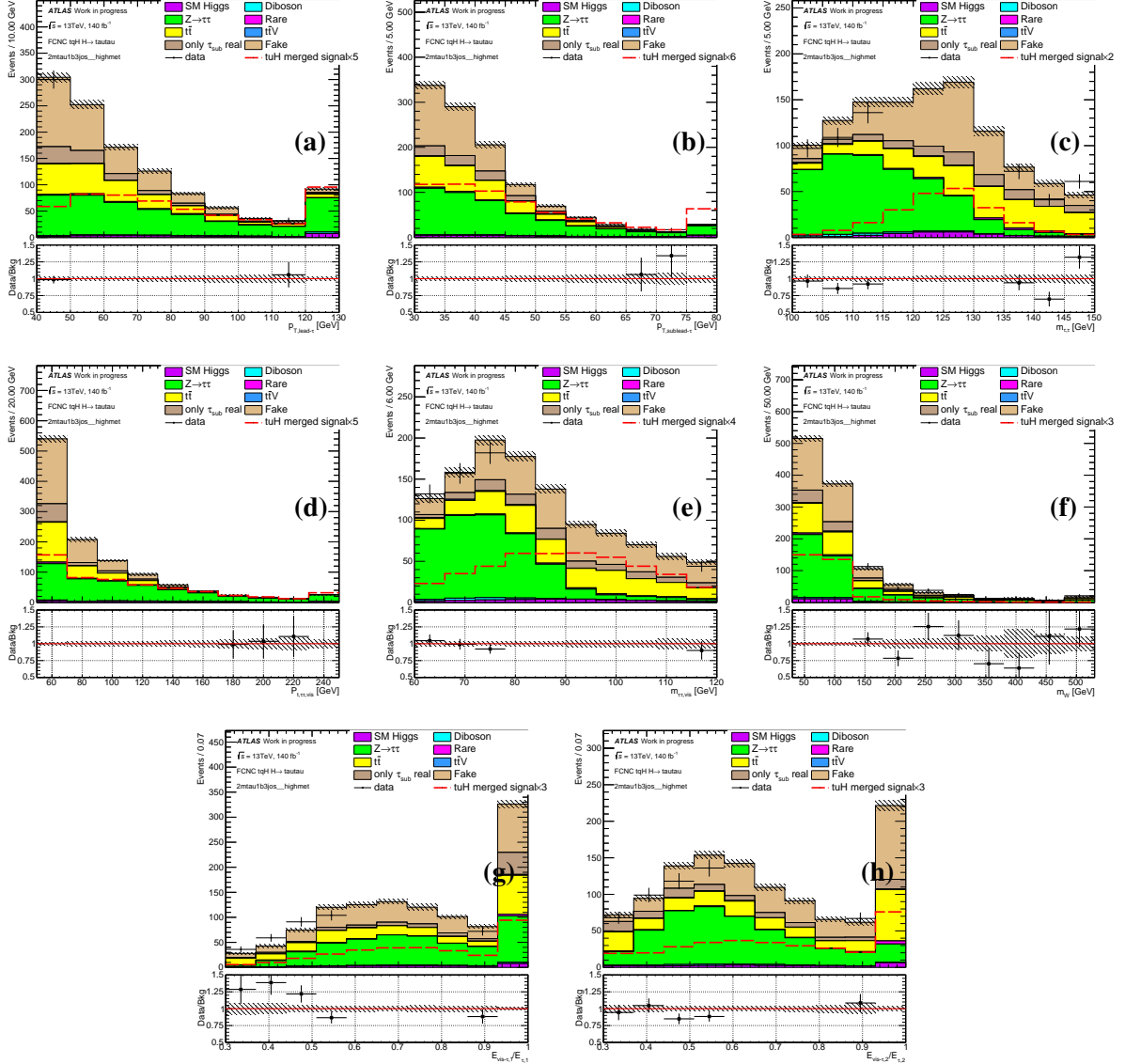


Figure 20: The variables distributions for the background and merged tuH signal in the TTH $\tau_{\text{had}} \tau_{\text{had}}$

518 9 Background estimation

519 The background events with real tau leptons are represented by Monte Carlo (MC) samples. These include
 520 $t\bar{t}$, $t\bar{t} + H/V$ and single top events with real taus, and $Z \rightarrow \tau\tau + \text{jets}$.

521 The $Z \rightarrow ee, \mu\mu$ processes are included for lepton faking tau background. The lepton faking taus are
 522 dominated by electrons which is studied by the tau working group. The e-veto BDT cut is used to reduce
 523 this kind of background as mentioned in the Section 6.4. The corresponding scale factors are applied
 524 separately to true electrons and true taus with dedicated uncertainties [56].

525 The fake background with one or more taus faked by jets consists of the top fake (with at least one fake
 526 tau from jets in the top events), QCD multijet, $W + \text{jets}$ and diboson events. Where the $t\bar{t}$ is dominant as
 527 shown in Figure 21.

528 9.1 Fake tau estimation in leptonic channels

529 Due to the large yield in the leptonic channels, tighter tau selection is applied, which limits the use of
 530 control regions with loosened tau identifications. the QCD background is much smaller than Monte Carlo
 531 events, so the MC events are used to model the fake taus. The fake taus are calibrated using Data-Driven
 532 (DD) Scale Factors (SF) derived by comparing the normalization of fake-tau events in MC to data in the
 533 control regions. This SF is then applied to correct the normalization of tau fakes in the MC yields. The
 534 excess of the events over these MC background is then from the multi-jets (QCD) faking background.

535 Top fake is the largest fake background in the total fake in the leptonic channels, which contributes around
 536 70% to 99% in different regions. Within the top fake events, fake taus can come from different origins,
 537 i.e., from jets (heavy/light flavor quark or gluon initiated) or leptons (electron or muon). The tau fake
 538 origins are checked with the top MC. Dedicated top pair production control regions are define for:

- 539 • W-jet faking tau: exactly 1 lepton, exactly 1 tau candidate, at least 4 jets with exactly 2 b-tagged.
 540 Tau candidate and lepton have the same charge, separated into $1l1tau2b2jSS$, $1l1tau2b2jSS$,
 541 $1l1tau2b2jSS$, $1l1tau2b2jSS$.
- 542 • B-jet faking tau: 2 leptons with different flavors or away from Z pole ($M_{ll} > 100\text{GeV}$ or $M_{ll} <$
 543 80GeV), exactly 1 tau candidate, exactly 1 b-tagged jet, later refered as $2l1tau1bnj$.
- 544 • Radiation faking tau: 2 leptons with different flavors or away from Z pole, exactly 1 tau candidate,
 545 at least two jets with exactly 2 b-tagged jets, later referred as $2l1tau2bnj$.

546 As shown in the Figure 21, most of the fake taus come from quark initiated jets, but the flavor distributions
 547 in OS are similar to those in SS. The data is generally over-estimated in the OS regions while it is opposite
 548 in the SS region. If the fake taus are corrected by the same scale factors, this mismodelling will never
 549 get solved. This asymmetry of the SS and OS fake taus can be interpreted by the mis-modelling of the
 550 fake tau charges. Since the fake taus mainly come from light-flavored jets as shown in Figure 22, the
 551 mis-modelling is related to the charge carried by the jets. In conclusion, the mis-modelling is originated
 552 from the charge correlation between the jet which is faking a tau and the lepton. So the parent of the jet
 553 is believed to be charge correlated with the lepton. Considering the main background is $\bar{t}t$ process. The
 554 only suspect is the hadronic W boson. In order to find the contribution of w-jet faking taus (τ_W). the truth
 555 information is used to match between the w-jet and the fake tau with $\Delta R < 0.4$. As shown in the Figure
 556 22, there is a considerable amount of τ_W 's in both SS and OS regions. There are four kinds of fake taus
 557 that need to be calibrated: Type1) τ_W 's with the opposite charge to the lepton; Type2) τ_W 's with the same
 558 charge as the lepton; Type 3) the fake taus from b-jets; Type4) the fake taus from other origins(mainly
 559 radiations). The following control regions are used to calibrate the four types.

- 560 • $2l1tau1bnj$: 2 leptons with different flavors or away from Z pole, exactly 1 tau candidate, exactly
 561 1 b-tagged jets.
- 562 • $2l1tau2bnj$: 2 leptons with different flavors or away from Z pole, exactly 1 tau candidate, exactly
 563 2 b-tagged jets.
- 564 • $1l1tau2b2jSS$: Exactly 1 lepton, exactly 1 tau candidate, exactly 4 jets with exactly 2 b-tagged.
 565 Tau candidate and lepton have the same charge.
- 566 • $1l1tau2b2jOS$: Exactly 1 lepton, exactly 1 tau candidate, exactly 4 jets with exactly 2 b-tagged.
 567 Tau candidate and lepton have the opposite charge.
- 568 • $1l1tau2b3jSS$: Exactly 1 lepton, exactly 1 tau candidate, at least 5 jets with exactly 2 b-tagged.
 569 Tau candidate and lepton have the same charge.
- 570 • $1l1tau2b3jOS$: Exactly 1 lepton, exactly 1 tau candidate, at least 5 jets with exactly 2 b-tagged.
 571 Tau candidate and lepton have the opposite charge.

572 In the control regions with single lepton, $E_T^{\text{miss}} > 20\text{GeV}$ and at least 2 light jets are required to ensure
 573 that QCD contribution is negligible.

574 Where di-lep regions ($2l1tau1b$ and $2l1tau2b$) are used to calibrate the Type3 and Type4 fake taus. These
 575 regions are dominated by the bjet and the radiation jet faking taus. $1l1tau2b2jOS$ and $1l1tau2b3jOS$
 576 are used to calibrate Type1 fake taus. Compared to the signal region, this region has an additional b-jet.
 577 So the $\bar{t}t$ background is enhanced in this region and signal is depleted. Similarly for the Type2, regions
 578 $1l1tau2b2jSS$ and $1l1tau2b3jSS$ are chosen. The components of these regions are shown in Figure
 579 23. A simultaneous fit is made to derive the scale factors for the fake taus. There are four parameters

Table 6: The scale factors for 1 prong fake taus in different p_T bins derived from the fit.

	$25 - 35 \text{ GeV}$	$35 - 45 \text{ GeV}$	$45\text{GeV}-$
$\tau_{b \text{ fake}}$	0.61 ± 0.10	0.83 ± 0.10	0.84 ± 0.07
τ_{other}	1.19 ± 0.02	1.00 ± 0.04	0.77 ± 0.03
$\tau_W \text{ os}$	0.67 ± 0.01	0.62 ± 0.02	0.37 ± 0.02
$\tau_W \text{ ss}$	0.82 ± 0.05	0.50 ± 0.07	0.74 ± 0.07

Table 7: The scale factors for 3 prong fake taus in different p_T bins derived from the fit.

	$25 - 35 \text{ GeV}$	$35 - 45 \text{ GeV}$	$45\text{GeV}-$
$\tau_{b \text{ fake}}$	1.04 ± 0.14	1.33 ± 0.13	1.22 ± 0.11
τ_{other}	1.24 ± 0.07	0.70 ± 0.08	0.73 ± 0.08
$\tau_W \text{ os}$	0.92 ± 0.03	1.07 ± 0.04	0.21 ± 0.05
$\tau_W \text{ ss}$	1.00 ± 0.10	1.07 ± 0.09	0.73 ± 0.08

needed to be decided (the scale factors for the 4 types). But considering the p_T and number of tracks dependence of the tau reconstruction, the scale factors are derived in 3 p_T slices (25-35, 35-45, 45-)GeV and 1/3 prong taus. So there are 24 parameters to be decided. The results are shown in table 6 and 7. Where the errors are statistical only. The post-fit plots are shown in Figure 24. Then the scale factors are applied to the corresponding single b-jet regions. In $l\tau_{had}\tau_{had}$ channel, both taus can be fake, so the calibration is done to them separately, following the same procedure as $\tau_{lep}\tau_{had}$ channels using the lepton and fake tau charges, then the scale factors are multiplied together. The nominal value of the scale factors will vary along with other uncertainties from combined preformance (CP) recommendations and theory uncertainties in the final fit.

9.2 QCD fake background in $\tau_{lep}\tau_{had}$ and $l\tau_{had}$ regions

After the fake tau calibration, the fake contribution from QCD with both lepton and tau faked is estimated using ABCD method. For each $\tau_{lep}\tau_{had}$ and $l\tau_{had}$ signal regions, 4 blocks are defined as follows:

- A: $E_T^{miss} < 20\text{GeV}$, PLV not tight
- B: $E_T^{miss} < 20\text{GeV}$, PLV tight
- C: $E_T^{miss} > 20\text{GeV}$, PLV not tight
- D: $E_T^{miss} > 20\text{GeV}$, PLV tight

Table 8: The QCD transfer factor derived from different low E_T^{miss} control regions

	Electron	Muon
1 τ_{hadj} ss	0.76 ± 0.19	0.57 ± 0.11
STH $\tau_{lep}\tau_{had}$ os	0.60 ± 0.47	1.39 ± 0.35
1 $\tau_{had}2j$ ss	0.74 ± 0.42	0.54 ± 0.23
TTH $\tau_{lep}\tau_{had}$ os	1.12 ± 0.90	1.18 ± 0.52
Combined	0.75 ± 0.18	0.64 ± 0.25

Table 9: The QCD transfer factor derived from low BDT regions as closure test.

	Electron	Muon
lowBDT 1 τ_{hadj} ss	0.48 ± 0.23	0.38 ± 0.19
lowBDT STH $\tau_{lep}\tau_{had}$ os	1.71 ± 1.52	0.23 ± 0.92
lowBDT 1 $\tau_{had}2j$ ss	-0.25 ± 1.68	-0.00 ± 0.59
lowBDT TTH $\tau_{lep}\tau_{had}$ os	0.56 ± 1.28	4.00 ± 2.73
Combined	0.50 ± 0.30	0.36 ± 0.32

- 596 The transfer factors are measured in each signal region as $r = \frac{N_B}{N_A}$. Where N_A and N_B are the yields
 597 calculated by data-MC where MC includes real lepton background with real taus or calibrated fake taus.
 598 The results are shown in Table 8. The uncertainties in the table for each region contains statistical
 599 uncertainties during the calculation and the potential signal contribution ($BR = 0.2\%$). In principle for
 600 the QCD estimation, the transfer factor should not depend on the number of jets and charge. So all
 601 of the 4 measurements are taken into consideration to derive a universal transfer factor. The central
 602 value and statistical uncertainty of the transfer factor are derived using likelihood method separately for
 603 electron and muons. The systematics variation is taken by calculating the second moment of the four
 604 measurements (The power is $1/\sigma^2$). The combined result is shown as the last line in the table with both
 605 statistics and systematics considered, where the statistical uncertainty for electron and muon are 0.13
 606 and 0.07 respectively, which indicates that the systematic uncertainties are comparable with the statistical
 607 uncertainties, meaning that there is no big deviation among the 4 measurements.
 608 Finally the QCD contribution in D is then estimated as rD . The data-MC comparison after the fake tau
 609 and fake lepton estimation is show in Figure 25.
 610 A closure test is make for the background estimations in the low BDT region (BDT score < -0.6) The
 611 transfer factor derived in the low BDT region is shown in the Table 9. The leading lepton p_T distribution
 612 in the low BDT is shown in Figure 26.

613 9.3 Fake tau estimate in hadronic channels

614 In the hadronic channels, the QCD also contributes to the fake tau background which doesn't have MC
 615 samples. So the QCD and part of MC fake background are estimated together using anti tau ID control
 616 regions.

617 The $\tau_{\text{had}} p_T$ spectra in the $\tau_{\text{had}} \tau_{\text{had}}$ SS and OS are shown in Figure 27, where the data is far beyond the
 618 background prediction, which only contains real tau background. A Fake Factor Method developed by
 619 $H \rightarrow \tau\tau$ group [53] is adopted and customized for this analysis.

- 620 • Fake-CR: 2 opposite charged τ_{had} with leading one passing RNN medium, subleading one failing
 621 RNN medium, other requirements are the same as SR.

622 Since the sub-leading tau ID is reversed, the Fake-CR have most of events with fake sub-leading tau.
 623 However there are events with leading taus fake but sub-leading taus real in the SR where both taus are
 624 equally medium. These events can not be modelled by the events in Fake-CR. Fortunately the contribution
 625 of these events is minor compared to the other fake background. So they can be modelled by MC with the
 626 shape uncertainty neglected and the normalisation uncertainty can be applied according to fake studies in
 627 the leptonic channels (50% to be conservative).

628 Then the events with fake sub-leading tau will be represented by the templates of fake taus in the Fake-CR
 629 with proper fake factors. The templates are acquired by subtracting all MC background contributions with
 630 real subleading taus from data.

631 The Fake-factors (FF) were computed in the W+jets control region (1 lepton + 1 tau, no b-jet) by the
 632 $H \rightarrow \tau\tau$ group [53] as listed in Table 10. They are computed in two regions with different tau ID
 633 requirement. The FFs are the ratio of the Data–MC_{real tau} yields passing medium tau ID to which failing
 634 the medium tau ID. The FFs are calculated in 12 bins ($\eta, p_T, N_{\text{track}} : 2 \times 3 \times 2 = 12$).

635 The uncertainties of this method consists of three parts:

- 636 1. The statistical uncertainties during the FF derivation, one for each FF, 12 in total.
- 637 2. The FF is rederived in the SS CR (2 taus with same charge, at least 3 jets with exactly 1 b-tagged)
 638 to account for the limitations of the parametrization of the fake-factors as shown in Figure 28. The
 639 fake factor are presented in Table 11.
- 640 3. The FF is rederived in the OS CR (2 taus with opposite charge, at least 3 jets with exactly 1 b-tagged)
 641 with the events failing the cut chain in Table 23 and 24 to account for the different contribution from
 642 each origin of the fake taus as shown in Figure 28. The fake factor are presented in Table 12.

Table 10: FF derived by the $H \rightarrow \tau\tau$ group.

		30 – 40 GeV	40 – 60 GeV	60 GeV-
1p	$ \eta \leq 1.37$	0.297 ± 0.020	0.258 ± 0.021	0.192 ± 0.027
	$ \eta \geq 1.52$	0.242 ± 0.021	0.166 ± 0.023	0.131 ± 0.030
3p	$ \eta \leq 1.37$	0.131 ± 0.018	0.104 ± 0.017	0.158 ± 0.032
	$ \eta \geq 1.52$	0.074 ± 0.023	0.086 ± 0.020	0.057 ± 0.030

Table 11: FF derived in SS CR.

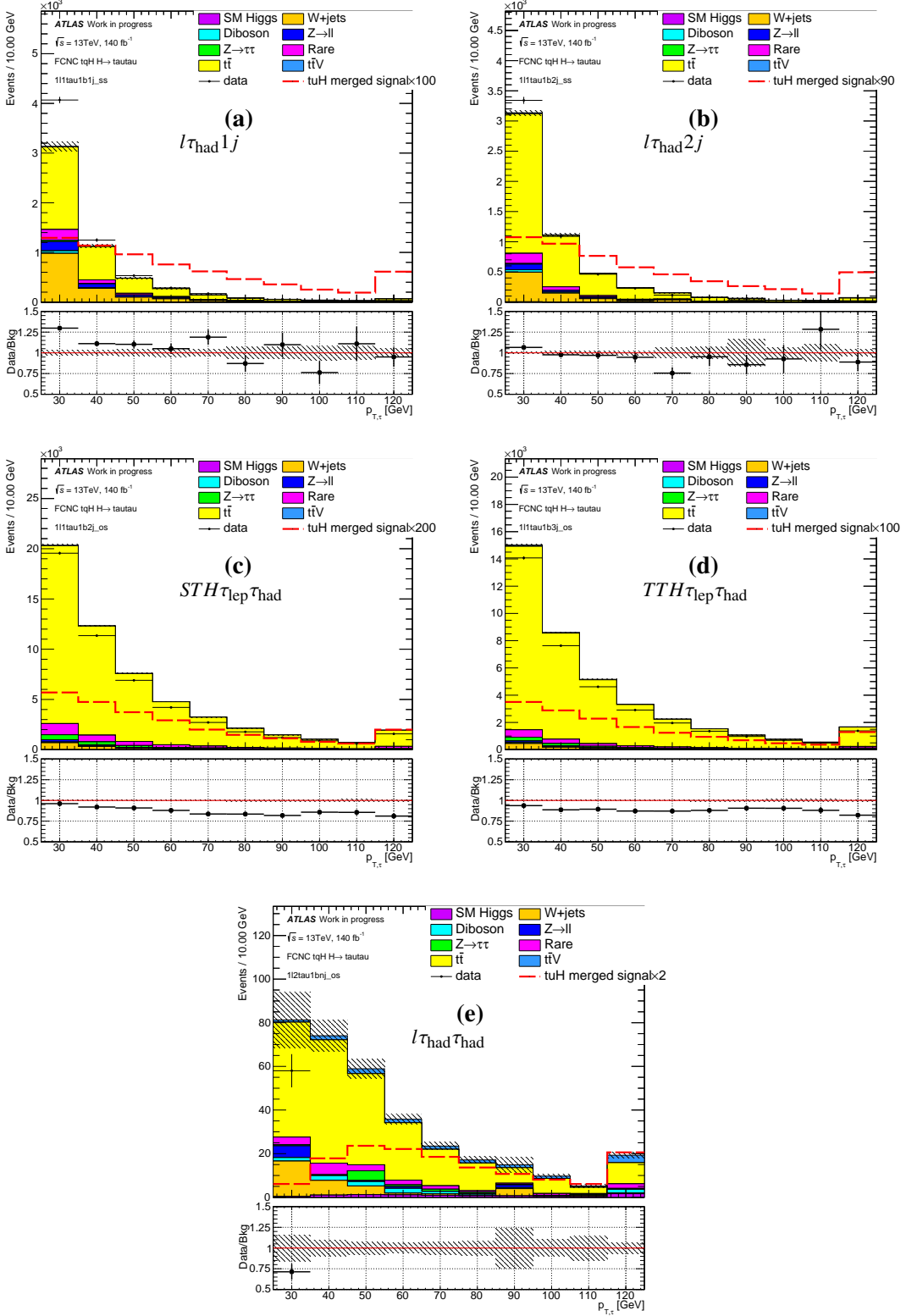
		30 – 40 GeV	40 – 60 GeV	60 GeV-
1p	$ \eta \leq 1.37$	0.25 ± 0.02	0.25 ± 0.04	-0.09 ± 0.04
	$ \eta \geq 1.52$	0.20 ± 0.03	0.15 ± 0.04	0.31 ± 0.28
3p	$ \eta \leq 1.37$	0.11 ± 0.02	0.12 ± 0.03	-0.07 ± 0.04
	$ \eta \geq 1.52$	0.09 ± 0.03	0.05 ± 0.03	-0.02 ± 0.01

Table 12: FF derived in OS CR.

		30 – 40 GeV	40 – 60 GeV	60 GeV-
1p	$ \eta \leq 1.37$	0.29 ± 0.03	0.17 ± 0.04	-0.10 ± 0.14
	$ \eta \geq 1.52$	0.20 ± 0.03	0.19 ± 0.04	-0.06 ± 0.11
3p	$ \eta \leq 1.37$	0.11 ± 0.03	0.04 ± 0.03	-0.24 ± 0.12
	$ \eta \geq 1.52$	0.05 ± 0.03	0.02 ± 0.03	-0.14 ± 0.14

643 Due to the low statistics in the high p_T region, some fake factors are negative in SS CR or OS CR. Those
 644 FFs are treated as 0.

645 The tau p_T distribution after fake estimation is shown in Figure 29.

Figure 21: The distributions of τp_T in the signal regions.

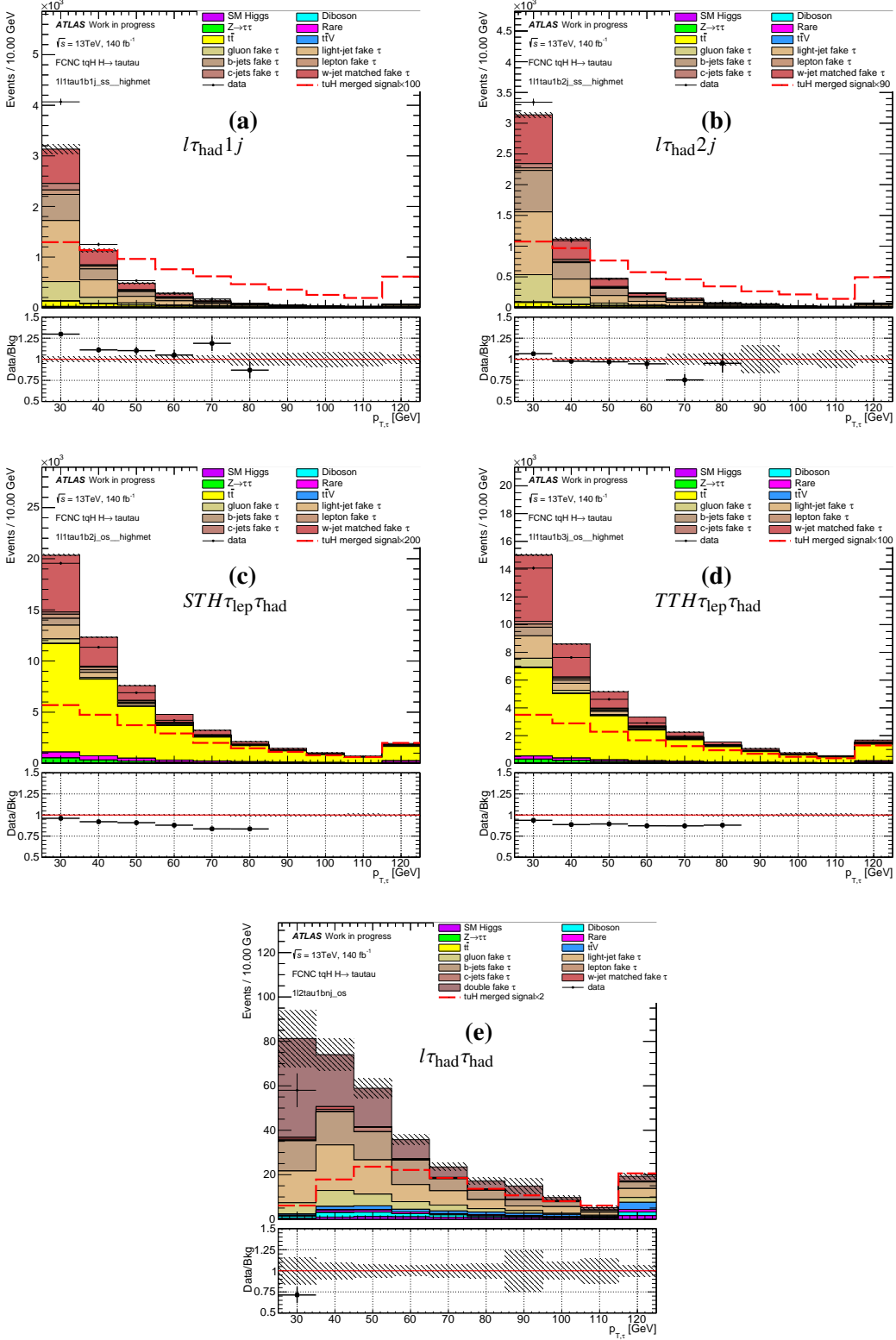


Figure 22: The distributions of τp_T in the signal regions with fake tau origin shown.

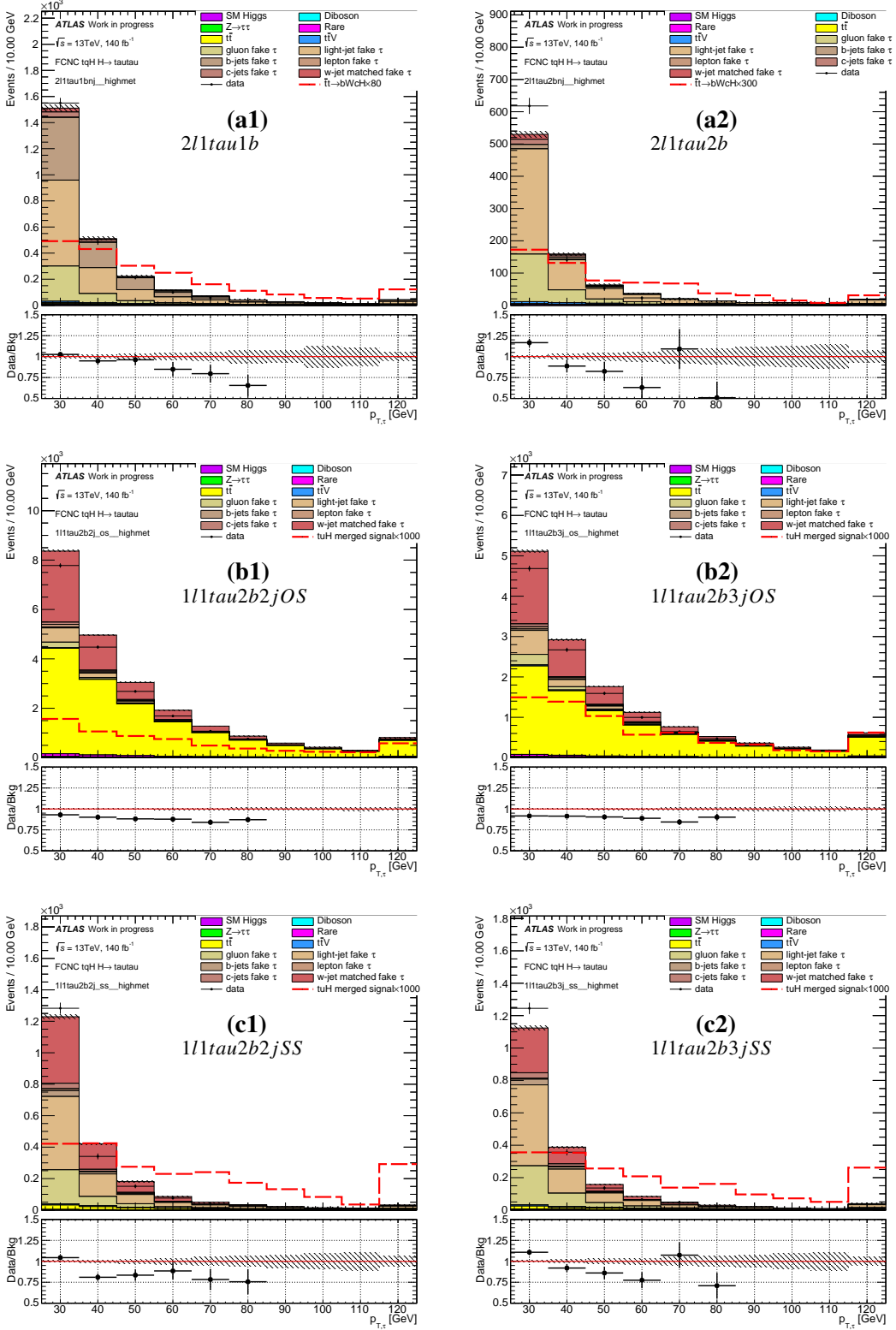
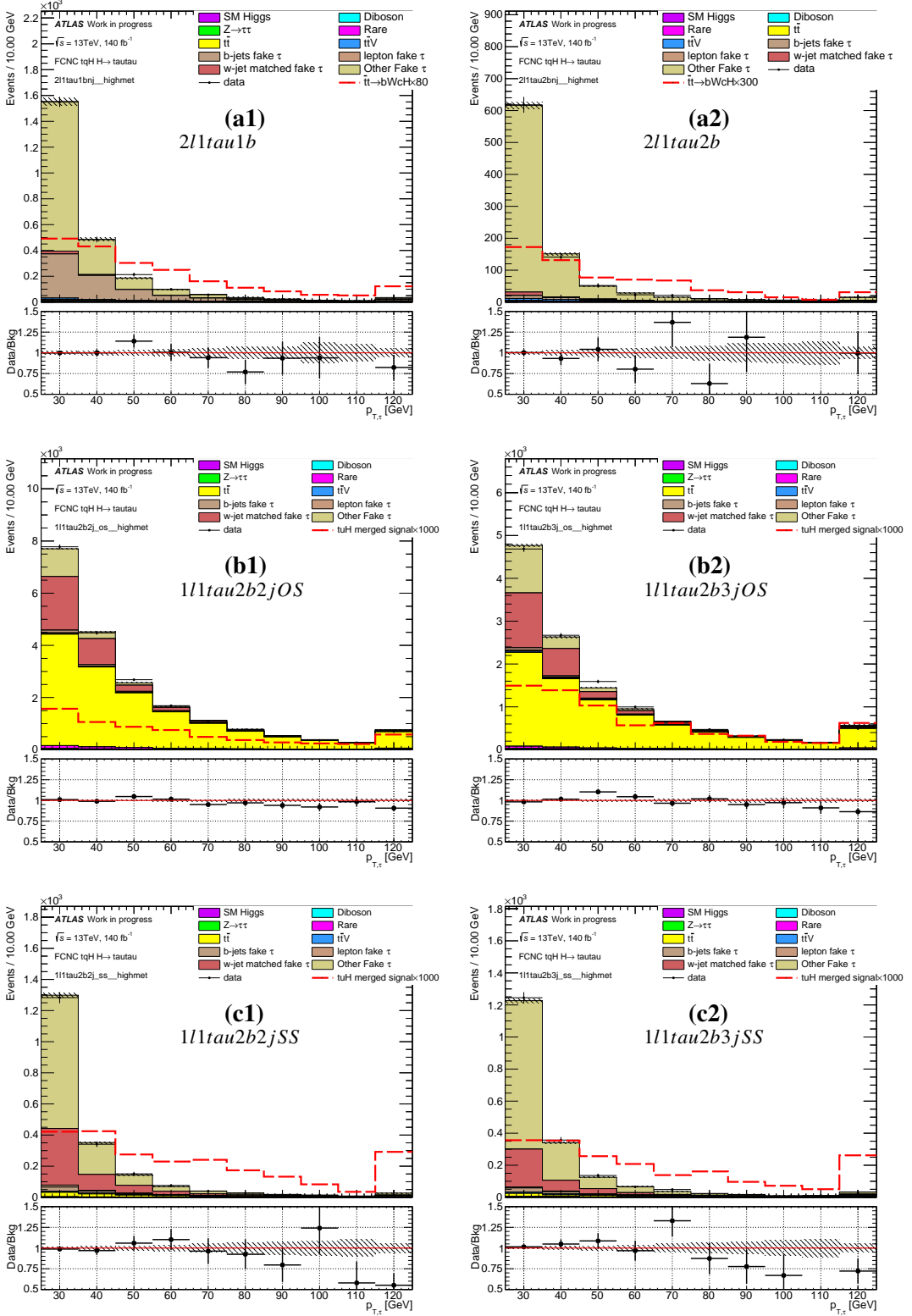


Figure 23: The distributions of τ p_T in the control regions used to calibrate the fake taus.

Figure 24: The post-fit distributions of τp_T in the control regions after the fake tau correction.

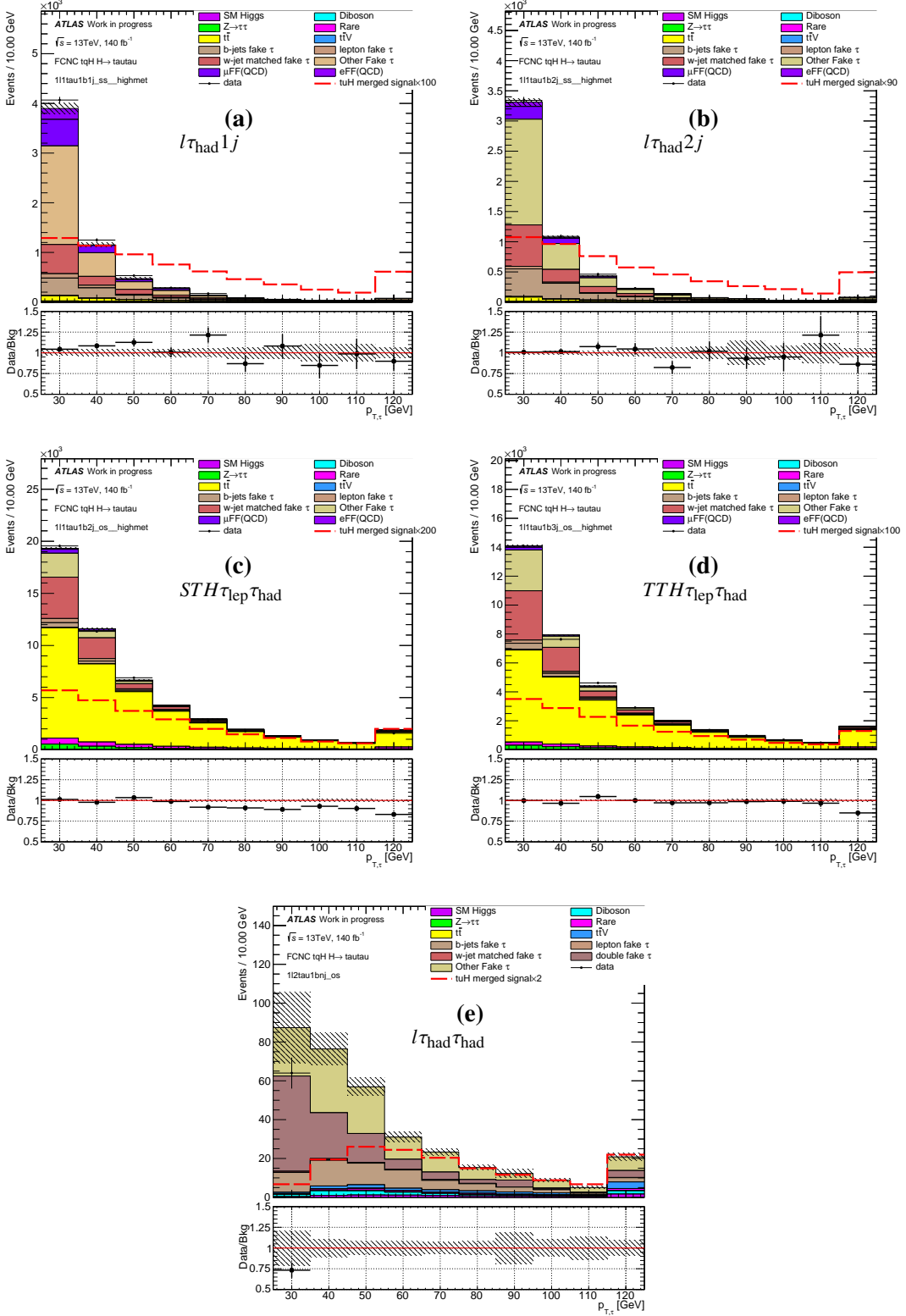


Figure 25: The data-MC comparison of τp_T in the signal regions after the fake tau correction and QCD estimation.

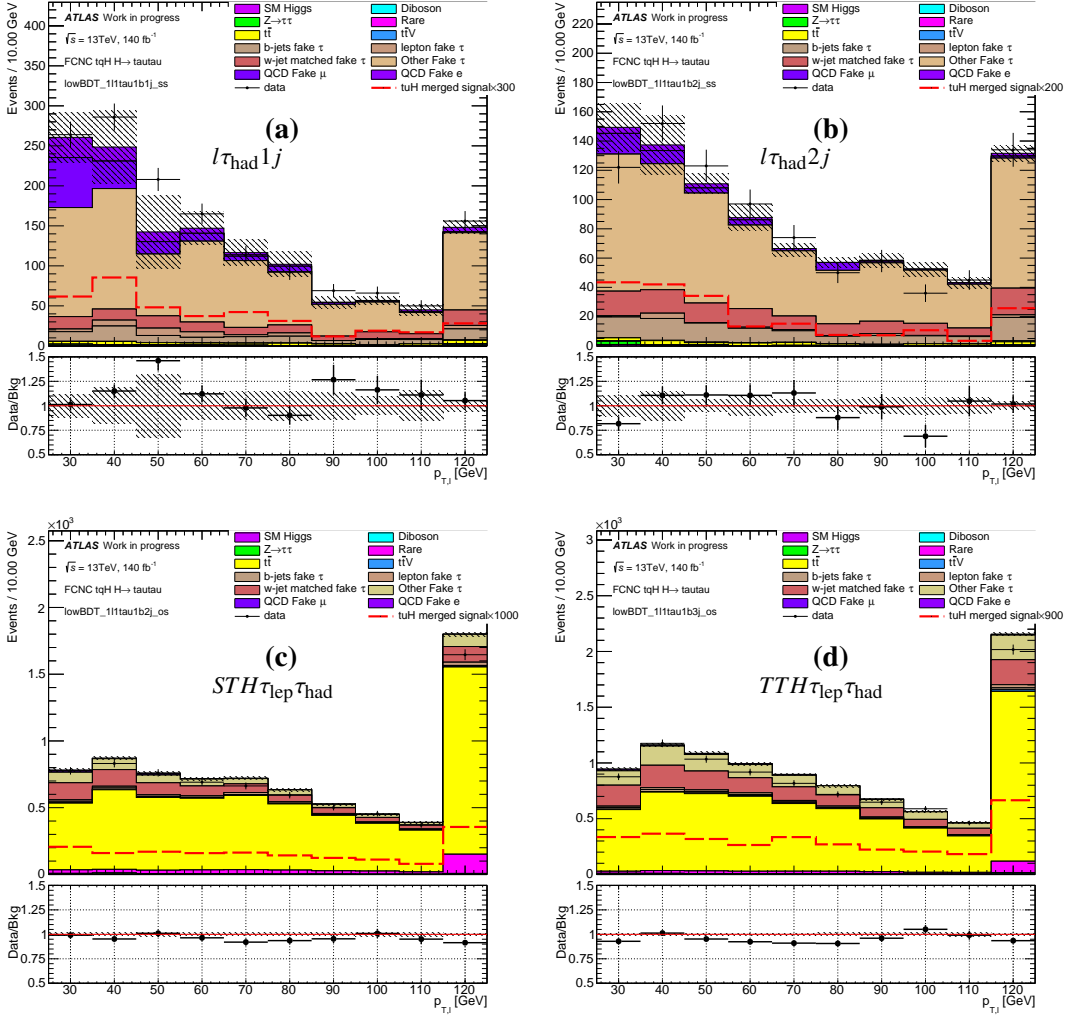


Figure 26: The data-MC comparison of lepton p_T in the low BDT score regions after the fake tau correction and QCD estimation.

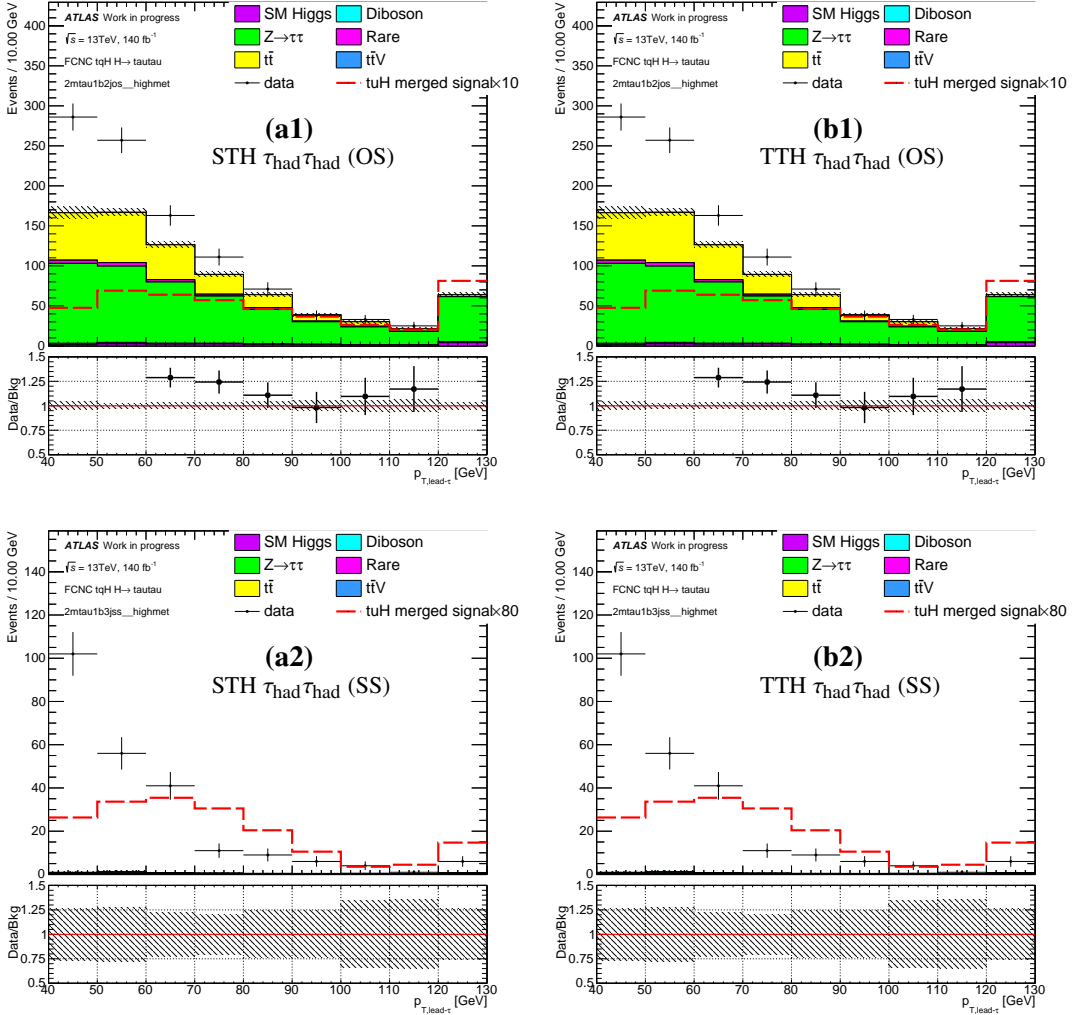


Figure 27: The distributions of leading τ p_T in the STH (a), and TTH (b) $\tau_{\text{had}}\tau_{\text{had}}$ SR (1) and SS CR (2) before the fake estimation. Data is more than the MC prediction because the fake tau backgrounds are not yet added.

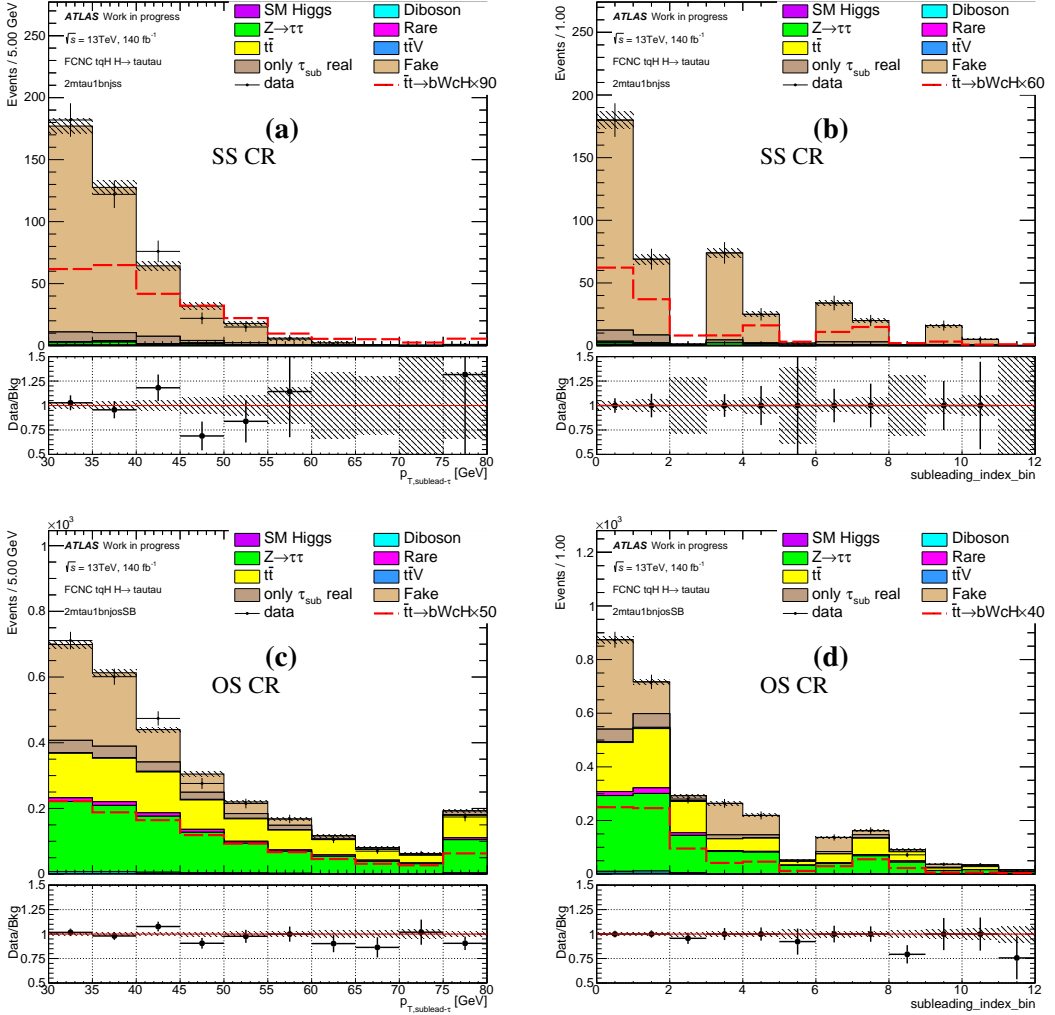


Figure 28: The distributions of sub-leading τp_T and sub-leading tau index (bin 1-6 are for 3 prong, 7-12 are for 1 prong; bin 1-3, 7-9 are for $|\eta| < 1.37$ with 3 p_T slices and the rest are for $|\eta| > 1.52$) in the SS CR and OS CR. The fake estimation of the index is perfect by definition but in some high p_T bins MC is higher than data where the estimation is treated as 0.

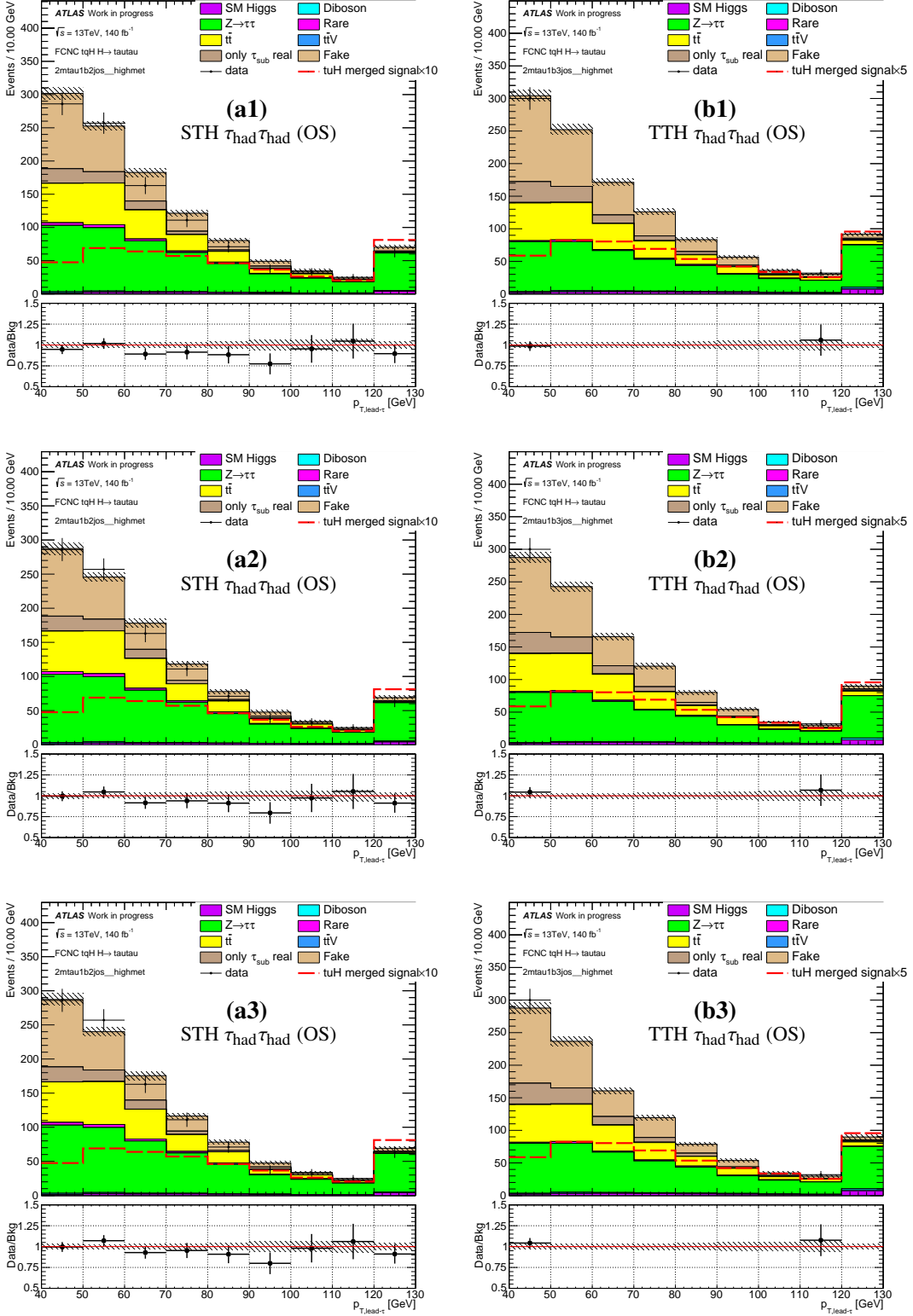


Figure 29: The distributions of τ p_{τ} in the STH $\tau_{\text{had}}\tau_{\text{had}}$ (SS)(a1-3), STH $\tau_{\text{had}}\tau_{\text{had}}$ (OS) (b1-3), using the nominal (1), SS CR derived (2), OS CR derived FFs.

646 10 MVA analysis

647 In this section, we investigate the sensitivity of probing signal using one of the Multi-Variate Analysis
 648 (MVA) methods, the Gradient Boosted Decision Trees (BDT) method [60, 61], with the TMVA software
 649 package. The BDT output score is in the range between -1 and 1. The most signal-like events have scores
 650 near 1 while the most background-like events have scores near -1.

651 The signal topology and kinematics are different across all the channels. To maximize the overall
 652 sensitivity, separated BDTG trainings are applied to each the signal region. A number of variables as
 653 the BDT inputs are used to train and test events in each signal region for maximal signal acceptance and
 654 background rejection. They are listed in Table 13 and Table 14. The most sensitive variables distributions
 655 are shown in Figure 30-32

656 The signal and background samples are randomly divided into two equal parts (denoted as even and odd
 657 parity events). The BDT is trained with one part, and tested on the other part. It is always ensured that
 658 the BDT derived from the training events is not applied to the same events, but only to the independent
 659 test ones. The sum of MC all background processes, corrected normalized, are used in the training and
 660 testing. With the `IgnoreNegWeightsInTraining` option, only MC events with positive MC weights
 661 are used in the traning. In The hadronic channels, due to the fake is modelled by the not medium control
 662 region, the data events in the not medium control region is also used in the training with a weight of 0.3
 663 to take the FFs into account. The comparison of BDT performances in test-odd and test-even samples is
 664 given in Figure 33-35.

665 The BDT parameters `NTrees` and `nCuts` are tuned based on the integration of the ROC S . The best choice
 666 for each channel depends on the number of variables used and the statistics. The optimisation factor is
 667 defined as $L = S_{\text{avg}} - xS_{\text{diff}}$, where S_{avg} is the average integration value of the two folds, indicating the
 668 separation power of the model, meaning the larger it is, the better. S_{diff} is the difference between the
 669 integration values of the two folds, indicating the instability of the models, meaning the smaller it is, the
 670 better. The factor x is chosen depending on how important the stability is regarded over the separation
 671 power, where there is no common standard. In this analysis $x = 1$ is chosen.==

672 The optimisation process uses a gradient method with a step of 5 for `nCuts` and 10 for `NTrees`. The
 673 optimisation stops when the smallest value of the optimisation factor L is found. The steps taken is listed
 674 in the App. ???. The final result is shown in Table 15.

675 The importance factors¹ of different variables used in the training is listed in Table 13 and 14. The two
 676 numbers in each block represent the importance factor of the two models trained from even and odd parts.
 677 The consistency of these factors implies that the training models are stable.

¹ The importance is evaluated as the total separation gain that this variable had in the decision trees (weighted by the number of events). It is normalized to all variables together, which have an importance of 1.

Table 13: The importance (in %) of each variables used in the BDTG training for leptonic channels, the two numbers in the each block are from the two training folds.

	$l\tau_{\text{hadj ss}}$	$\text{STH } \tau_{\text{lep}}\tau_{\text{had os}}$	$l\tau_{\text{had}}2j\text{ ss}$	$\text{TTH } \tau_{\text{lep}}\tau_{\text{had os}}$	$l\tau_{\text{had}}\tau_{\text{had os}}$
$p_{T,\tau}$	19.59 / 17.68	8.23 / 7.95	13.37 / 13.70	7.66 / 7.97	6.72 / 8.40
E_{miss}^T	7.83 / 9.26	6.91 / 6.34	4.64 / 3.58	7.59 / 7.32	5.87 / 7.05
$m_{\tau\tau,\text{vis}}$	7.00 / 7.01	8.68 / 9.00	2.32 / 3.75	9.19 / 9.36	13.23 / 11.76
$\Delta R(\tau, \text{light jet}, \text{min})$	15.88 / 15.37	7.20 / 7.40	9.76 / 10.27	6.88 / 6.37	7.16 / 8.36
$\Delta R(l, b \text{ jet})$	17.01 / 18.42	4.69 / 6.24	12.88 / 12.30	6.30 / 4.87	6.03 / 6.74
$\Delta R(l, \tau)$	14.56 / 11.39	7.93 / 8.17	7.06 / 7.33	7.89 / 7.71	2.92 / 2.47
$\Delta R(\tau, b \text{ jet})$	12.73 / 12.95	7.50 / 6.50	7.12 / 8.37	5.48 / 5.31	4.99 / 2.33
$p_{T,l}$	5.40 / 7.92	3.62 / 3.74	5.86 / 7.20	2.28 / 3.13	1.55 / 2.78
$\Delta\phi(\tau\tau, P_{\text{miss}}^T)$	/	6.55 / 5.28	4.02 / 3.57	5.76 / 5.08	/
$E_{\text{miss}}^T \text{centrality}$	/	6.62 / 6.02	4.03 / 4.97	5.14 / 5.72	/
$m_{\tau,\tau}$	/	4.20 / 4.01	1.90 / 2.40	2.94 / 3.64	/
$E_{\nu,1}/E_{\tau,1}$	/	9.75 / 10.16	9.55 / 9.12	8.51 / 9.81	/
$E_{\nu,2}/E_{\tau,2}$	/	8.38 / 9.14	8.02 / 9.85	8.41 / 8.39	/
$m_{t,SM}$	/	5.56 / 5.64	3.37 / 0.79	4.50 / 4.60	/
$M(\text{light jet}, \text{light jet}, \text{min})$	/	4.19 / 4.39	6.11 / 2.80	5.65 / 4.86	/
m_W	/	/	/	3.28 / 3.27	/
χ^2	/	/	/	2.55 / 2.58	/
$\Delta R(\tau, \tau)$	/	/	/	/	9.19 / 9.45
$m_{t,SM,\text{vis}}$	/	/	/	/	8.70 / 7.74
$M(\tau \text{light jet}, \text{min})$	/	/	/	/	4.94 / 1.57
$\eta_{\tau,\text{max}}$	/	/	/	/	6.26 / 6.03
m_W^T	/	/	/	/	2.94 / 6.74
$\Delta R(l + b \text{ jet}, \tau + \tau)$	/	/	/	/	6.71 / 8.06
$P_{t,\tau\tau,\text{vis}}$	/	/	/	/	5.61 / 4.78
$m_{t,FCNC,\text{vis}}$	/	/	/	/	7.19 / 5.75

Table 14: The importance (in %) of each variables used in the BDTG training for hadronic channels, the two numbers in the each block are from the two training folds.

	STH $\tau_{\text{had}}\tau_{\text{had}}$	TTH $\tau_{\text{had}}\tau_{\text{had}}$
$p_{T,\tau}$	4.74 / 5.98	2.63 / 4.24
E_{miss}^T	8.28 / 6.58	7.88 / 7.44
$m_{\tau\tau,vis}$	10.07 / 11.46	11.66 / 10.74
$\Delta R(\tau, \text{light jet}, \text{min})$	8.33 / 8.20	8.63 / 8.28
$\Delta R(\tau, \tau)$	10.21 / 10.72	10.94 / 11.50
$m_{t,FCNC}$	6.28 / 6.24	8.93 / 9.30
$\Delta\phi(\tau\tau, P_{miss}^T)$	4.56 / 6.20	2.84 / 3.05
$E_{miss}^T \text{centrality}$	6.80 / 4.21	6.78 / 5.06
$m_{\tau,\tau}$	13.63 / 13.73	13.31 / 13.94
$E_{\nu,1}/E_{\tau,1}$	5.48 / 3.78	4.56 / 3.66
$E_{\nu,2}/E_{\tau,2}$	5.24 / 6.80	5.11 / 5.99
$m_{t,SM}$	10.46 / 9.33	11.08 / 10.86
m_W	5.93 / 6.77	5.66 / 5.96

Table 15: The chosen `nCuts` and `NTrees` value for each channel.

678 As a cross check, the comparisons between BDT distributions in testing samples, as well as the test even
 679 and test odd ROC curves, are shown in Figure 33 and 34.

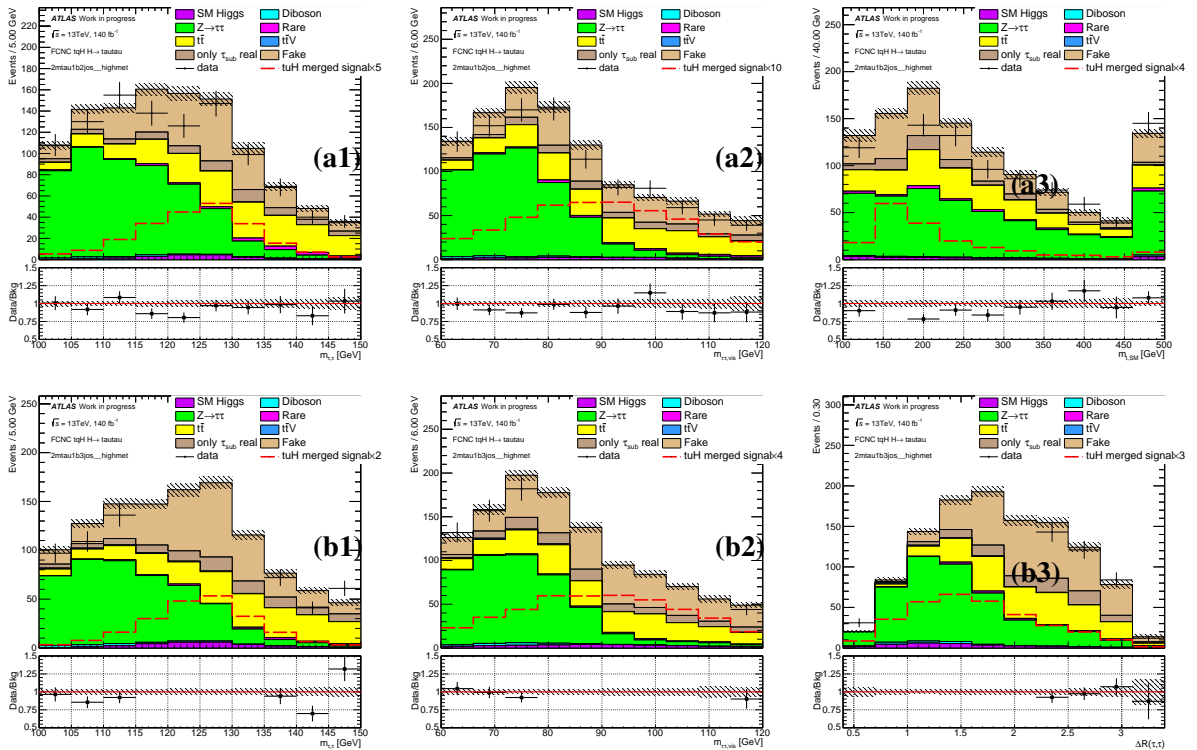


Figure 30: The BDT input distributions for the background and merged signal in the STH $\tau_{\text{had}}\tau_{\text{had}}$ (a1-3), TTH $\tau_{\text{had}}\tau_{\text{had}}$ (b1-3)

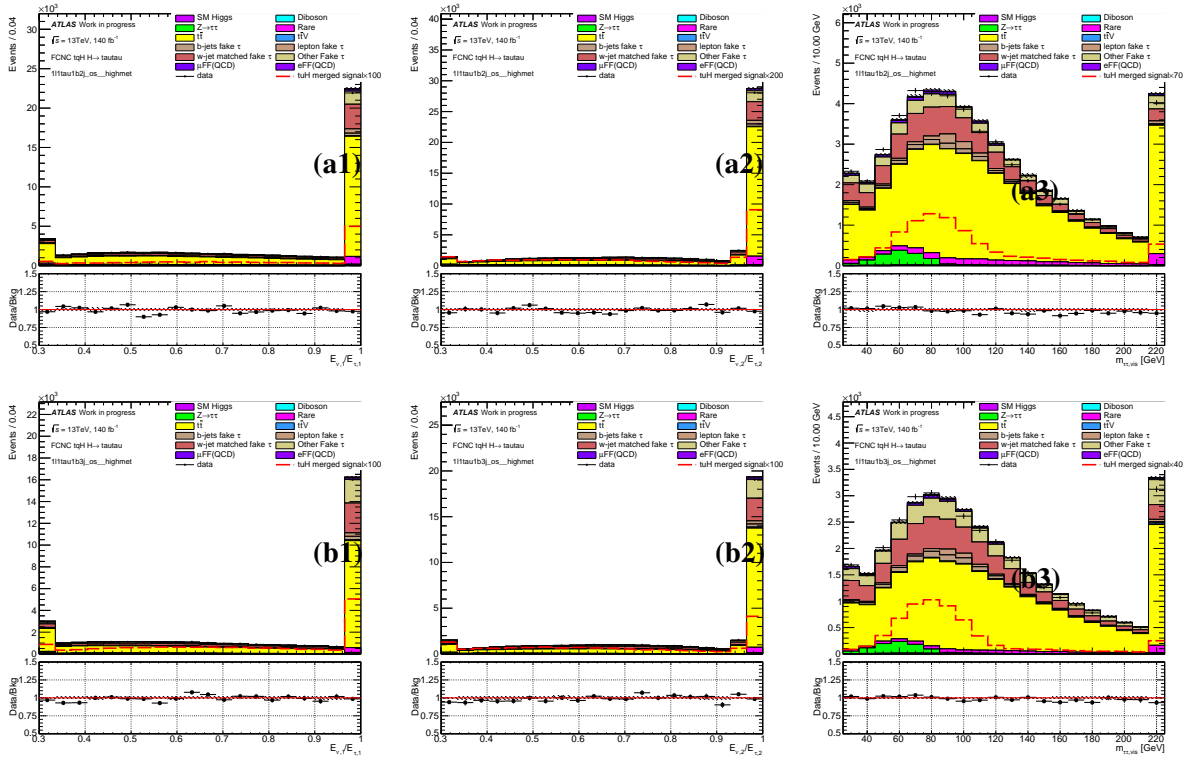


Figure 31: The BDT input distributions for the background and merged signal in the STH $\tau_{\text{lep}}\tau_{\text{had}}$ (a1-3), TTH $\tau_{\text{lep}}\tau_{\text{had}}$ (b1-3).

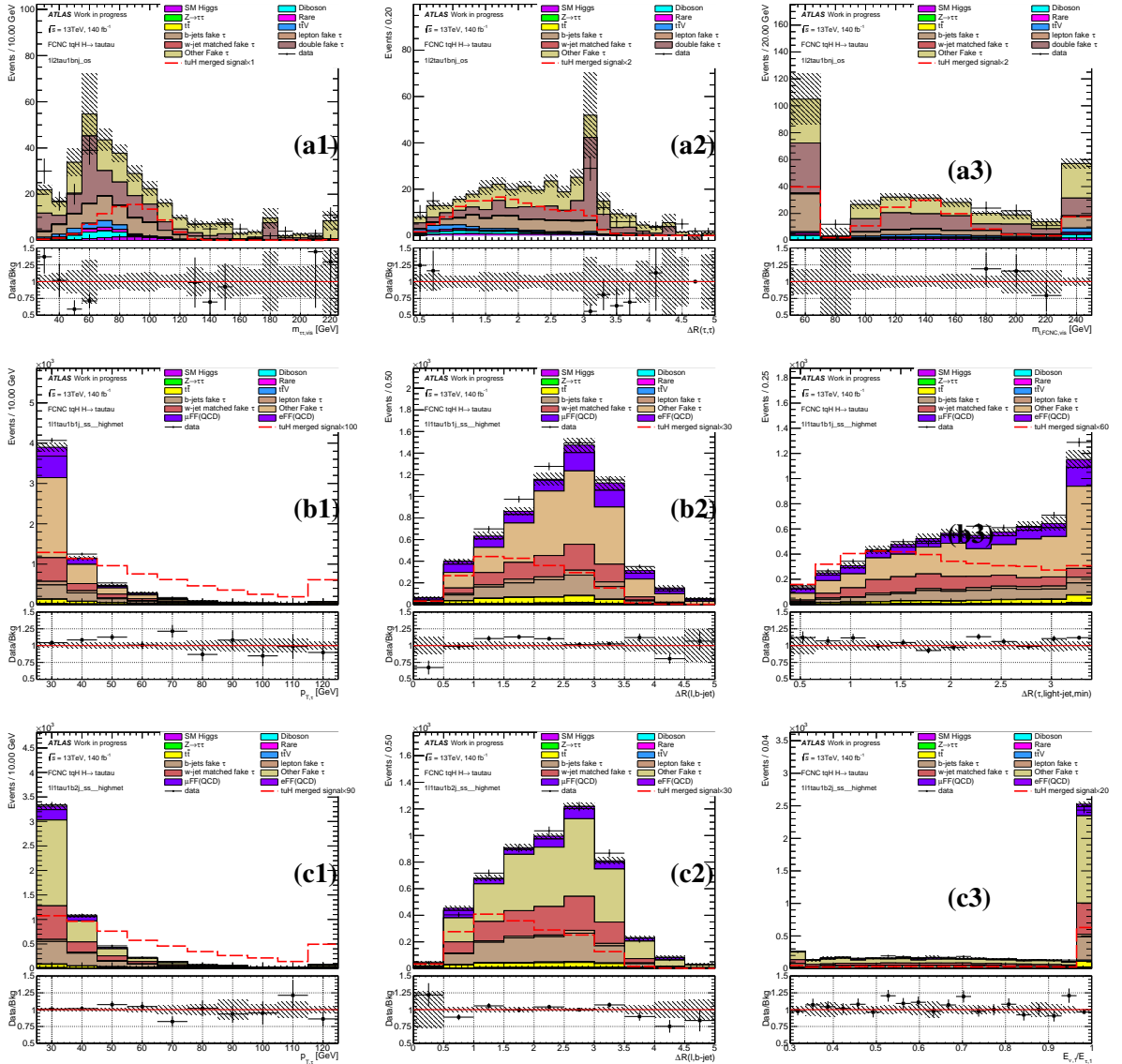


Figure 32: The BDT input distributions for the background and merged signal in the $l\tau_{\text{had}}\tau_{\text{had}}$ (a1-3), $l\tau_{\text{had}} 1j$ (b1-3), $l\tau_{\text{had}} 2j$ (c1-3) channels.

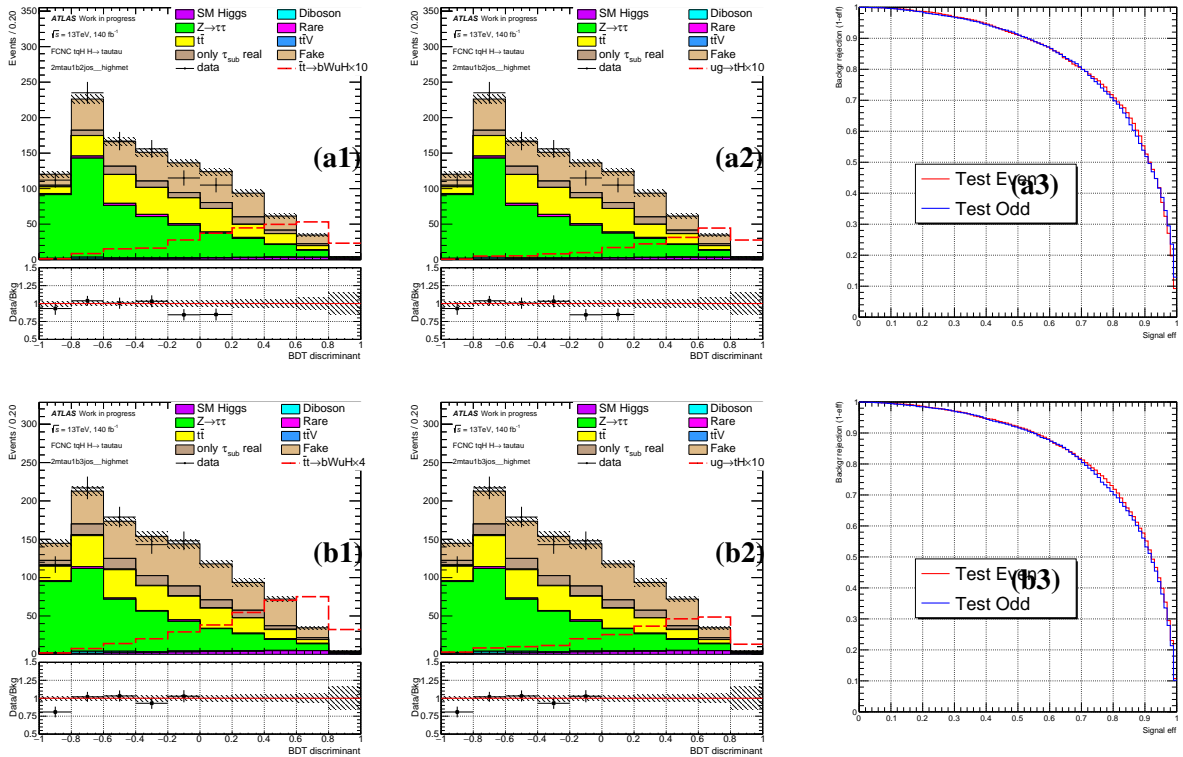


Figure 33: The BDT output distributions for the background and TT signal (a1, b1), background and ST signal (a2, b2) and ROC curves (a3, b3) in the STH $\tau_{\text{had}}\tau_{\text{had}}$ (a1-3), TTH $\tau_{\text{had}}\tau_{\text{had}}$ (b1-3).

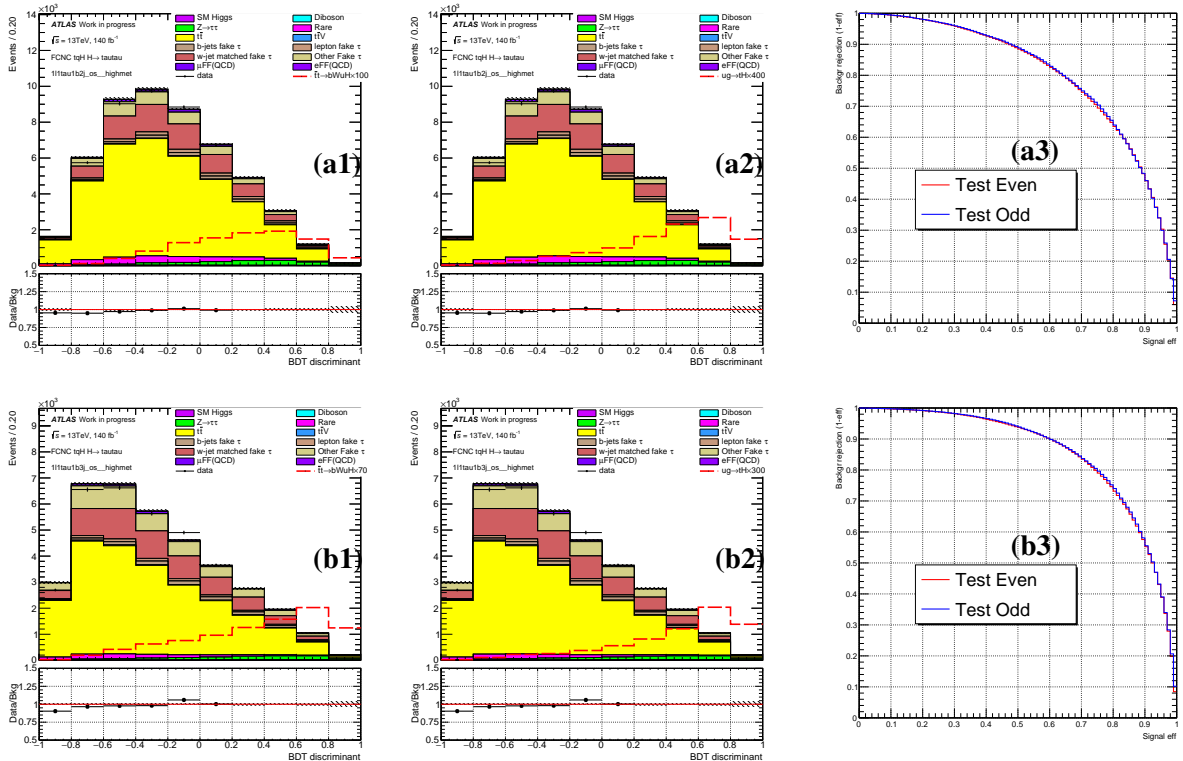


Figure 34: The BDT output distributions for the background and TT signal (a1, b1), background and ST signal (a2, b2) and ROC curves (a3, b3) in the STH $\tau_{\text{lep}}\tau_{\text{had}}$ (a1-3), TTH $\tau_{\text{lep}}\tau_{\text{had}}$ (b1-3).

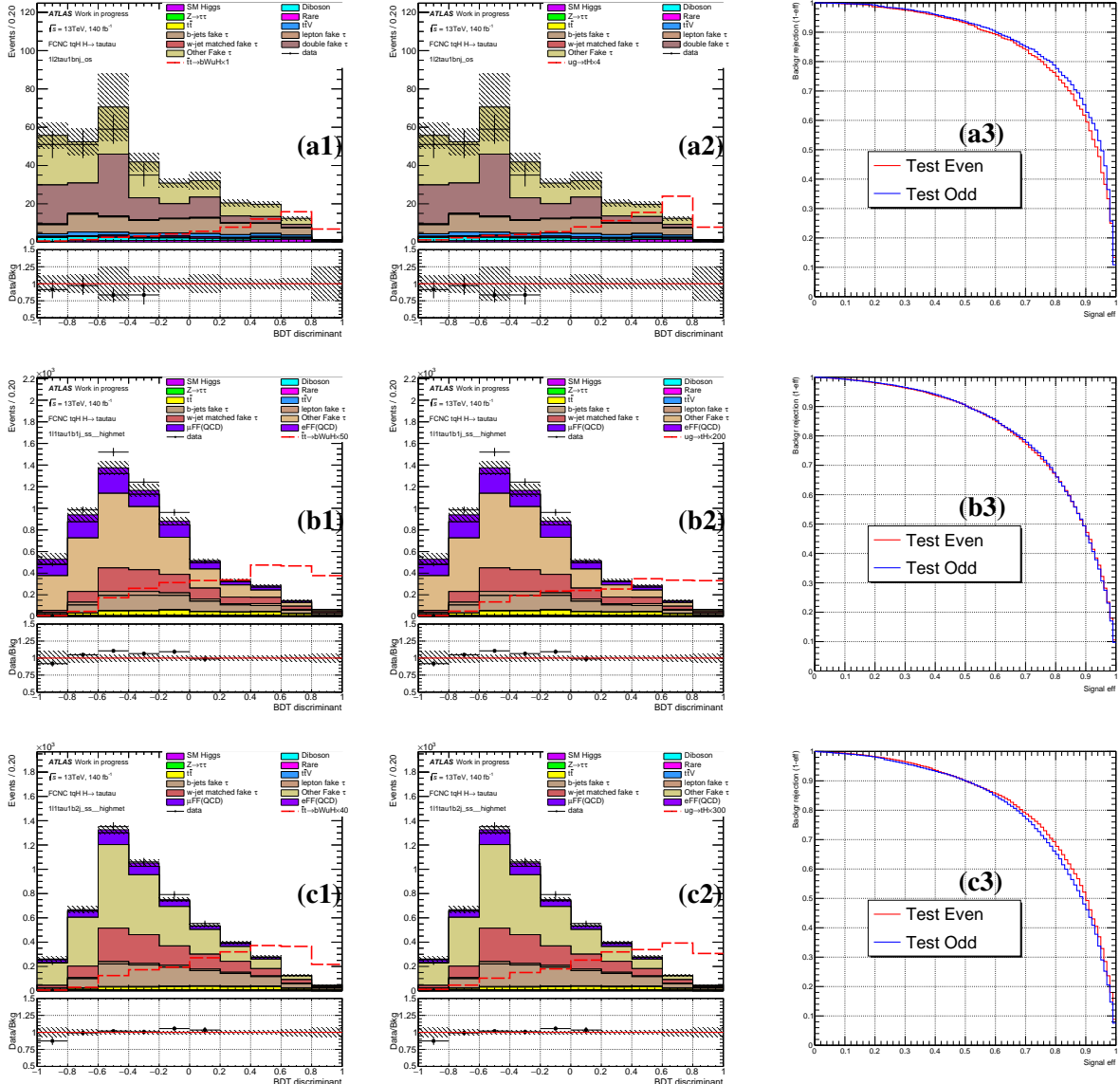


Figure 35: The BDT output distributions for the background and TT signal (a1, b1, c1), background and ST signal (a2, b2, c2) and ROC curves (a3, b3, c3) in the $l\tau_{had}\tau_{had}$ (a1-3), $\tau_{had} 1j$ (b1-3), $\tau_{had} 2j$ (c1-3) channels.

680 11 Systematic uncertainties

681 The signal efficiency and the background estimations are affected by uncertainties associated with the
 682 detector simulation, the signal modelling and the data-driven background determination. In the combined
 683 fit, these uncertainties are called Nuisance Parameters (NP), as opposed to the parameter of interest, the
 684 signal strength, which is a scaling factor applied on the total signal events.

685 Any systematic effect on the the overall normalisation or shape of the final BDT distribution in the signal
 686 region is considered. In `TRExFitter` [62], the NP pruning is applied, which means that NPs whose
 687 impact are less than a certain threshold are discarded. The lower thresholds to remove a shape systematic
 688 and a normalisation systematic from the fit are both 1% in the fit.

689 11.1 Luminosity (TBD)

690 The integrated luminosity measurement has an uncertainty of 1.7% for the combined Run-2 data, and it
 691 is applied to all simulated event samples.

692 11.2 Detector-related uncertainties (TBD)

693 Uncertainties related to the detector are included for the signal and backgrounds that are estimated using
 694 simulation. These uncertainties are also taken into account for the simulated events that enter the data-
 695 driven background estimations. All instrumental systematic uncertainties arising from the reconstruction,
 696 identification and energy scale of electrons, muons, (b -)jets and the soft term of the E_T^{miss} measurement
 697 are considered. The effect of the energy scale uncertainties on the objects is propagated to the E_T^{miss}
 698 calculation. These systematics include uncertainty associated with:

- 699 • The electron and muon trigger, reconstruction, identification and isolation efficiencies. These are
 700 estimated with the tag-and-probe method on the $Z \rightarrow ll$, $J/\psi \rightarrow ll$ and $W \rightarrow l\nu$ events [63].
- 701 • Electron and muon momentum scales. They are estimated from the early 13 TeV $Z \rightarrow ll$ events.
- 702 • Jet energy scale (JES) and resolution (JER). The JES uncertainty is estimated by varying the jet
 703 energies according to the uncertainties derived from simulation and in-situ calibration measurements
 704 using a model with a reduced set of 38 orthogonal NPs [64] which has up to 30% correlation losses,
 705 which are assumed to be uncorrelated, and the induced changes can be added in quadrature. The
 706 individual scale variations on the jets are parameterised in p_T and η . The total JES uncertainty is
 707 below 5% for most jets and below 1% for central jets with pT between 300 GeV and 2 TeV. The
 708 difference between the JER in data and MC is represented by one NP. It is applied on the MC by

smearing the jet p_T within the prescribed uncertainty. JVT is applied in the analysis to select jets from hard-scattered vertices. It was found that different MC generators (and different fragmentation models) lead to efficiency differences of up to 1%, and the uncertainty on the efficiency measurement was found to be around 0.5%. Two NPs are assigned for the JVT efficiency, one for the central and the other for the forward jets.

- Calibration of the E_T^{miss} . The uncertainties on E_T^{miss} due to systematic shifts in the corrections for leptons and jets are accounted for in a fully correlated way in their evaluation for those physics objects, and are therefore not considered independently here. The systematic uncertainty assigned to the track-based soft term used in the E_T^{miss} definition quantifies the resolution and scale of the soft term measurement by using the balance between hard and soft contributions in $Z \rightarrow \mu\mu$ events. The uncertainties are studied using the differences between Monte Carlo generators, using Powheg+Pythia8 as the nominal generator [65]. One NP is assigned for the soft-track scale, and two NPs for the soft-track resolution.
- Jet flavour tagging systematics. The uncertainties on the b -tagging are assessed independently for b , c and light-flavour quark jets, with extrapolation factors [66]. The efficiencies and mis-tag rates are measured in data using the methods described in [67]-[68] with the 2015, 2016 and 2017 data set. There are 19 NPs assigned for the flavour tagging systematics (so-called “Loose” reduced set, with 5 NPs for light flavor, 4 for c , 9 for b , and 1 for extrapolation).
- Pileup. The uncertainty on the pileup reweighting is evaluated by varying the pileup scale factors by 1σ based on the reweighting of the average interactions per bunch crossing. However, this uncertainty is highly correlated with the luminosity uncertainty and may be an overestimate.
- Tau object systematics. These include the τ_{had} reconstruction, identification and trigger efficiencies, the efficiency for tau-electron overlap removal of true τ_{had} , the one for tau-electron overlap removal of true electrons faking τ_{had} , and the one for a “medium” BDT electron rejection. There are also three NPs that cover the tau energy scale (TES) systematics due to the modeling of the detector geometry (TAU_TES_DETECTOR), the measurement in the tag-and-probe analysis (TAU_TES_INSITU) and the Geant4 shower model (TAU_TES_MODEL). The systematics are based on detailed MC variation study, as well as the Run-2 $Z \rightarrow \tau\tau$ data for insitu calibrations of the tau TES and trigger efficiencies, as documented in [51] and the dedicated software tools [54] recommended by the Tau CP Woking Group [56].

11.3 Uncertainties on fake background estimations

Systematic uncertainties as described in Sec. 9 are considered in the final fit. The uncertainties of the fake estimation for the leptonic channels and hadronic channels are correlated respectively but independent between them.

- 743 In the leptonic channels, they are named `fakeSFNP_Xprong_ptbinX_*` for tau fakings modelled by MC
 744 and `ABCD*` for QCD faking modelled by DD.
- 745 In the hadronic channels, they are named `FFNP_Xprong_ptbinX_etabin*` for the statistical uncertainties
 746 of the FFs derived from the W+jets control region. `FFNP_OS_CR` and `FFNP_SS_CR` are one-sided NP for the
 747 systematic uncertainties of the FFs derived in the OS and SS control region respectively. `only τ_{sub} real`
 748 `modelling` is the uncertainty of the MC modelling of the events with leading tau fake but sub-leading
 749 tau real, which is varied by 50% to be conservative according to the study in the leptonic channels.

750 11.4 Theoretical uncertainties on the background (TBD)

- 751 Theoretical uncertainties have been applied to the MC background in this analysis. The NNPDF3.0
 752 systematic set (which has 100 variations) is used to get the variation envelope around the nominal PDF,
 753 and the renormalization and factorization scales are varied by a factor of 0.5 and 2.0 around the nominal
 754 values. There are eight such variations. In the final BDT distributions, the largest variations of the eight
 755 per bin are taken.
- 756 The default $t\bar{t}$ sample is generated with Powheg. A separate full-sim $t\bar{t}$ sample generated with Sherpa (0
 757 and 1-jet at NLO, and ≥ 2 jets at LO) is compared with the Powheg sample, and the difference in final
 758 results is treated as the hard scattering systematics [69].
- 759 The default $t\bar{t}$ MC events are showered with Pythia8. A separate sample showered with Herwig7 is
 760 compared with the Pythia8 sample, and the difference is treated as fragmentation and hadronization
 761 systematics [69]. These two samples are both generated with ATLFAST-II [36], and their difference is
 762 then applied to the default full-simulation $t\bar{t}$ sample.
- 763 The Powheg+Pythia8 $t\bar{t}$ MC is also generated with different shower radiations (initial and final-state
 764 radiation modelling). For a sample with increased radiation, the factorisation and renormalization scales
 765 are scaled by 0.5 with respect to their nominal values, the `hdamp` parameter (which controls the amount
 766 of radiation produced by the parton shower in POWHEG-BOX v2) is set to $3m_{\text{top}}$ and the `A14var3cUp` tune
 767 is used. Conversely, for a sample with decreased radiation, the two scales are scaled by 2 with respect to
 768 their nominal values, the `hdamp` is kept at the nominal value of $1.5m_{\text{top}}$ and the `A14var3cDown` tune is
 769 used [69].
- 770 Uncertainty affecting the normalisation of the $V+\text{jets}$ background is estimated to be about 30% according
 771 to the study done in the FCNC $H \rightarrow b\bar{b}$ channel [70]. The uncertainty on the diboson cross section is 5%
 772 [71], on single top +5%/-4% [43][72, 73], on $t\bar{t}V$ 15% [74, 75], and on $t\bar{t}H$ +10%/-13% [76].

773 **11.5 Uncertainties on the signal modelling (TBD)**

774 Since the TT signal samples share the same production as the $t\bar{t}$ process, the systematics listed above for
775 $t\bar{t}$ also apply to the signal. However, because the systematics variation samples are only generated for the
776 SM decays of $t\bar{t}$, only the integral change of the yields observed for the $t\bar{t}$ background with real taus in
777 the FR is used, and applied on the signal in the same region in a fully correlated way. An additional 1.6%
778 uncertainty on $\text{BR}(H \rightarrow \tau\tau)$ is also assigned [39].

779 The fake calibration is also applied to the fake tau part of the signal the same way as the background. The
780 6 NPs are also applied to the signal and fully correlated with the background.

781 12 Fit model and signal extraction

782 The parameter of interest in this search is the signal strength of the FCNC interactions, $\text{BR}(t \rightarrow Hq)$
 783 and corresponding production mode cross section. The statistical analysis of the data employs a binned
 784 likelihood function constructed as the product of Poisson probability terms, in bins of the BDT output.

785 To take into account the systematic uncertainties associated with the MC estimation from different sources
 786 for both the signal and background samples, the fit model incorporates these systematics as extra Gaussian
 787 or Log-Normal constraint terms multiplied with the combined likelihood. The fitted central values and
 788 errors of the systematics parameters, or NPs, are expected to follow a normal distribution centered around 0
 789 with unit width, when the Asimov data is used. The fit model construction is obtained with the `RooFit` and
 790 `RooStats` software, and the model configuration and persistence files (as input to `RooStats`) are produced
 791 by `TRExFitter` [62], which is a software package interface with `HistFactory`. The `TRExFitter`
 792 includes additional features such as histogram smoothing, NP pruning and error symmetrization before
 793 the fits.

794 The correlated bin-by-bin histogram variation corresponds to the up and down variation of each NP.
 795 The independent bin-by-bin fluctuations in the combined MC templates are also treated as NPs. They are
 796 incorporated in the model as extra Poisson constraint terms, and are expected to have a fitted value of 1 and
 797 a fitted error reflecting the relative statistical error in each particular bin. There is one parameter of interest
 798 (POI) freely floating in the fit without any constraints, namely, the signal strength μ (`SigXsecOverSM`)
 799 which is a multiplicative factor on a presumed branching ratio of $\text{BR}(t \rightarrow Hq)=0.2\%$ in this analysis. The
 800 errors associated with the different systematics will be properly propagated to the fitted error of μ in a
 801 simultaneous fit of multiple regions via a profiled likelihood scan by the minimization program `MINUIT`.

802 The one-sided NPs in the analysis, namely, `fakeSFxprongXPtbin`, `ttbar fragmentation`, `ttbar`
 803 `hard scattering`, `JET_BJES_Response`, `JET_JER_DataVsMC_MC16`, `JET_SingleParticle_HighPt`,
 804 `JET_TILECORR_Uncertainty`, `MET_SoftTrk_ResoPara`, `MET_SoftTrk_ResoPerp` are symmetrized.
 805 This is done manually on the MC components of the background. By default, all the kinematic NPs (shape
 806 NPs due to, e.g., energy scales) are smoothed using the default smoothing parameters in `TRExFitter`.
 807 This helps removing the artificial NP constraints due to statistical fluctuations in the systematic variations,
 808 and makes the fit well behaved.

809 Figure 40 shows the ranking of the 25 top NPs along with their pull distributions, produced also with
 810 `TRExFitter`. The highest ranked NP is defined to have the largest impact on μ . The impact is evaluated by
 811 varying the NP under consideration by one σ (either pre or post-fit error) up and down, and afterwards
 812 looking at the relative change in μ under the conditional fit where the NP under consideration is fixed to
 813 its varied new value. Figure 39 shows the pull distributions of all NPs in asimov fit. Normalization and
 814 shape systematics whose impact is less than 1% are removed from the fit.

815 Figure 41 shows the correlation matrix for different NPs. Except for self-correlations, and the correlations
 816 between the normalization factors (including POI) and the others, all the NPs have relatively small
 817 correlations with each other, which justifies the fit models for independent systematics.

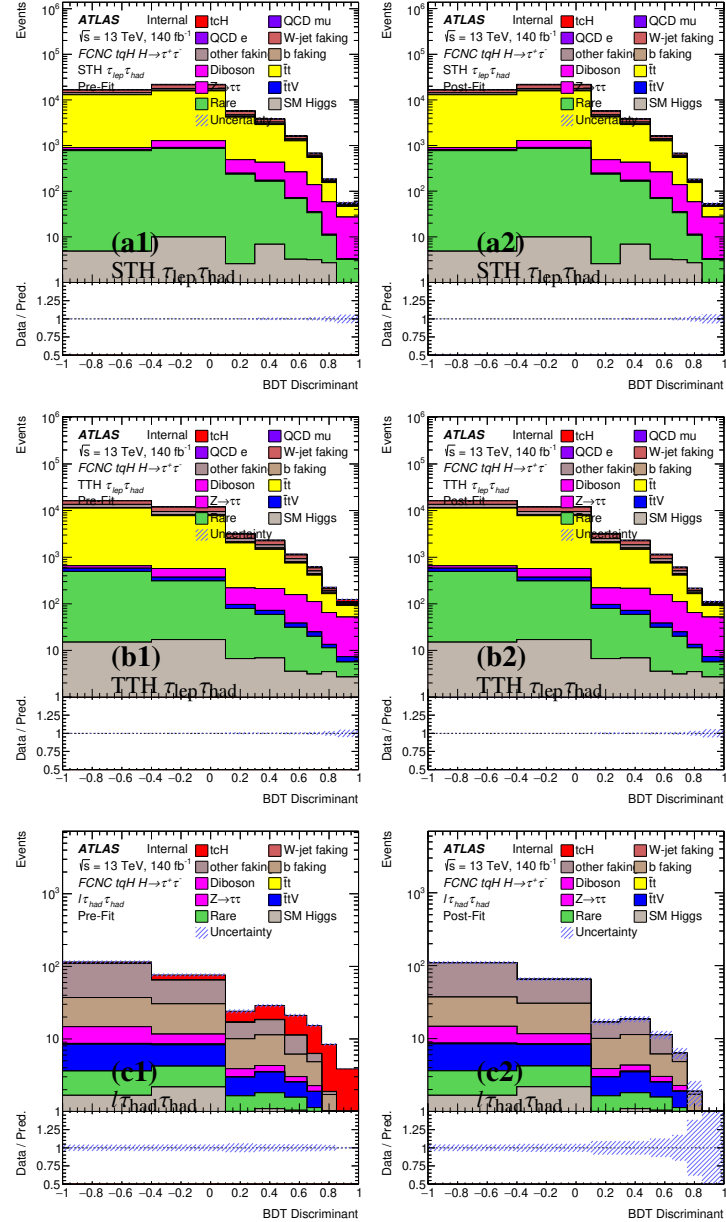


Figure 36: The asimov prefit (left) and postfit (right) BDT distributions in the STH $\tau_{\text{lep}}\tau_{\text{had}}$ (a1-2) and TTH $\tau_{\text{lep}}\tau_{\text{had}}$ (b1-2), $l\tau_{\text{had}}\tau_{\text{had}}$ (c1-2)

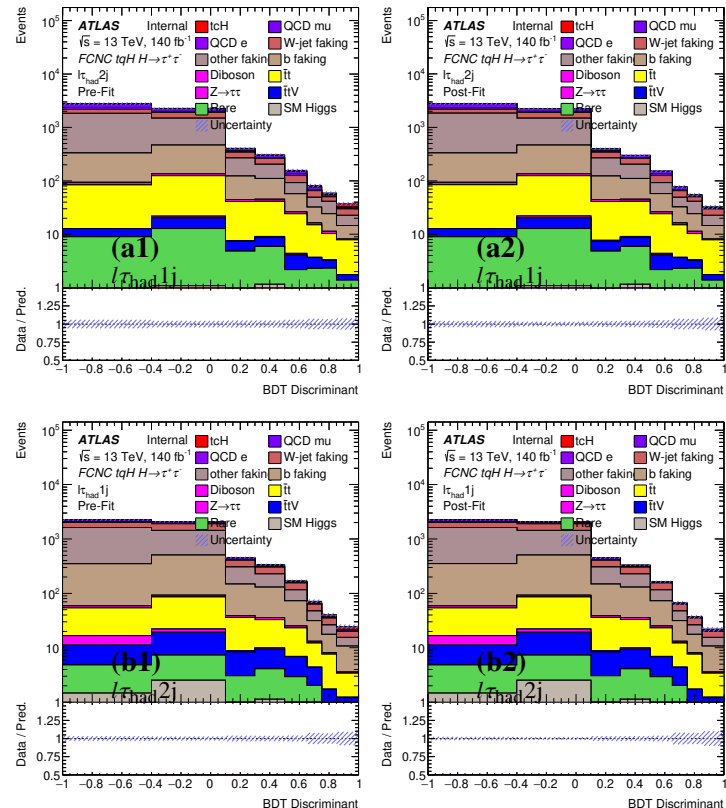


Figure 37: The asimov prefit (left) and postfit (right) BDT distributions in the $l_{\tau_{\text{had}}1j}$ (a1-2) and $l_{\tau_{\text{had}}2j}$ (b1-2)

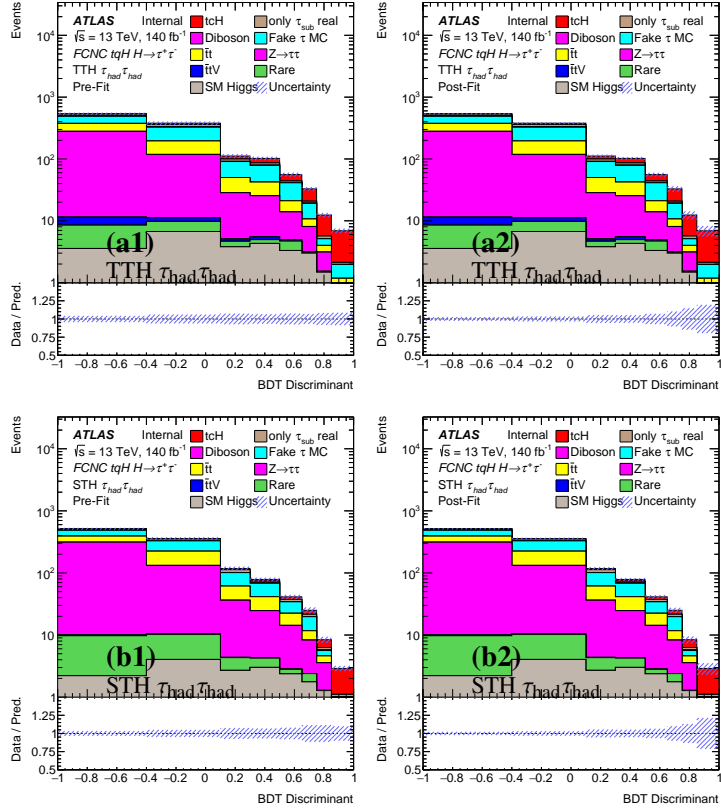


Figure 38: The asimov prefit (left) and postfit (right) BDT distributions in the TTH $\tau_{\text{had}}\tau_{\text{had}}$ (a1-2) and STH $\tau_{\text{had}}\tau_{\text{had}}$ (b1-2)

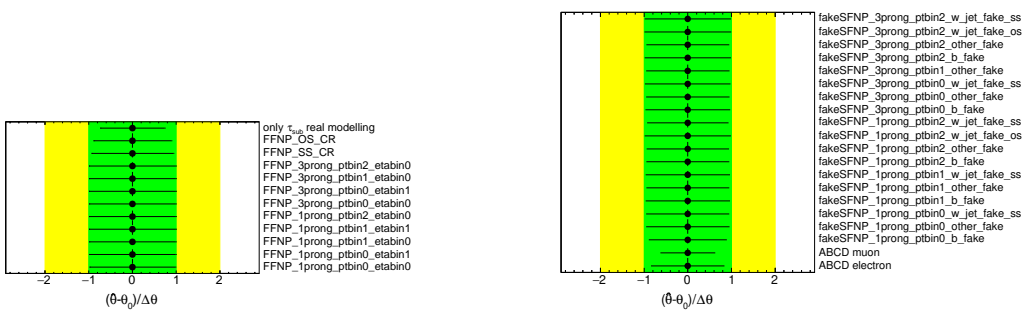


Figure 39: The pull distributions of asimov fit in $\tau_{\text{had}}\tau_{\text{had}}$ channels (left) combined and leptonic channels combined (right) in terms of tuH merged signal .

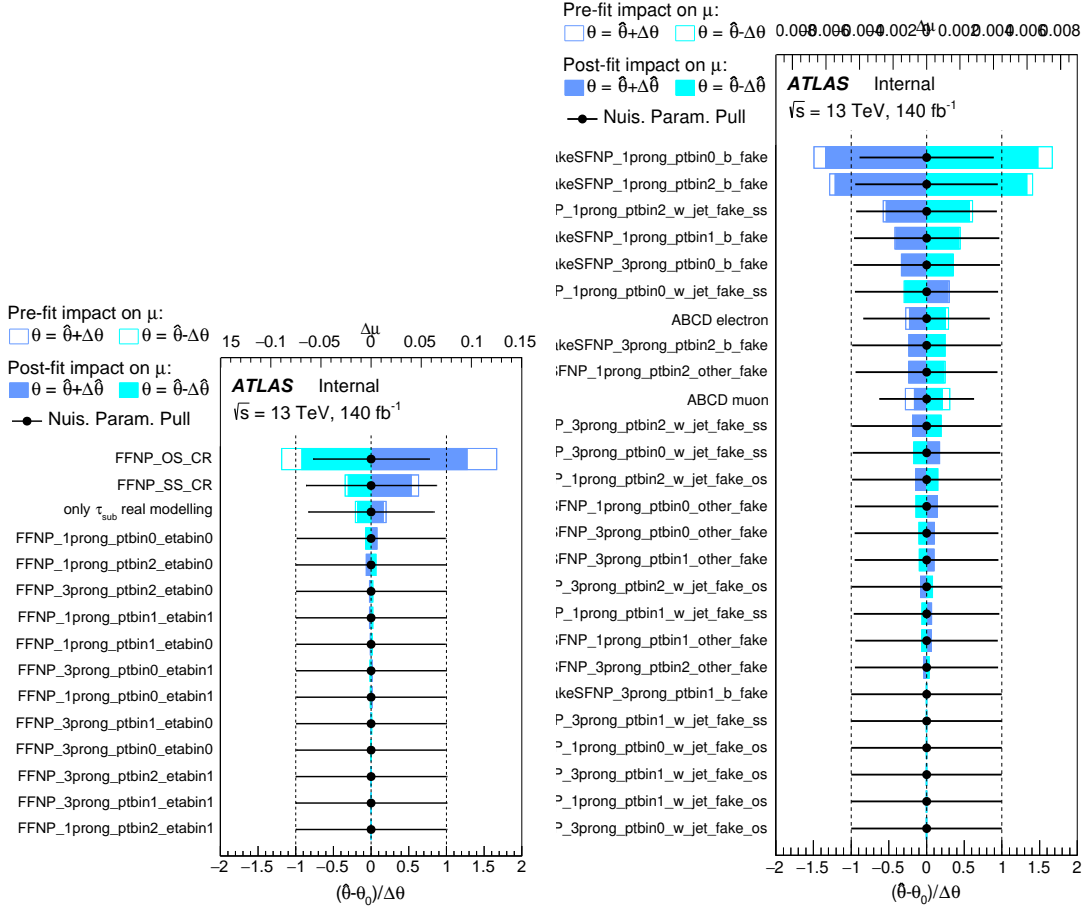


Figure 40: The asimov fit ranking of the top 25 NPs for $\tau_{\text{had}}\tau_{\text{had}}$ channels (left) and leptonic channels in terms of tuH merged signal. The scale of the relative impact on μ (the pull) of the NPs is shown on the top (bottom) axis.

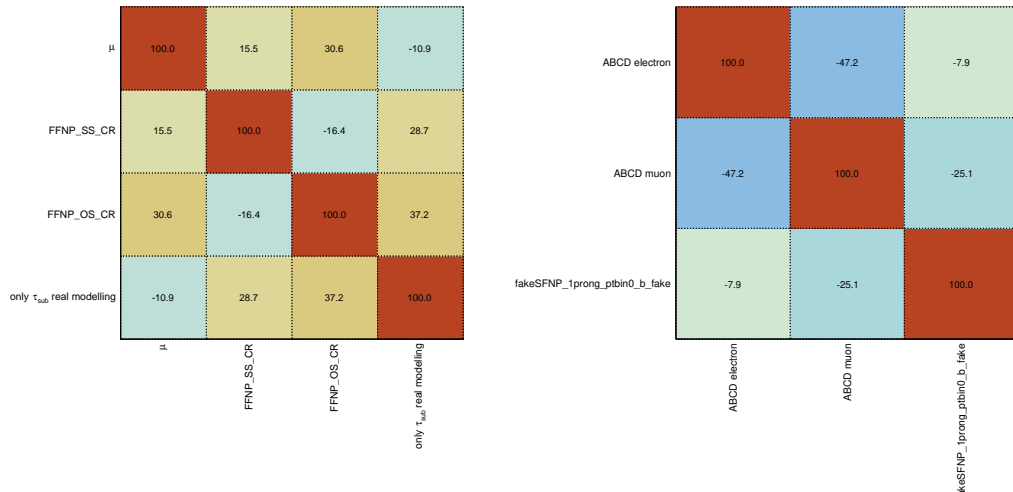


Figure 41: The asimov fit correlation matrix (%) of different NPs, with a threshold of 20% for $\tau_{\text{had}}\tau_{\text{had}}$ channels (left) combined and lepton channels combined (right).

Table 16: The statistical only significance in leptonic channels based on BDT discriminant.

	$l\tau_{had}\ 1j$	STH $\tau_{lep}\tau_{had}$	$l\tau_{had}\ 2j$
$\bar{t}t \rightarrow bWcH$	1.34	0.74	1.28
$cg \rightarrow tH$	0.05	0.06	0.03
tcH merged signal	1.39	0.80	1.31
$\bar{t}t \rightarrow bWuH$	1.43	0.76	1.38
$ug \rightarrow tH$	0.29	0.39	0.22
tuH merged signal	1.71	1.12	1.59
	TTH $\tau_{lep}\tau_{had}\ os$	$l\tau_{had}\tau_{had}\ os$	
$\bar{t}t \rightarrow bWcH$	1.55	6.08	
$cg \rightarrow tH$	0.07	0.58	
tcH merged signal	1.62	6.48	
$\bar{t}t \rightarrow bWuH$	1.65	6.47	
$ug \rightarrow tH$	0.40	2.43	
tuH merged signal	2.04	8.26	

Table 17: The statistical only significance in hadronic channels based on BDT discriminant.

	STH $\tau_{had}\tau_{had}$	TTH $\tau_{had}\tau_{had}$
$\bar{t}t \rightarrow bWcH$	1.70	4.87
$cg \rightarrow tH$	0.29	0.25
tcH merged signal	1.95	5.08
$\bar{t}t \rightarrow bWuH$	1.68	5.08
$ug \rightarrow tH$	1.67	1.24
tuH merged signal	3.15	6.12

13 Results

- The statistical only significance based on BDT discriminant is shown in Table 16, 17.
The significance of any small observed excess in data is evaluated by quoting the p -values to quantify the level of consistency of the data with the BR=0 hypothesis. The asymptotic approximation in [77] is used. The test statistic used for the exclusion limits derivation is the \tilde{q}_μ test statistic and for the p -values the q_0 test statistic² [77].

² The definition of the test statistics used in this search is the following:

$$\tilde{q}_\mu = \begin{cases} -2 \ln(\mathcal{L}(\mu, \hat{\theta}) / \mathcal{L}(0, \hat{\theta})) & \text{if } \hat{\mu} < 0 \\ -2 \ln(\mathcal{L}(\mu, \hat{\theta}) / \mathcal{L}(\hat{\mu}, \hat{\theta})) & \text{if } 0 \leq \hat{\mu} \leq \mu \\ 0 & \text{if } \hat{\mu} > \mu \end{cases}$$

824 The 95% CL upper limits on tqH interaction with $\text{BR}(t \rightarrow Hq) = 0.2\%$ as reference are given in Table 18
 825 and 19 for leptonic and hadronic channels respectively. The expected limits combining all channels are
 826 given in Table 20. The sensitivity is significantly improved compared to the published results 3. The best
 827 asimov fit values with S+B hypothesis are given in Table 21. Note that the current results only consists of
 828 fake estimation NPs.

Table 18: The expected 95% CL exclusion upper limits on $\text{BR}(t \rightarrow Hc)$ and $\text{BR}(t \rightarrow Hu)$ (0.2%) with the Asimov (B-only) in the leptonic channels.

	$l\tau_{\text{had}}2j$	$l\tau_{\text{had}}1j$	STH $\tau_{\text{lep}}\tau_{\text{had}}$
$\bar{t}t \rightarrow bWcH$	$1.94^{+0.77}_{-0.54}$	$1.85^{+0.74}_{-0.52}$	$3.16^{+1.24}_{-0.88}$
$cg \rightarrow tH$	/	/	/
tcH merged signal	$1.89^{+0.75}_{-0.53}$	$1.78^{+0.71}_{-0.50}$	$2.90^{+1.14}_{-0.81}$
$\bar{t}t \rightarrow bWuH$	$1.78^{+0.71}_{-0.50}$	$1.74^{+0.69}_{-0.49}$	$3.03^{+1.19}_{-0.85}$
$ug \rightarrow tH$	$11.17^{+4.48}_{-3.12}$	$8.51^{+3.41}_{-2.38}$	$5.48^{+2.19}_{-1.53}$
tuH merged signal	$1.54^{+0.61}_{-0.43}$	$1.45^{+0.58}_{-0.40}$	$2.00^{+0.79}_{-0.56}$
	TTH $\tau_{\text{lep}}\tau_{\text{had}}$	$l\tau_{\text{had}}\tau_{\text{had}}$	Combined
$\bar{t}t \rightarrow bWcH$	$1.44^{+0.57}_{-0.40}$	$0.29^{+0.13}_{-0.08}$	$0.27^{+0.12}_{-0.08}$
$cg \rightarrow tH$	/	$3.66^{+1.60}_{-1.02}$	$3.60^{+1.57}_{-1.00}$
tcH merged signal	$1.38^{+0.55}_{-0.39}$	$0.27^{+0.12}_{-0.07}$	$0.26^{+0.11}_{-0.07}$
$\bar{t}t \rightarrow bWuH$	$1.35^{+0.53}_{-0.38}$	$0.27^{+0.12}_{-0.07}$	$0.25^{+0.11}_{-0.07}$
$ug \rightarrow tH$	$5.56^{+2.20}_{-1.55}$	$0.79^{+0.34}_{-0.22}$	$0.76^{+0.33}_{-0.21}$
tuH merged signal	$1.09^{+0.43}_{-0.30}$	$0.20^{+0.09}_{-0.06}$	$0.19^{+0.08}_{-0.05}$

Table 19: The expected 95% CL exclusion upper limits on $\text{BR}(t \rightarrow Hc)$ and $\text{BR}(t \rightarrow Hu)$ (0.2%) with the Asimov (B-only) in the hadronic channels.

	STH $\tau_{\text{had}}\tau_{\text{had}}$	TTH $\tau_{\text{had}}\tau_{\text{had}}$	Combined
$\bar{t}t \rightarrow bWcH$	$1.49^{+0.66}_{-0.42}$	$0.52^{+0.21}_{-0.15}$	$0.47^{+0.20}_{-0.13}$
$cg \rightarrow tH$	$9.12^{+4.06}_{-2.55}$	$11.79^{+4.69}_{-3.29}$	$7.12^{+3.03}_{-1.99}$
tcH merged signal	$1.28^{+0.57}_{-0.36}$	$0.50^{+0.21}_{-0.14}$	$0.45^{+0.19}_{-0.12}$
$\bar{t}t \rightarrow bWuH$	$1.47^{+0.64}_{-0.41}$	$0.50^{+0.21}_{-0.14}$	$0.46^{+0.19}_{-0.13}$
$ug \rightarrow tH$	$1.45^{+0.65}_{-0.41}$	$2.23^{+0.90}_{-0.62}$	$1.19^{+0.52}_{-0.33}$
tuH merged signal	$0.73^{+0.33}_{-0.21}$	$0.41^{+0.17}_{-0.12}$	$0.35^{+0.14}_{-0.10}$

and

$$q_0 = \begin{cases} -2 \ln(\mathcal{L}(0, \hat{\theta}) / \mathcal{L}(\hat{\mu}, \hat{\theta})) & \text{if } \hat{\mu} \geq 0 \\ 0 & \text{if } \hat{\mu} < 0 \end{cases}$$

where $\mathcal{L}(\mu, \theta)$ denotes the binned likelihood function, μ is the parameter of interest (i.e. the signal strength parameter), and θ denotes the nuisance parameters. The pair $(\hat{\mu}, \hat{\theta})$ corresponds to the global maximum of the likelihood, whereas $(x, \hat{\theta})$ corresponds to a conditional maximum in which μ is fixed to a given value x .

Table 20: The combined expected 95% CL exclusion upper limits on $\text{BR}(t \rightarrow Hc)$ and $\text{BR}(t \rightarrow Hu)$ (0.2%) with the Asimov (B-only).

	tcH merged signal	tuH merged signal
Combined Limit	$0.23^{+0.10}_{-0.06}$	$0.18^{+0.08}_{-0.05}$

Table 21: The best asimov fit values with S+B hypothesis.

	tcH	tuH
$\tau_{\text{had}}\tau_{\text{had}}$	$1.00^{+0.23+X.XX}_{-0.22-X.XX}$	$1.00^{+0.18+X.XX}_{-0.18-X.XX}$
leptonic channels	$1.00^{+0.19+X.XX}_{-0.18-X.XX}$	$1.00^{+0.16+X.XX}_{-0.15-X.XX}$

829 The search for the FCNC decay $t \rightarrow Hq, H \rightarrow \tau\tau$ with the ATLAS detector at the LHC using 13 TeV
 830 data was presented in this note. The best-fit values for $\text{BR}(t \rightarrow Hc)$ and $\text{BR}(t \rightarrow Hu)$ are found to be
 831 $-X.XX^{+X.XX}_{-X.XX}\%$ and $-X.XX^{+X.XX}_{-X.XX}\%$ respectively, based on 140 fb^{-1} of data collected from 2015 to 2018.
 832 The observed (expected) 95% CL upper limits on $\text{BR}(t \rightarrow Hc)$ and $\text{BR}(t \rightarrow Hu)$ are found to be $X.XX\%$
 833 ($X.XX^{+X.XX}_{-X.XX}\%$) and $X.XX\%$ ($X.XX^{+X.XX}_{-X.XX}\%$), respectively.

834 Appendix

835 A Sample DSID list

836 $t\bar{t} \rightarrow bWcH, W \rightarrow lv, H \rightarrow \tau^+\tau^-$: 411172 411173

837 $t\bar{t} \rightarrow bWcH$ 1 lepton filter: 410694 410695

838 $t\bar{t} \rightarrow bWcH, W \rightarrow q\bar{q}, H \rightarrow \tau^+\tau^-$: 411170 411171

839 $cg \rightarrow tH, H \rightarrow \tau^+\tau^-$: 412104 412105 412100 412101

840 $t\bar{t} \rightarrow bWuH, W \rightarrow lv, H \rightarrow \tau^+\tau^-$: 411176 411177

841 $t\bar{t} \rightarrow bWuH$ 1 lepton filter: 410692 410693

842 $t\bar{t} \rightarrow bWuH, W \rightarrow q\bar{q}, H \rightarrow \tau^+\tau^-$: 411174 411175

843 $ug \rightarrow tH, H \rightarrow \tau^+\tau^-$: 412098 412099 412102 412103

844 Diboson: 364250 363355 363356 363357 363358 363359 363360 363489 345708 345716 364253 364254
845 364255

846 Rare: 410080 410081 304014 341998 342004 343267 343270 410408 410560 345716 345708 410644
847 410645 410646 410647

848 SM Higgs: 342001 342282 342283 342284 342285 343273 345873 345874 345875

849 $t\bar{t}$: 410470 410471

850 $t\bar{t}V$: 410155 410156 410157 410218 410219 410220 410276 410277 410278 410397 410398 410399

851 $W+jets$: 364156 364157 364158 364159 364160 364161 364162 364163 364164 364165 364166 364167
852 364168 364169 364170 364171 364172 364173 364174 364175 364176 364177 364178 364179 364180
853 364181 364182 364183 364184 364185 364186 364187 364188 364189 364190 364191 364192 364193
854 364194 364195 364196 364197

855 $Z \rightarrow l^+l^-$: 364100 364101 364102 364103 364104 364105 364106 364107 364108 364109 364110
856 364111 364112 364113 364114 364115 364116 364117 364118 364119 364120 364121 364122 364123
857 364124 364125 364126 364127 364198 364199 364200 364201 364202 364203 364204 364205 364206
858 364207 364208 364209

859 $Z \rightarrow \tau^+\tau^-$: 364128 364129 364130 364131 364132 364133 364134 364135 364136 364137 364138
860 364139 364140 364141 364210 364211 364212 364213 364214 364215

861 B Derivation and framework level cuts

862 A number of event cuts are applied before getting to the signal enhanced regions with the back-
 863 ground suppressed. Then the DAOD_HIGG8D1 (DAOD_HIGG4D3) derivation is feed to ttHMultiAna
 864 (`xTauFramework`) to produce n-tuples for leptonic (hadronic) channels, where ttHMultiAna is AnalysisTop
 865 [78] based. The list of event-level selection criteria is as follows:

- 866 1. DAOD_HIGG8D1 and DAOD_HIGG4D3 ($\tau_{\text{had}} \tau_{\text{had}}$) derivations are used for this analysis. At the
 867 derivation level, the following cuts are applied:
 - 868 • In DAOD_HIGG8D1, trigger skimming: all electron, muon, tau triggers; Offline skimming:
 869 at least 2 light leptons or at least 1 lepton plus 1 tau.
 - 870 • In DAOD_HIGG4D3, no trigger skimming. Offline skimming: 2taus
- 871 2. At the ttHMultiAna level, skim cuts in [58] are applied , then only the events passing either of the
 872 following cut are saved for the n-tuples:
 - 873 • At least two light leptons passing loose identification criteria with leading lepton $p_T > 15$
 874 GeV and subleading lepton $p_T > 5$ GeV within $|\eta| < 2.6$.
 - 875 • At least one light lepton passing loose identification criterua with $p_T > 15$ GeV and $|\eta| < 2.5$,
 876 and at least one hadronic tau. The tau lepton has to pass RNN loose requirement with $p_T > 15$
 877 GeV and $|\eta| < 2.5$.
- 878 3. If the tau candidate overlaps with a muon or fails Loose electron-BDT cut, the event is removed.
- 879 4. If the event neither fires single lepton nor dilepton trigger, the event is removed.
- 880 5. If the lepton fails tight lepton selection, the event is removed.
- 881 6. If the leading or sub-leading tau candidate has p_T less than 25GeV or fails RNN medium criteria,
 882 the event is removed.
- 883 7. If the event has two same-charged lepton, the electrons are required to pass Loose charge BDT. (Not
 884 affecting this analysis.)
- 885 8. If the tau is tagged as b -jet by 70% WP, the event is removed.
- 886 9. At the `xTauFramework` level, skim cuts are applied to reduce the ntuple size:
 - 887 • No leptons.
 - 888 • At least 1 RNN Loose tau.

- 889 • At least 3 jets with $p_T > 30$ GeV, $|\eta| < 4.5$ and passing either central or forward JVT cuts,
890 with at least 1 b-tagged. (The jets are further required to have $|\eta| < 2.5$ at n-tuple level to be
891 consistent with leptonic channels.)

- 892 • Taus trigger matched.

- 893 • LooseBad Event Cleaning.

- 894 • Leading tau $p_T > 40$ GeV, sub-leading tau $p_T > 30$ GeV, two taus comes from a single vertex.

- 895 • Leading jet $p_T > 70$ GeV, $|\eta| < 3.2$

- 896 • $E_T^{\text{miss}} > 15$ GeV.

- 897 • In the case of data, GRL cut as defined in Sec. 5.2 is also applied.

898 10. At least one primary vertex exists in the event. The primary vertex is defined as the vertex that has
899 the largest sum of track p_T^2 associated to it, and has at least 4 tracks with $|z_0| < 100$ mm.

900 The corresponding cutflow for the n-tuple level selection and each channel are given in Table 22 - 30.

Table 22: The cutflow tables for the preselection in the hadronic channels.

	SM Higgs	W+jets	Diboson	$Z \rightarrow ll$
n-tuple	676.62 ± 1.88	11732.12 ± 124.96	1051.56 ± 11.87	1166.92 ± 48.08
pass trigger	543.42 ± 1.73	7304.42 ± 97.16	755.24 ± 9.61	904.67 ± 31.08
ntrack = 1,3	374.89 ± 1.53	3484.23 ± 85.34	449.70 ± 7.17	541.43 ± 25.28
ele veto	264.47 ± 1.31	2084.42 ± 49.96	299.13 ± 5.82	4.32 ± 0.92
jet num ≥ 3	206.39 ± 1.05	1385.95 ± 44.66	229.60 ± 5.05	3.47 ± 0.76
tau rnn score ≥ 0.01	187.64 ± 1.03	1014.28 ± 23.94	202.37 ± 4.67	2.03 ± 0.28
SR+CR	102.07 ± 0.83	729.27 ± 20.19	149.02 ± 3.89	0.99 ± 0.22
	$Z \rightarrow \tau\tau$	Rare	$t\bar{t}$	$t\bar{t}V$
n-tuple	14869.01 ± 55.47	14329.96 ± 52.89	189864.11 ± 210.84	440.49 ± 2.06
pass trigger	13057.21 ± 50.78	9324.55 ± 42.29	125670.32 ± 171.27	337.71 ± 1.80
ntrack = 1,3	10351.28 ± 45.70	4732.10 ± 30.15	63031.31 ± 119.31	209.87 ± 1.45
ele veto	7607.09 ± 39.78	2867.35 ± 22.85	38450.70 ± 92.64	135.40 ± 1.15
jet num ≥ 3	4830.71 ± 24.20	2148.52 ± 19.55	34673.13 ± 88.63	133.26 ± 1.14
tau rnn score ≥ 0.01	4706.78 ± 23.91	1578.54 ± 16.26	25495.22 ± 74.67	117.33 ± 1.07
SR+CR	3248.83 ± 18.91	836.19 ± 11.56	11520.06 ± 48.69	61.43 ± 0.77
	$t\bar{t} \rightarrow bWcH$	$cg \rightarrow tH$	tCh merged signal	$t\bar{t} \rightarrow bWuH$
n-tuple	3480.44 ± 15.20	186.55 ± 1.12	3666.99 ± 15.25	3429.32 ± 14.53
pass trigger	2883.81 ± 13.82	163.69 ± 1.06	3047.50 ± 13.86	2859.48 ± 13.21
ntrack = 1,3	2197.02 ± 12.05	134.00 ± 0.96	2331.02 ± 12.09	2178.49 ± 11.50
ele veto	1666.34 ± 10.51	102.97 ± 0.84	1769.31 ± 10.54	1655.16 ± 10.04
jet num ≥ 3	1560.37 ± 10.22	87.29 ± 0.79	1647.66 ± 10.25	1549.56 ± 9.76
tau rnn score ≥ 0.01	1499.72 ± 10.01	86.12 ± 0.78	1585.84 ± 10.04	1492.38 ± 9.57
SR+CR	1219.99 ± 8.86	72.13 ± 0.71	1292.12 ± 8.89	1308.40 ± 8.89
	$ug \rightarrow tH$	tuH merged signal	Data	total background
n-tuple	1025.81 ± 5.76	4455.13 ± 15.63	1460658.00 ± 1208.58	234130.79 ± 261.54
pass trigger	889.85 ± 5.40	3749.32 ± 14.27	975476.00 ± 987.66	157897.55 ± 210.25
ntrack = 1,3	700.77 ± 4.80	2879.26 ± 12.47	383804.00 ± 619.52	83174.80 ± 158.78
ele veto	533.50 ± 4.19	2188.66 ± 10.87	276245.00 ± 525.59	51712.88 ± 114.98
jet num ≥ 3	448.86 ± 3.90	1998.43 ± 10.51	187734.00 ± 433.28	43611.03 ± 104.15
tau rnn score ≥ 0.01	443.20 ± 3.88	1935.58 ± 10.32	123625.00 ± 351.60	33304.18 ± 83.72
SR+CR	380.38 ± 3.58	1688.78 ± 9.58	54902.00 ± 234.31	16647.86 ± 57.32

Table 23: The cutflow tables in the STH $\tau_{\text{had}}\tau_{\text{had}}$ signal region.

	SM Higgs	W+jets	Diboson	$Z \rightarrow \tau\tau$
this region	20.98 ± 0.46	42.22 ± 6.21	25.41 ± 1.18	1041.13 ± 10.93
$m_{\tau\tau,\text{vis}} > 60$	19.29 ± 0.44	36.98 ± 6.08	17.53 ± 0.99	709.61 ± 9.66
$m_{\tau\tau,\text{vis}} < 120$	18.81 ± 0.44	22.75 ± 4.14	16.12 ± 0.97	690.79 ± 9.56
$\Delta R(\tau, \tau) < 3.4$	18.80 ± 0.44	22.75 ± 4.14	16.12 ± 0.97	690.79 ± 9.56
$100\text{GeV} < m_{\tau\tau} < 150\text{GeV}$	18.23 ± 0.44	17.92 ± 3.97	11.44 ± 0.79	524.17 ± 8.85
$m_{t,\text{FCNC}} > 140\text{GeV}$	17.89 ± 0.43	17.60 ± 3.96	10.91 ± 0.77	500.73 ± 8.71
	Rare	$t\bar{t}$	$t\bar{t}V$	$t\bar{t} \rightarrow bWcH$
this region	91.41 ± 3.75	901.24 ± 12.44	2.82 ± 0.15	166.42 ± 3.23
$m_{\tau\tau,\text{vis}} > 60$	79.68 ± 3.48	800.20 ± 11.73	2.07 ± 0.13	156.80 ± 3.13
$m_{\tau\tau,\text{vis}} < 120$	47.64 ± 2.68	502.19 ± 9.31	1.37 ± 0.10	148.38 ± 3.06
$\Delta R(\tau, \tau) < 3.4$	47.64 ± 2.68	501.37 ± 9.30	1.37 ± 0.10	148.27 ± 3.06
$100\text{GeV} < m_{\tau\tau} < 150\text{GeV}$	34.13 ± 2.28	382.29 ± 8.12	0.86 ± 0.08	138.89 ± 3.00
$m_{t,\text{FCNC}} > 140\text{GeV}$	32.96 ± 2.25	375.17 ± 8.04	0.84 ± 0.08	136.55 ± 2.98
	$cg \rightarrow tH$	tCh merged signal	$\bar{t}t \rightarrow bWuH$	$ug \rightarrow tH$
this region	19.79 ± 0.37	186.22 ± 3.25	171.81 ± 3.19	105.43 ± 1.83
$m_{\tau\tau,\text{vis}} > 60$	18.38 ± 0.35	175.18 ± 3.15	162.23 ± 3.10	94.22 ± 1.74
$m_{\tau\tau,\text{vis}} < 120$	17.66 ± 0.35	166.04 ± 3.08	152.25 ± 3.02	90.85 ± 1.71
$\Delta R(\tau, \tau) < 3.4$	17.66 ± 0.35	165.92 ± 3.08	152.18 ± 3.02	90.85 ± 1.71
$100\text{GeV} < m_{\tau\tau} < 150\text{GeV}$	16.96 ± 0.34	155.85 ± 3.02	141.98 ± 2.95	87.12 ± 1.68
$m_{t,\text{FCNC}} > 140\text{GeV}$	16.75 ± 0.34	153.30 ± 3.00	139.42 ± 2.92	85.94 ± 1.67
	tuH merged signal	Data	total background	
this region	277.24 ± 3.68	2399.00 ± 48.98	2125.23 ± 18.12	
$m_{\tau\tau,\text{vis}} > 60$	256.45 ± 3.55	1753.00 ± 41.87	1665.36 ± 16.76	
$m_{\tau\tau,\text{vis}} < 120$	243.10 ± 3.47	1374.00 ± 37.07	1299.67 ± 14.26	
$\Delta R(\tau, \tau) < 3.4$	243.03 ± 3.47	1371.00 ± 37.03	1298.83 ± 14.26	
$100\text{GeV} < m_{\tau\tau} < 150\text{GeV}$	229.10 ± 3.39	1085.00 ± 32.94	989.04 ± 12.88	
$m_{t,\text{FCNC}} > 140\text{GeV}$	225.36 ± 3.37	1047.00 ± 32.36	956.10 ± 12.73	

Table 24: The cutflow tables in the TTH $\tau_{\text{had}}\tau_{\text{had}}$ signal region.

	SM Higgs	W+jets	Diboson	$Z \rightarrow \tau\tau$
this region	35.04 ± 0.48	32.94 ± 3.26	39.13 ± 1.49	990.30 ± 10.25
$m_{\tau\tau,\text{vis}} > 60$	31.59 ± 0.45	27.05 ± 2.96	26.29 ± 1.30	650.88 ± 9.15
$m_{\tau\tau,\text{vis}} < 120$	29.69 ± 0.45	16.36 ± 2.56	22.71 ± 1.05	628.36 ± 9.05
$\Delta R(\tau, \tau) < 3.4$	29.67 ± 0.45	16.36 ± 2.56	22.71 ± 1.05	628.34 ± 9.05
$100\text{GeV} < m_{\tau\tau} < 150\text{GeV}$	27.83 ± 0.44	14.16 ± 2.50	16.16 ± 0.92	470.15 ± 8.35
$m_{t,\text{FCNC}} > 140\text{GeV}$	27.01 ± 0.43	14.40 ± 2.44	14.99 ± 0.88	437.01 ± 8.22
	Rare	$t\bar{t}$	$t\bar{t}V$	$t\bar{t} \rightarrow bWcH$
this region	80.42 ± 3.49	1221.57 ± 14.63	21.21 ± 0.47	497.31 ± 5.73
$m_{\tau\tau,\text{vis}} > 60$	69.97 ± 3.28	1061.21 ± 13.63	14.43 ± 0.38	467.32 ± 5.56
$m_{\tau\tau,\text{vis}} < 120$	38.35 ± 2.45	658.01 ± 10.77	11.46 ± 0.34	447.43 ± 5.47
$\Delta R(\tau, \tau) < 3.4$	38.15 ± 2.44	656.62 ± 10.76	11.46 ± 0.34	447.43 ± 5.47
$100\text{GeV} < m_{\tau\tau} < 150\text{GeV}$	26.31 ± 2.08	490.44 ± 9.33	6.86 ± 0.27	429.81 ± 5.38
$m_{t,\text{FCNC}} > 140\text{GeV}$	26.30 ± 2.08	473.51 ± 9.18	6.33 ± 0.26	416.00 ± 5.30
	$cg \rightarrow tH$	tCh merged signal	$\bar{t}t \rightarrow bWuH$	$ug \rightarrow tH$
this region	26.87 ± 0.45	524.19 ± 5.75	516.63 ± 5.67	138.53 ± 2.26
$m_{\tau\tau,\text{vis}} > 60$	24.57 ± 0.43	491.89 ± 5.58	486.56 ± 5.50	122.85 ± 2.13
$m_{\tau\tau,\text{vis}} < 120$	23.90 ± 0.43	471.34 ± 5.48	463.62 ± 5.39	119.26 ± 2.10
$\Delta R(\tau, \tau) < 3.4$	23.90 ± 0.43	471.34 ± 5.48	463.45 ± 5.39	119.24 ± 2.10
$100\text{GeV} < m_{\tau\tau} < 150\text{GeV}$	23.21 ± 0.42	453.02 ± 5.40	446.04 ± 5.32	114.90 ± 2.07
$m_{t,\text{FCNC}} > 140\text{GeV}$	22.52 ± 0.41	438.52 ± 5.31	433.49 ± 5.24	111.92 ± 2.05
	tuh merged signal	Data	total background	
this region	655.16 ± 6.10	2716.00 ± 52.12	2420.62 ± 18.56	
$m_{\tau\tau,\text{vis}} > 60$	609.42 ± 5.90	2024.00 ± 44.99	1881.42 ± 17.06	
$m_{\tau\tau,\text{vis}} < 120$	582.88 ± 5.79	1542.00 ± 39.27	1404.94 ± 14.56	
$\Delta R(\tau, \tau) < 3.4$	582.69 ± 5.79	1541.00 ± 39.26	1403.31 ± 14.55	
$100\text{GeV} < m_{\tau\tau} < 150\text{GeV}$	560.94 ± 5.71	1192.00 ± 34.53	1051.91 ± 12.98	
$m_{t,\text{FCNC}} > 140\text{GeV}$	545.41 ± 5.63	1116.00 ± 33.41	999.54 ± 12.77	

Table 25: The cutflow tables for the preselection in the leptonic channels.

	SM Higgs	W+jets	Diboson	$Z \rightarrow ll$
n-tuple	17152.85 ± 102.09	2549803.66 ± 9945.07	259417.38 ± 334.63	5076218.50 ± 8306.74
pass trigger	16477.69 ± 100.32	2518835.54 ± 9889.11	248536.30 ± 333.15	4704322.06 ± 7984.34
leadtauOLR	16087.82 ± 99.05	2419309.44 ± 9772.39	240069.04 ± 325.01	4414736.28 ± 7728.34
subtauOLR	16082.01 ± 99.04	2418923.49 ± 9772.00	239973.79 ± 324.92	4413931.08 ± 7727.78
trigger match	15981.81 ± 98.70	2406789.97 ± 9746.08	239082.36 ± 324.18	4405527.85 ± 7722.63
tight lepton	14974.32 ± 95.86	2325820.71 ± 9589.35	225676.03 ± 318.63	3596467.15 ± 6321.88
Medium,25GeV leadtau	11671.30 ± 82.68	705359.50 ± 4980.18	149254.77 ± 199.43	2765958.95 ± 4754.76
Medium,25GeV subtau	11613.22 ± 82.49	702120.36 ± 4970.87	148609.89 ± 198.85	2763634.87 ± 4751.81
2lSS chargeBDT	11405.04 ± 81.91	698208.87 ± 4956.03	143922.65 ± 198.08	2399199.13 ± 4359.34
SR+CR	392.77 ± 9.55	9148.62 ± 258.83	1442.22 ± 22.99	3501.90 ± 106.01
	$Z \rightarrow \tau\tau$	Rare	$t\bar{t}$	$t\bar{t}V$
n-tuple	569469.50 ± 2600.27	279736.04 ± 187.62	3580387.63 ± 698.29	18645.78 ± 15.01
pass trigger	559082.94 ± 2582.60	267927.73 ± 183.83	3404908.11 ± 681.77	17674.85 ± 14.65
leadtauOLR	546917.05 ± 2556.75	261995.50 ± 181.81	3331840.00 ± 674.43	17395.55 ± 14.52
subtauOLR	546819.15 ± 2556.61	261936.09 ± 181.79	3330895.23 ± 674.33	17387.40 ± 14.51
trigger match	539963.88 ± 2537.77	260875.18 ± 181.43	3312474.25 ± 672.52	17278.52 ± 14.47
tight lepton	515237.69 ± 2485.89	240749.74 ± 174.41	3036019.50 ± 644.25	15835.21 ± 13.85
Medium,25GeV leadtau	332992.81 ± 1959.33	207144.85 ± 161.77	2646376.07 ± 601.22	14330.23 ± 13.00
Medium,25GeV subtau	331682.04 ± 1956.04	206920.51 ± 161.68	2643224.28 ± 600.86	14286.45 ± 12.98
2lSS chargeBDT	329677.16 ± 1952.12	202380.63 ± 159.97	2584398.78 ± 594.40	13923.97 ± 12.83
SR+CR	3598.56 ± 52.46	8348.47 ± 32.26	161797.56 ± 148.42	1122.99 ± 4.12
	$\bar{t}t \rightarrow bWcH$	$cg \rightarrow tH$	tcH merged signal	$\bar{t}t \rightarrow bWuH$
n-tuple	2697.69 ± 4.51	124.01 ± 0.33	2821.70 ± 4.53	2697.40 ± 4.47
pass trigger	2591.28 ± 4.43	119.06 ± 0.33	2710.34 ± 4.44	2592.75 ± 4.38
leadtauOLR	2561.17 ± 4.40	117.83 ± 0.32	2678.99 ± 4.42	2565.50 ± 4.36
subtauOLR	2554.93 ± 4.40	117.50 ± 0.32	2672.43 ± 4.41	2560.52 ± 4.36
trigger match	2499.80 ± 4.35	114.99 ± 0.32	2614.78 ± 4.36	2507.98 ± 4.31
tight lepton	2299.96 ± 4.17	105.90 ± 0.31	2405.86 ± 4.18	2308.31 ± 4.13
Medium,25GeV leadtau	1889.15 ± 3.75	88.14 ± 0.28	1977.29 ± 3.76	1895.11 ± 3.72
Medium,25GeV subtau	1826.74 ± 3.69	84.68 ± 0.27	1911.43 ± 3.70	1829.31 ± 3.66
2lSS chargeBDT	1795.42 ± 3.66	83.34 ± 0.27	1878.76 ± 3.67	1797.87 ± 3.63
SR+CR	553.80 ± 2.08	25.73 ± 0.15	579.53 ± 2.09	552.12 ± 2.05
	$ug \rightarrow tH$	tuH merged signal	Data	total background
n-tuple	631.43 ± 1.70	3328.82 ± 4.78	14388438.00 ± 3793.21	12350831.34 ± 13240.59
pass trigger	608.67 ± 1.67	3201.42 ± 4.69	13747432.00 ± 3707.75	11737765.24 ± 12993.61
leadtauOLR	601.45 ± 1.66	3166.96 ± 4.67	13183266.00 ± 3630.88	11248350.69 ± 12742.35
subtauOLR	599.85 ± 1.66	3160.37 ± 4.66	13181031.00 ± 3630.57	11245948.23 ± 12741.67
trigger match	589.11 ± 1.65	3097.09 ± 4.62	13113541.00 ± 3621.26	11197973.81 ± 12714.78
tight lepton	541.21 ± 1.58	2849.51 ± 4.42	11318527.00 ± 3364.30	9970780.35 ± 11775.31
Medium,25GeV leadtau	442.90 ± 1.42	2338.01 ± 3.98	7534936.00 ± 2744.98	6833088.47 ± 7189.12
Medium,25GeV subtau	427.94 ± 1.40	2257.24 ± 3.92	7524509.00 ± 2743.08	6822091.61 ± 7179.77
2lSS chargeBDT	418.02 ± 1.38	2215.89 ± 3.88	7049077.00 ± 2655.01	6383116.22 ± 6913.89
SR+CR	129.71 ± 0.78	681.83 ± 2.19	186660.00 ± 432.04	189353.10 ± 323.56

Table 26: The cutflow tables in the $l\tau_{\text{had}} 1j$ signal region.

	SM Higgs	W+jets	Diboson	$Z \rightarrow ll$
this region	9.06 ± 1.77	1880.37 ± 103.44	122.06 ± 9.92	487.10 ± 39.28
tau b-veto	7.18 ± 1.42	1813.01 ± 98.27	118.61 ± 9.91	469.90 ± 39.05
	$Z \rightarrow \tau\tau$	Rare	$t\bar{t}$	$t\bar{t}V$
this region	58.59 ± 16.01	467.01 ± 7.56	4164.41 ± 24.09	32.78 ± 0.50
tau b-veto	56.33 ± 15.77	422.87 ± 7.21	3468.88 ± 22.05	31.25 ± 0.48
	$\bar{t}t \rightarrow bWcH$	$cg \rightarrow tH$	tch merged signal	$\bar{t}t \rightarrow bWuH$
this region	61.43 ± 0.61	2.38 ± 0.04	63.81 ± 0.61	62.49 ± 0.62
tau b-veto	59.37 ± 0.60	2.31 ± 0.04	61.69 ± 0.60	60.87 ± 0.61
	$ug \rightarrow tH$	tuH merged signal	Data	total background
this region	12.03 ± 0.21	74.52 ± 0.65	8402.00 ± 91.66	7221.37 ± 115.06
tau b-veto	11.64 ± 0.21	72.51 ± 0.65	7563.00 ± 86.97	6388.03 ± 109.86

Table 27: The cutflow tables in the STH $\tau_{\text{lep}}\tau_{\text{had}}$ signal region.

	SM Higgs	W+jets	Diboson	$Z \rightarrow ll$
this region	44.95 ± 4.35	1596.58 ± 75.51	268.69 ± 9.94	709.14 ± 30.23
tau b-veto	43.32 ± 4.25	1548.17 ± 75.28	259.86 ± 9.83	700.87 ± 30.17
	$Z \rightarrow \tau\tau$	Rare	$t\bar{t}$	$t\bar{t}V$
this region	1622.59 ± 34.11	3562.03 ± 21.28	54565.58 ± 86.65	150.08 ± 1.39
tau b-veto	1585.45 ± 33.27	3431.48 ± 20.90	52130.19 ± 84.74	143.86 ± 1.36
	$\bar{t}t \rightarrow bWcH$	$cg \rightarrow tH$	tch merged signal	$\bar{t}t \rightarrow bWuH$
this region	111.46 ± 0.99	6.06 ± 0.08	117.52 ± 0.99	114.44 ± 0.98
tau b-veto	108.10 ± 0.97	5.91 ± 0.08	114.01 ± 0.98	110.93 ± 0.96
	$ug \rightarrow tH$	tuH merged signal	Data	total background
this region	30.89 ± 0.41	145.33 ± 1.06	57335.00 ± 239.45	62519.64 ± 125.94
tau b-veto	29.91 ± 0.40	140.84 ± 1.04	54806.00 ± 234.11	59843.21 ± 124.17

Table 28: The cutflow tables in the $l\tau_{\text{had}} 2j$ signal region.

	SM Higgs	W+jets	Diboson	$Z \rightarrow ll$
this region	15.04 ± 2.18	945.47 ± 45.67	99.84 ± 8.34	237.32 ± 21.03
tau b-veto	14.31 ± 2.15	908.98 ± 45.31	97.52 ± 8.33	231.64 ± 20.99
	$Z \rightarrow \tau\tau$	Rare	$t\bar{t}$	$t\bar{t}V$
this region	25.37 ± 3.63	356.68 ± 6.59	5402.45 ± 27.28	57.87 ± 0.71
tau b-veto	24.25 ± 3.60	318.29 ± 6.23	4479.10 ± 24.93	54.67 ± 0.69
	$\bar{t}t \rightarrow bWcH$	$cg \rightarrow tH$	tch merged signal	$\bar{t}t \rightarrow bWuH$
this region	56.24 ± 0.59	1.44 ± 0.03	57.68 ± 0.59	58.60 ± 0.60
tau b-veto	54.47 ± 0.58	1.41 ± 0.03	55.87 ± 0.58	56.81 ± 0.59
	$ug \rightarrow tH$	tuH merged signal	Data	total background
this region	7.95 ± 0.17	66.55 ± 0.62	7077.00 ± 84.12	7140.04 ± 58.34
tau b-veto	7.74 ± 0.17	64.55 ± 0.61	6150.00 ± 78.42	6128.77 ± 56.93

Table 29: The cutflow tables in the TTH $\tau_{\text{lep}}\tau_{\text{had}}$ region.

	SM Higgs	W+jets	Diboson	$Z \rightarrow ll$
this region	78.09 ± 3.57	949.53 ± 23.63	256.48 ± 10.66	366.66 ± 12.55
tau b-veto	74.43 ± 3.45	922.72 ± 23.54	249.33 ± 10.59	362.06 ± 12.52
	$Z \rightarrow \tau\tau$	Rare	$t\bar{t}$	$t\bar{t}V$
this region	979.60 ± 14.38	1746.76 ± 14.80	40069.19 ± 73.92	293.97 ± 2.32
tau b-veto	942.69 ± 14.18	1677.04 ± 14.50	38188.59 ± 72.21	281.59 ± 2.27
	$\bar{t}t \rightarrow bWcH$	$cg \rightarrow tH$	tch merged signal	$\bar{t}t \rightarrow bWuH$
this region	143.63 ± 1.20	4.69 ± 0.07	148.32 ± 1.21	150.75 ± 1.19
tau b-veto	138.88 ± 1.18	4.55 ± 0.07	143.44 ± 1.19	145.97 ± 1.18
	$ug \rightarrow tH$	tuH merged signal	Data	total background
this region	25.91 ± 0.40	176.67 ± 1.26	40395.00 ± 200.99	44740.26 ± 82.08
tau b-veto	25.18 ± 0.39	171.15 ± 1.24	38458.00 ± 196.11	42698.44 ± 80.41

Table 30: The cutflow tables in the $l\tau_{\text{had}}\tau_{\text{had}}$ signal region.

	SM Higgs	W+jets	Diboson	$Z \rightarrow ll$
this region	9.75 ± 0.20	34.72 ± 14.21	16.00 ± 1.36	16.32 ± 6.83
tau b-veto	9.09 ± 0.20	33.79 ± 14.20	14.93 ± 1.35	14.91 ± 6.72
	$Z \rightarrow \tau\tau$	Rare	$t\bar{t}$	$t\bar{t}V$
this region	17.45 ± 4.85	23.67 ± 1.49	322.81 ± 6.63	18.31 ± 0.42
tau b-veto	16.38 ± 4.81	21.81 ± 1.43	253.77 ± 5.91	16.97 ± 0.41
	$\bar{t}t \rightarrow bWcH$	$cg \rightarrow tH$	tcH merged signal	$\bar{t}t \rightarrow bWuH$
this region	61.42 ± 0.61	4.74 ± 0.06	66.16 ± 0.61	63.89 ± 0.62
tau b-veto	57.51 ± 0.59	4.46 ± 0.06	61.97 ± 0.59	60.13 ± 0.61
	$ug \rightarrow tH$	tuH merged signal	Data	total background
this region	21.93 ± 0.29	85.81 ± 0.69	407.00 ± 20.17	459.02 ± 17.90
tau b-veto	20.76 ± 0.28	80.89 ± 0.67	322.00 ± 17.94	381.66 ± 17.58

901 References

- 902 [1] ATLAS Collaboration, *Combined Measurement of the Higgs Boson Mass in pp Collisions at*
 903 *$\sqrt{s}=7$ and 8 TeV with the ATLAS and CMS Experiments*, Phys. Rev. Lett. **114** (2015) 191803,
 904 arXiv: [1503.07589 \[hep-ex\]](#).
- 905 [2] S. Glashow, J. Iliopoulos and L. Maiani, *Weak Interactions with Lepton-Hadron Symmetry*,
 906 Phys. Rev. D **2** (1970) 1285.
- 907 [3] J. Aguilar-Saavedra,
 908 *Top flavor-changing neutral interactions: Theoretical expectations and experimental detection*,
 909 Acta Phys. Polon. B **35** (2004) 2695, arXiv: [0409342 \[hep-ph\]](#).
- 910 [4] F. del Aguila, J. A. Aguilar-Saavedra, and R. Miquel,
 911 *Constraints on top couplings in models with exotic quarks*, Phys. Rev. Lett. **82** (1999) 1628,
 912 arXiv: [9808400 \[hep-ph\]](#).
- 913 [5] J. Aguilar-Saavedra, *Effects of mixing with quark singlets*, Phys. Rev. D **67** (2003) 035003,
 914 arXiv: [0210112 \[hep-ph\]](#).
- 915 [6] S. Bejar, J. Guasch and J. Sola, *Loop induced flavor changing neutral decays of the top quark in a*
 916 *general two Higgs doublet model*, Nucl. Phys. B **600** (2001) 21, arXiv: [0011091 \[hep-ph\]](#).
- 917 [7] I. Baum, G. Eilam and S. Bar-Shalom, *Scalar flavor changing neutral currents and rare top quark*
 918 *decays in a two Higgs doublet model 'for the top quark'*, Phys. Rev. D **77** (2008) 113008,
 919 arXiv: [0802.2622 \[hep-ph\]](#).
- 920 [8] J. J. Cao et al., *SUSY-induced FCNC top-quark processes at the large hadron collider*,
 921 Phys. Rev. D **75** (2007) 075021, arXiv: [0702264 \[hep-ph\]](#).
- 922 [9] G. Eilam et al., *Top quark rare decay $t \rightarrow ch$ in R-parity violating SUSY*,
 923 Phys. Lett. B **510** (2001) 227, arXiv: [0102037 \[hep-ph\]](#).
- 924 [10] G. Lu et al., *The rare top quark decays $t \rightarrow cV$ in the topcolor-assisted technicolor model*,
 925 Phys. Rev. D **68** (2003) 015002, arXiv: [0303122 \[hep-ph\]](#).
- 926 [11] K. Agashe, G. Perez and A. Soni,
 927 *Collider signals of top quark flavor violation from a warped extra dimension*,
 928 Phys. Rev. D **75** (2007) 015002, arXiv: [0606293 \[hep-ph\]](#).
- 929 [12] B. Yang, N. Liu and J. Han, *Top quark flavor-changing neutral-current decay to a 125 GeV Higgs*
 930 *boson in the littlest Higgs model with T parity*, , Phys. Rev. D **89** (2014) 034020,
 931 arXiv: [1308.4852 \[hep-ph\]](#).
- 932 [13] K. Agashe and R. Contino, *Composite Higgs-mediated flavor-changing neutral current*,
 933 Phys. Rev. D **80** (2009) 075016, arXiv: [0906.1542 \[hep-ph\]](#).

- [14] T. P. Cheng and Marc Sher,
Mass Matrix Ansatz and Flavor Nonconservation in Models with Multiple Higgs Doublets,
Phys. Rev. D **35** (1987) 3484.
- [15] Wei-Shu Hou, *Tree level $t \rightarrow ch$ or $h \rightarrow t\bar{c}$ decays*, Phys. Lett. B **296** (1992) 179.
- [16] Federico Demartin, Fabio Maltoni, Kentarou Mawatari, Marco Zaro,
Higgs production in association with a single top quark at the LHC, (2015),
arXiv: [1504.00611 \[hep-ph\]](https://arxiv.org/abs/1504.00611).
- [17] ATLAS Collaboration, *Search for top quark decays $t \rightarrow qH$, with $H \rightarrow \gamma\gamma$, in $\sqrt{s} = 13$ TeV pp collisions using the ATLAS detector*, JHEP **(2017) 129**, arXiv: [1707.01404 \[hep-ex\]](https://arxiv.org/abs/1707.01404).
- [18] ATLAS Collaboration,
Search for flavor-changing neutral currents in top quark decays $t \rightarrow Hc$ and $t \rightarrow Hu$ in multilepton final states in proton–proton collisions at $\sqrt{s} = 13$ TeV with the ATLAS detector, Phys. Rev. D **(2018) 36**, arXiv: [1805.03483 \[hep-ex\]](https://arxiv.org/abs/1805.03483).
- [19] ATLAS Collaboration, *Search for top-quark decays $t \rightarrow qH$ with 36 fb $^{-1}$ of pp collision data at $\sqrt{s}=13$ TeV with the ATLAS detector*, (), arXiv: [1812.11568 \[hep-ex\]](https://arxiv.org/abs/1812.11568).
- [20] CMS Collaboration, *Search for the flavor-changing neutral current interactions of the top quark and the Higgs boson which decays into a pair of b quarks at $\sqrt{s} = 13$ TeV*, JHEP **06** (2018) 102, arXiv: [1712.02399 \[hep-ex\]](https://arxiv.org/abs/1712.02399).
- [21] Celine Degrande, Fabio Maltoni, Jian Wang, Cen Zhang, *Automatic computations at next-to-leading order in QCD for top-quark flavor-changing neutral processes*, Phys. Rev. D **(2015) 6**, arXiv: [1412.5594 \[hep-ex\]](https://arxiv.org/abs/1412.5594).
- [22] ATLAS Collaboration, *The ATLAS Experiment at the CERN Large Hadron Collider*, JINST **3** (2008) S08003.
- [23] ATLAS Collaboration, *ATLAS Insertable B-Layer Technical Design Report*, CERN-LHCC-2010-013; ATLAS-TDR-19, 2010,
URL: <https://cds.cern.ch/record/1291633>.
- [24] ATLAS Collaboration,
Luminosity determination in pp collisions at $\sqrt{s} = 8$ TeV using the ATLAS detector at the LHC, (2016), arXiv: [1608.03953 \[hep-ex\]](https://arxiv.org/abs/1608.03953).
- [25] Celine Degrande et al., *Automatic computations at next-to-leading order in QCD for top-quark flavor-changing neutral processes*, Phys. Rev. D **91** (2015) 034024, arXiv: [1412.5594 \[hep-ph\]](https://arxiv.org/abs/1412.5594).
- [26] Celine Degrande et al., *Effective theory for top flavor changing interactions*, 2016,
URL: <https://feynrules.irmp.ucl.ac.be/wiki/TopFCNC>.
- [27] J. Alwall et al., *The automated computation of tree-level and next-to-leading order differential cross sections, and their matching to parton shower simulations*, JHEP **07** (2014) 079, arXiv: [1405.0301 \[hep-ph\]](https://arxiv.org/abs/1405.0301).

- [28] T. Sjostrand et al., *An introduction to PYTHIA 8.2*, Comp. Phys. Commun. **191** (2015) 159, arXiv: [1410.3012 \[hep-ph\]](https://arxiv.org/abs/1410.3012).
- [29] ATLAS Collaboration, *ATLAS Pythia 8 tunes to 7 TeV data*, ATL-PHYS-PUB-2014-021, 2014, URL: <https://cdsweb.cern.ch/record/196641>.
- [30] R. D. Ball et al., *Parton distributions for the LHC Run II*, JHEP **04** (2015) 040, arXiv: [1410.8849 \[hep-ph\]](https://arxiv.org/abs/1410.8849).
- [31] C. Oleari, *The POWHEG-BOX*, Nucl. Phys. Proc. Suppl. **205-206** (2010) 36–41, arXiv: [1007.3893 \[hep-ph\]](https://arxiv.org/abs/1007.3893).
- [32] T. Gleisberg et al., *Event generation with Sherpa 1.1*, JHEP **02** (2009) 007, arXiv: [0811.4622 \[hep-ph\]](https://arxiv.org/abs/0811.4622).
- [33] N. Davidson et al., *Universal interface of TAUOLA: Technical and physics documentation*, Comp. Phys. Commun. **183** (2012) 821.
- [34] S. Agostinelli et al., *GEANT4 - A simulation toolkit*, Nucl. Instrum. Meth. A **506** (2003) 250.
- [35] J. Bellm et al., *Herwig 7.0/Herwig++ 3.0 release note*, Eur. Phys. J. C **76** (2016) 196.
- [36] ATLAS Collaboration, *The simulation principle and performance of the ATLAS fast calorimeter simulation FastCaloSim*, ATL-PHYS-PUB-2010-013, 2010, URL: [http://cds.cern.ch/record/1300517](https://cds.cern.ch/record/1300517).
- [37] J Butterworth et al., *Single Boson and Diboson Production Cross Sections in pp Collisions at $\sqrt{s}=7$ TeV*, ATL-COM-PHYS-2010-695, 2010, URL: [http://cds.cern.ch/record/1287902](https://cds.cern.ch/record/1287902).
- [38] M. Czakon and A. Mitov, *Top++: a program for the calculation of the top-pair cross-section at hadron colliders*, Comput. Phys. Commun **185** (2014) 2930, arXiv: [1112.5675 \[hep-ph\]](https://arxiv.org/abs/1112.5675).
- [39] D. de Florian et al., *Handbook of LHC Higgs Cross Sections: 4. Deciphering the Nature of the Higgs Sector*, CERN-2017-002-M (2017), arXiv: [1610.07922 \[hep-ph\]](https://arxiv.org/abs/1610.07922), URL: <https://cds.cern.ch/record/2227475>.
- [40] J. Alwall et al., *The automated computation of tree-level and next-to-leading order differential cross sections, and their matching to parton shower simulations*, JHEP **07** (2014) 079, arXiv: [1405.0301 \[hep-ph\]](https://arxiv.org/abs/1405.0301).
- [41] M. Aliiev et al., *HATHOR - HAdronic Top and Heavy quarks crOss section calculatoR*, Comput. Phys. Commun **182** (2011) 1034, arXiv: [1007.1327 \[hep-ph\]](https://arxiv.org/abs/1007.1327).
- [42] P. Kant et al., *HATHOR for single top-quark production: Updated predictions and uncertainty estimates for single top-quark production in hadronic collisions*, Comput. Phys. Commun **191** (2015) 74, arXiv: [1406.4403 \[hep-ph\]](https://arxiv.org/abs/1406.4403).

- 1005 [43] N. Kidonakis,
 1006 *Two-loop soft anomalous dimensions for single top quark associated production with a W^- or H^- ,*
 1007 Phys. Rev. D **82** (2010) 054018, arXiv: [1005.4451 \[hep-ph\]](#).
- 1008 [44] J. Pumplin et al.,
 1009 *New Generation of Parton Distributions with Uncertainties from Global QCD Analysis,*
 1010 JHEP **07** (2002) 012, arXiv: [0201195 \[hep-ph\]](#).
- 1011 [45] M. Cacciari, G. P. Salam, and G. Soyez, *The Anti- $k(t)$ jet clustering algorithm,*
 1012 JHEP **04** (2008) 063, arXiv: [0802.1189 \[hep-ph\]](#).
- 1013 [46] ATLAS Collaboration, *Tagging and suppression of pileup jets with the ATLAS detector,*
 1014 ATLAS-CONF-2014-018, 2014, URL: <http://cds.cern.ch/record/1700870>.
- 1015 [47] ATLAS Collaboration, *Optimisation of the ATLAS b-tagging performance for the 2016 LHC Run,*
 1016 ATL-PHYS-PUB-2016-012, 2016, URL: <https://cds.cern.ch/record/2160731>.
- 1017 [48] *Electron and Photon Selection and Identification for Run2*, Accessible on 2021-1-3, URL: <https://twiki.cern.ch/twiki/bin/view/AtlasProtected/EGammaIdentificationRun2>.
- 1018 [49] *Official Isolation Working Points*, Accessible on 2021-1-3, URL: <https://twiki.cern.ch/twiki/bin/viewauth/AtlasProtected/IsolationSelectionTool#Leptons>.
- 1019 [50] *MuonSelectionTool*, Accessible on 2021-1-3,
 1020 URL: <https://twiki.cern.ch/twiki/bin/view/Atlas/MuonSelectionTool>.
- 1021 [51] ATLAS Collaboration, *Reconstruction, Energy Calibration, and Identification of Hadronically*
 1022 *Decaying Tau Leptons in the ATLAS Experiment for Run-2 of the LHC,*
 1023 ATL-PHYS-PUB-2015-045, 2015, URL: <https://cds.cern.ch/record/2064383>.
- 1024 [52] ATLAS Collaboration,
 1025 *Jet energy measurement with the ATLAS detector in proton-proton collisions at $\sqrt{s} = 7 \text{ TeV}$,*
 1026 Eur. Phys. J. C **73** (2013) 2304, arXiv: [1112.6426 \[hep-ex\]](#).
- 1027 [53] *Measurement of the Higgs boson coupling properties in the $H \rightarrow \tau\tau$ decay channel at $\sqrt{s}=13\text{TeV}$*
 1028 *with the ATLAS detector*, 2020, URL: <https://cds.cern.ch/record/2741326>.
- 1029 [54] *TauAnalysisTools*, Accessible on 2021-1-3,
 1030 URL: <https://twiki.cern.ch/twiki/bin/view/AtlasProtected/TauAnalysisTools>.
- 1031 [55] *Measurement of the total and differential production cross-sections of $t\bar{t}W$ production at 13 TeV in*
 1032 *139 fb^{-1} of data with the ATLAS detector*, 2021,
 1033 URL: <https://atlas-glance.cern.ch/atlas/analysis/analyses/details?id=3390>.
- 1034 [56] *Tau Recommendations*, Accessible on 2021-1-3, URL:
 1035 <https://twiki.cern.ch/twiki/bin/view/AtlasProtected/TauRecommendationsR21>.
- 1036 [57] *Usage of Missing ET in analyses: rebuilding and systematics*, Accessible on 2021-1-3,
 1037 URL: <https://twiki.cern.ch/twiki/bin/viewauth/AtlasProtected/METUtilities>.

- 1040 [58] ATLAS Collaboration, *Search for the Associated Production of a Higgs Boson and a Top Quark*
 1041 *Pair in multilepton final states in 80 fb^{-1} pp Collisions at $\sqrt{s} = 13\text{ TeV}$ with the ATLAS Detector*,
 1042 ATL-COM-PHYS-2018-410, 2018, URL: <https://cds.cern.ch/record/2314122>.
- 1043 [59] ATLAS Collaboration,
 1044 *Measurement of the $H \rightarrow \tau^+\tau^-$ cross-section in 13TeV Collisions with the ATLAS Detector*,
 1045 ATL-COM-PHYS-2017-446, 2017, URL: <https://cds.cern.ch/record/2261605>.
- 1046 [60] J. Friedman, *Stochastic gradient boosting*, Comput. Stat. Data Anal. **38** (2002) 367.
- 1047 [61] A. Hoecker et al., *TMVA - Toolkit for Multivariate Data Analysis*, PoS A CAT **040** (2007),
 1048 arXiv: [0703039 \[physics\]](https://arxiv.org/abs/0703039).
- 1049 [62] *TRExFitter*, Accessible on 2021-1-3,
 1050 URL: <https://gitlab.cern.ch/TRExStats/TRExFitter>.
- 1051 [63] ATLAS Collaboration, *Electron efficiency measurements with the ATLAS detector using the 2015*
 1052 *LHC proton–proton collision data*, ATL-CONF-2016-024, 2016,
 1053 URL: <https://cds.cern.ch/record/2157687>.
- 1054 [64] ATLAS Collaboration, *Jet Calibration and Systematic Uncertainties for Jets Reconstructed in the*
 1055 *ATLAS Detector at $\sqrt{s} = 13\text{ TeV}$* , ATL-PHYS-PUB-2015-015, 2015,
 1056 URL: <https://cds.cern.ch/record/2037613>.
- 1057 [65] ATLAS Collaboration, *Performance of missing transverse momentum reconstruction for the*
 1058 *ATLAS detector in the first proton-proton collisions at $\sqrt{s} = 13\text{ TeV}$* , ATL-PHYS-PUB-2015-027,
 1059 2015, URL: <https://cds.cern.ch/record/2037904>.
- 1060 [66] ATLAS Collaboration, *Expected performance of the ATLAS b-tagging algorithms in Run-2*,
 1061 ATL-PHYS-PUB-2015-022, 2015, URL: <https://cds.cern.ch/record/2037697>.
- 1062 [67] ATLAS Collaboration,
 1063 *Calibration of the performance of b-tagging for c and light-flavour jets in the 2012 ATLAS data*,
 1064 ATL-CONF-2014-046, 2014, URL: <https://cds.cern.ch/record/1741020>.
- 1065 [68] ATLAS Collaboration, *Calibration of b-tagging using dileptonic top pair events in a*
 1066 *combinatorial likelihood approach with the ATLAS experiment*, ATL-CONF-2014-004, 2014,
 1067 URL: <https://cds.cern.ch/record/1664335>.
- 1068 [69] ATLAS Collaboration,
 1069 *Studies on top-quark Monte Carlo modelling with Sherpa and MG5_aMC@NLO*,
 1070 ATL-PHYS-PUB-2017-007, 2017, URL: <https://cds.cern.ch/record/2261938>.
- 1071 [70] ATLAS Collaboration, *Search for flavor-changing neutral current $t \rightarrow Hq$ ($q=u,c$) decays, with*
 1072 *$H \rightarrow b\bar{b}$, in the lepton+jets final state in pp collisions at $\sqrt{s} = 13\text{ TeV}$ with the ATLAS detector*,
 1073 ATL-COM-PHYS-2017-346, 2017, URL: <https://cds.cern.ch/record/2257631>.
- 1074 [71] J. M. Campbell and R. K. Ellis, *An Update on vector boson pair production at hadron colliders*,
 1075 Phys. Rev. D **60** (1999) 113006, arXiv: [9905386 \[hep-ph\]](https://arxiv.org/abs/9905386).

-
- 1076 [72] N. Kidonakis, *Next-to-next-to-leading-order collinear and soft gluon corrections for t-channel*
1077 *single top quark production*, Phys. Rev. D **83** (2011) 091503, arXiv: [1103.2792 \[hep-ph\]](#).
- 1078 [73] N. Kidonakis, *NNLL resummation for s-channel single top quark production*,
1079 Phys. Rev. D **81** (2010) 054028, arXiv: [1001.5034 \[hep-ph\]](#).
- 1080 [74] M. V. Garzelli et al., *$t\bar{t}W^\pm$ and $t\bar{t}Z$ Hadroproduction at NLO accuracy in QCD with Parton*
1081 *Shower and Hadronization effects*, JHEP **1211** (2012) 056, arXiv: [1208.2665 \[hep-ph\]](#).
- 1082 [75] J. M. Campbell and R. K. Ellis, *$t\bar{t}W^\pm$ production and decay at NLO*, JHEP **1207** (2012) 052,
1083 arXiv: [1204.5678 \[hep-ph\]](#).
- 1084 [76] LHC Higgs Cross Section Working Group,
1085 *Handbook of LHC Higgs Cross Sections: 1. Inclusive Observables*, (2011),
1086 arXiv: [1101.0593 \[hep-ph\]](#).
- 1087 [77] G. Cowan, K. Cranmer, E. Gross and O. Vitells,
1088 *Asymptotic formulae for likelihood-based tests of new physics*, Eur. Phys. J. C **71** (2011) 1554,
1089 arXiv: [1007.1727 \[physics.data-an\]](#).
- 1090 [78] *AnalysisTop*, Accessible on 2021-1-3,
1091 URL: <https://twiki.cern.ch/twiki/bin/view/AtlasProtected/AnalysisTop21>.

1092 List of contributions

1093

- 1094 • Boyang Li: main analyser, analysis code maintainer; signal generation; derivation, ntuple produc-
1095 tion; fake tau estimation; BDT analysis; systematics; fit; support note.
- 1096 • Weiming Yao: main analyser, `tthML` ntuple skimming and support; fake tau estimation; BDT
1097 analysis; cross check; support note.
- 1098 • MingMing Xia: main analyser, `xTauFramework` n-tuple production; production validation; fake
1099 tau estimation in hadronic channels.
- 1100 • Xin Chen: Supervisor of Boyang Li and MingMing Xia